



THE HONG KONG
POLYTECHNIC UNIVERSITY

香港理工大學

Pao Yue-kong Library

包玉剛圖書館

Copyright Undertaking

This thesis is protected by copyright, with all rights reserved.

By reading and using the thesis, the reader understands and agrees to the following terms:

1. The reader will abide by the rules and legal ordinances governing copyright regarding the use of the thesis.
2. The reader will use the thesis for the purpose of research or private study only and not for distribution or further reproduction or any other purpose.
3. The reader agrees to indemnify and hold the University harmless from and against any loss, damage, cost, liability or expenses arising from copyright infringement or unauthorized usage.

IMPORTANT

If you have reasons to believe that any materials in this thesis are deemed not suitable to be distributed in this form, or a copyright owner having difficulty with the material being included in our database, please contact lbsys@polyu.edu.hk providing details. The Library will look into your claim and consider taking remedial action upon receipt of the written requests.

OPTICALLY-CONTROLLED
MULTIFUNCTIONAL ELECTRONIC
DEVICES

ZHOU FEICHI

PhD

The Hong Kong Polytechnic University
2018

The Hong Kong Polytechnic University

Department of Applied Physics

Optically-Controlled Multifunctional
Electronic Devices

ZHOU Feichi

A thesis submitted in partial fulfillment of the requirements for
the degree of Doctor of Philosophy

Jan 2018

CERTIFICATE OF ORIGINALITY

I hereby declare that this thesis is my own work and that, to the best of my knowledge and belief, it reproduces no material previously published or written, nor material that has been accepted for the award of any other degree or diploma, except where due acknowledgement has been made in the text.

Signature:

ABSTRACT

In the era of information explosion, Internet of Things (IoT) has emerged as a technological revolution. With the rapidly increased number of IoT devices, IoT will drive unprecedented volumes and demands for the electronics industry. A multifunctional and highly integrated device can well benefit the IoT system operation and cater for the demands of smart device, such as reducing cost and device occupation area, and lowering energy consumption and electric loss. In this thesis, we design two types of optically-controlled multifunctional electronic devices: (1) multifunctional solar-power supercapacitor by integrating novel perovskite solar cell and electrochromic supercapacitor into one device and (2) hybrid organic-inorganic and transition metal oxide based optoelectronic memories, which both integrate sensing, data storage and processing functions.

We first demonstrate multifunctional supercapacitor devices: solar-powered photovoltachromic supercapacitors (PVCSs) by vertically integrating a perovskite solar cell (PSC) with $\text{MoO}_3/\text{Au}/\text{MoO}_3$ transparent electrode and electrochromic supercapacitor into one device. These PVCSs provide a seamless integration of energy harvesting/storage device, automatic and wide color tunability and enhanced photo-stability of PSCs. The color states of PVCSs not only indicate the amount of energy stored and energy consumed in real time, but also enhance the photo-stability of photovoltaic component by preventing its long-time photo-exposure under fully charged state of PVCSs. This work designs a new type PVCS for multifunctional smart

window applications commonly made of glass.

Except for the multifunctional and integrated solar-powered supercapacitors, to develop optoelectronic memories integrated with the functions of sensing, data storage and data processing is also desirable for the potential Internet of Things (IoT) application. In this thesis, we demonstrate two types of optoelectronic resistive switching memory integrated with sensing, data storage and processing by adopting hybrid organic-inorganic $\text{CH}_3\text{NH}_3\text{PbI}_{3-x}\text{Cl}_x$ perovskites and MoO_3 , respectively. Based on the unusual defect physics and excellent light absorption, the $\text{CH}_3\text{NH}_3\text{PbI}_{3-x}\text{Cl}_x$ memory cell designed in our work exhibits low operation voltage of 0.1 V with the assistance of light illumination, long-term retention property, and multiple resistance states. Its unique optoelectronic characteristics enable to perform logic operation for inputting one electrical pulse and one optical signal, and detect the coincidence of electrical and optical signal as well. This design provides possibilities for smart sensor in IoT application. Except for the non-volatile perovskite optoelectronic memory, we also adopted photochromic material MoO_3 as both light absorption layer and storage medium and designed UV switchable optoelectronic memory. The MoO_3 memory enables both non-volatile and volatile resistive switching behaviors according to different light intensity and light wavelength applied. The co-existence of non-volatile and volatile behaviors enables the implementation of light-stimulated short-term (STP) and long-term plasticity (LTP) for neuromorphic computing, which bridges the gap between sensing and neuromorphic computing and is potential for the design of cognitive artificial eyes.

LIST OF PUBLICATIONS

1. Feichi Zhou, Zhiwei Ren, Yuda Zhao, Xinpeng Shen, Aiwu Wang, Yang Yang Li, Charles Surya, and Yang Chai*, "Perovskite Photovoltachromic Supercapacitor with All Transparent Electrodes", *ACS Nano*, 2016, 10(6), 5900-5908
2. Feichi Zhou, Yanghui Liu, Xinpeng Shen, Mengye Wang, Fang Yuan, and Yang Chai*, "Low-Voltage, Optoelectronic $\text{CH}_3\text{NH}_3\text{PbI}_{3-x}\text{Cl}_x$ Memory with Integrated Sensing and Logic Operations", *Advanced Functional Materials*, 2018, 28, 1800080
3. Feichi Zhou, Yanghui Liu, Jiewei Chen, Mengye Wang and Yang Chai*, "UV switchable transition metal based optoelectronic memory", submit to International Electron Device Meeting.
4. Feichi Zhou and Yang Chai. Multifunctional perovskite photovoltachromic supercapacitor, *Nanoelectronics Conference (INEC)*, 2016 IEEE International. IEEE, 2016: 1-2.
5. Feichi Zhou, Perovskite Photovoltachromic Supercapacitor with All Transparent Electrodes, presented in the **2017 Spring Material Research Society Conference**.
6. Fang Yuan, Zhi Zhang, Chunru Liu, Feichi Zhou, Hei Man Yau, Wei Lu, Xiaoyan Qiu, H.-S. Philip Wong, Jiyan Dai, and Yang Chai*, "Real-time observation of the electrode-size-dependent evolution dynamics of the conducting filaments in a SiO_2 layer", *ACS Nano*, 2017, 11 (4), 4097–4104.
7. Mengye Wang, Leijuan Cai, Yi Wang, Feichi Zhou, Kang Xu, Xiaoming Tao, and Yang Chai*, "Graphene-draped semiconductors for enhanced photocorrosion resistance and photocatalytic properties", *Journal of the American Chemistry Society*, 2017, 139(11), 4144-4151.
8. Yuda Zhao, Kang Xu, Feng Pan, Changjian Zhou, Feichi Zhou, and Yang Chai*, "Doping, Contact and Interface Engineering of Two-Dimensional Layered Transition Metal Dichalcogenides Transistors", *Advanced Functional Materials*, 2016.
9. Xinpeng Shen, Mengye Wang, Feichi Zhou, Bocheng Qiu, Lejuan Cai, Yanghui Liu, Zijian Zheng and Yang Chai*, *Journal of Material Chemistry C*, DOI: 10.1039/C8TC01507D.
10. Xiaoyan Qiu, R.X. Wang, Zhi Zhang, Minglong Wei, H. Ji, Yang Chai, Feichi Zhou, Jiyan Dai, *Applied Physics Letters* 111(14):142103.

ACKNOWLEDGEMENTS

I am honored to have the opportunity to pursue my Ph.D. studies in the department of applied physics at the Hong Kong Polytechnic University.

Firstly, I would like to express my sincere gratitude to my supervisor, Dr. Yang CHAI, for his active encouragement and academic support throughout my Ph.D. student study period. None of this would have been possible without his guidance. Meanwhile, I would like to thank my group mates including, Dr. Yuda Zhao, Dr. Changjian Zhou, Dr. Fang Yuan, Dr. Mengye Wang, Dr. Jingli Wang, Dr. Yanghui Liu, Dr. Bocheng Qiu, Dr. Yang Wang, Mr. Feng Pan, Mr. Jiewei Chen, Mr. Ziyuan Lin, Mr. Kang Xu, Mr. Xinpeng Shen, Mr. Yi Wang, Mr Yunpeng Zuo, Ms Lejuan Cai for their useful advices, kind assistance during my research study.

Last but not the least, I also have to show my special appreciation to my dear parents for their endless love and support throughout my Ph.D. study.

TABLE OF CONTENT

CERTIFICATE OF ORIGINALITY	I
ABSTRACT	II
LIST OF PUBLICATIONS.....	IV
ACKNOWLEDGEMENTS	V
TABLE OF CONTENT	VI
LIST OF FIGURES	VIII
LIST OF TABLES	XIII
CHAPTER 1 Introduction: Demands for Multifunctional Integrated Electronic Devices	1
CHAPTER 2 Multifunctional Solar-Powered Supercapacitor	4
2.1 Introduction.....	4
2.1.1. Energy storage devices.....	4
2.1.1.1. Supercapacitors: working principles and materials	7
2.1.1.2. Electrochemical characterizations	12
2.1.2. Smart supercapacitor: electrochromic supercapacitor (ECS).....	15
2.1.2.1. Electrochromism & traditional electrochromic cell	15
2.1.2.2. Integration possibilities for electrochromic supercapacitor (ECS)..	17
2.1.2.3. Material candidates	17
2.1.2.4. Challenges and outlook	24
2.1.3. Integration of energy harvesting/storage systems	25
2.1.3.1. Solar powered supercapacitors.....	25
2.1.3.2. Challenges and outlook	33
2.2 Multifunctional perovskite photovoltachromic supercapacitor.....	34
2.2.1. Motivation.....	34
2.2.2. Experiments.....	38
2.2.3. Results and discussions	41
2.2.4. Summary	59
References.....	61
CHAPTER 3 Optoelectronic Random Access Memory with Integrated Sensing and Logic Operations	65
3.1 Introduction.....	65
3.1.1. Overviews of Resistive Random Access Memories (RRAMs).....	66
3.1.2. Basic working principles.....	66
3.1.3. Key evaluation parameters	68
3.1.4. Materials and switching mechanisms.....	69
3.1.4.1. Anion migration	70
3.1.4.2. Cation migration.....	75
3.1.4.3. Charge trapping/de-trapping.....	79
3.1.5. Optoelectronic resistive switching memories.....	82
3.2 Low voltage, optoelectronic CH ₃ NH ₃ PbI _{3-x} Cl _x Memory with Integrated Sensing and Logic Operations.....	86

3.2.1.	Motivation.....	86
3.2.2.	Experiments.....	88
3.2.3.	Results and Discussions	90
3.2.4.	Summary	104
	References.....	106
CHAPTER 4	UV-switchable Transition Metal Oxide Optoelectronic Memory	111
4.1	Introduction.....	111
4.2	Experiments	113
4.3	Results and Discussions	114
4.3.1.	Device structure and switching characteristics	114
4.3.2.	Switching mechanisms.....	117
4.3.3.	Synaptic functions.....	122
4.3.4.	Emulation of visual image memory training	124
4.4	Summary	125
	References.....	127
CHAPTER 5	Summary and Outlook	128

LIST OF FIGURES

Figure 2.1. Charge storage mechanisms of rechargeable battery, supercapacitor and intercalation pseudocapacitance.....	6
Figure 2.2. Ragone plot with energy density vs power density of various energy storage devices. ^[2]	6
Figure 2.3 Schematics of working mechanisms of EDLCs. ^[7]	8
Figure 2.4. Illustration of a typical working mechanism in the pseudocapacitors. ^[7]	11
Figure 2.5 (a) Voltage (E) vs time (t) in the CV measurements. The voltage ramps linearly with time. (b) A typical CV curve corresponding to the voltage sweeping in (a). ^[32]	13
Figure 2.6. Typical GCD curves for EDLCs and hybrid supercapacitor. ^[10]	14
Figure 2.7. A schematic of electrochromic cell. ^[33]	16
Figure 2.8. Applications of electrochromic windows. ^[34, 35]	16
Figure 2.9. Multifunctional WO ₃ electrochromic supercapacitor reported by Yang <i>et al.</i> ^[36] ..	19
Figure 2.10. Electrochromism and energy storage properties in NiO _x . ^[39]	20
Figure 2.11. Energy storage performances and electrochromism in the V ₂ O ₅ ECS. ^[41]	21
Figure 2.12 Conducting polymers for electrochromism and energy storage (a)-(d) PANI energy storage smart window. ^[45] (e) Schematics of PEDOP-Au@WO ₃ structure. (f) Optical transmittance of PEDOP-Au@WO ₃ electrochromic material vs voltage and time. ^[46] ..	22
Figure 2.13. (a) and (b) optical photos and <i>In situ</i> optical transmittance of Prussian based ECS device. ^[47] (c) and (d) Optical transmittances during Li intercalation process and photos of color change before and after the intercalation process. ^[49]	24
Figure 2.14. A typical J-V curve of solar cells with and without light illumination.	26
Figure 2.15. (a) Schematics of a DSSC. ^[60] (b) Energy diagram of a typical DSSC. ^[61]	27
Figure 2.16. (a) Schematics of an integrated DSSC and CNT supercapacitor. (b) Cross-section of the fiber-shaped device. (c) Photo-charging and discharging curves. (d) The charging and discharging performances under stretching. ^[62]	29
Figure 2.17 (a) A power pack including DSSC and LIB with Ti substrate as a common platform. (b) Schematics of illustrated working mechanism. (c)(d)(e) SEM images of TiO ₂ nanotubes on the Ti foil. (f) Photo-charging and discharge curves. ^[63]	29
Figure 2.18. A fiber-shaped energy pack in three-electrode configuration by using Ti wire as a common platform. (a) Schematics of photo-charging and discharging. (b) Photo-charging and discharging curves. A fiber-shaped energy pack with PANI-ss as the common electrode. (c) Schematics and cross section image. (d) Photo-charging and discharging curves. ^[64]	30
Figure 2.19. Schematics and working mechanisms of a typical polymer solar cell. ^[67]	31
Figure 2.20. Polymer solar cell/CNT supercapacitor package. (a) Device structure. (b) Photo-charging and discharging curves. ^[68]	32
Figure 2.21 (a) A fiber-shaped energy pack. (b) Photo-charging and discharging curve. ^[69] ...	32
Figure 2.22. A typical perovskite device structure and band diagram. ^[70]	33
Figure 2.23. (a) Schematics of PECC and PVCC. (b) Transmittance spectra of PECC at as-prepared and colored states (open-circuit condition). (c) Photos of PECC and PVCC colored states. (d) The transmittance spectra illustrating the bleaching of PECC and	

PVCC at open circuit condition and short circuit condition at a wavelength of 788 nm.	36
Figure 2.24 (a) Schematics of a PVCC device based on perovskite solar cell and WO ₃ electrochromic cell. (b) and (c) Photos of PVCC at bleached state and colored state, respectively.	36
Figure 2.25. Fabrication process flow of the PSC.....	40
Figure 2.26. (a) Absorption spectra of perovskite film on quartz. (b) SEM image of perovskite film.....	42
Figure 2.27. (a) Schematic diagram and photo of PSC with MAM transparent electrode. (b) UV-Vis spectra of the as-fabricated MAM, showing an AVT of 70.6 %. (c) UV-Vis spectra of the whole PSC device with the MAM top electrode. (d) <i>J-V</i> curves of a typically semitransparent PSC (MAM electrode) with the light illuminated from both FTO side and MAM side, exhibiting PCEs of 12.54% and 9.35%, respectively.....	42
Figure 2.28. A <i>J-V</i> curve of a typical PSC device with Au top electrode, showing a PCE of 16.4 %.	43
Figure 2.29. (a) Schematic diagram of a symmetric WO ₃ ECS. (b) AFM and (c) SEM image of the as-deposited WO ₃ thin film. (d) and (e) XPS spectra of the WO ₃ thin film.....	44
Figure 2.30. (a), (b) and (c) three-dimensional schematic, cross-section and photo of co-anode PVCS. (d) and (e) three-dimensional schematic and photo of co-cathode PVCS. The red dashed boxes represent the active area of PSCs.....	46
Figure 2.31. Schematics of co-anode and co-cathode PVCS working mechanism. Original states of (a) co-anode and (d) co-cathode PVCS. At the original states, ECS parts are transparent and at a bleached states, which allow solar light to pass through. Initial charged states of (b) co-anode and (e) co-cathode PVCS: under the solar illumination, electric-fields are formed in the PSC parts which power the ECS. Electrons are injected into the WO ₃ cathode, and H ⁺ moves towards to the WO ₃ cathode driven by electric-field. Charges are stored at the WO ₃ cathode during the reversible oxidation reaction. The colors are starting to change. (c) and (f) Fully charged states: with the continuous light illumination, the PVCSs reach their fully charged states. The ECS color turns to blue, accompanying with the chemical state of W charging from 6+ (bleaching state) to 5+ (coloring state). These whole processes are reversible. After the discharging through external circuit, the reversible reduction process releases the charge and the WO ₃ thin film recovers to be transparent, thus the PVCSs recover to their bleached states.....	48
Figure 2.32. The photos of (a) Co-anode and (b) co-cathode PVCS color states under bleached, half charged and fully charged. Transmission spectra of PSC shelters in (c) co-anode PVCS and (d) co-cathode PVCS corresponding to different color states. Accompanying with energy storage, the color of PSC shelters changes from transparent to blue with a reduction in AVT from 76.2 % (68.7%) to 35.1 (23.0%) for co-anode PVCS and co- cathode PVCS, respectively. (e) Color coordinates of the PSC shelters with transmission spectra of 3(c) and (d) under AM 1.5 illumination plotted on the CIE xy 1931 chromaticity diagram.	50
Figure 2.33. (a) and (b)The <i>V-t</i> curves of the co-anode PVCS and co-cathode devices for the photo-charging process within 100 s and discharging process at a current density of 0.1mA/cm ² .(c) and (d) CV curves and GCD curves of a symmetric WO ₃ ECS.	53

Figure 2.34. (a) The areal capacitances as a function of different current densities. (d) The Ragone plot of WO ₃ ECS, showing the relationship between power density and energy density.	54
Figure 2.35. (a) Schematic illustration of the integration of the PSC with MAM anode and symmetric WO ₃ ECS connected by external wires. (b) V-t curves of photo-charging and discharging processes and the color changes during the processes.....	54
Figure 2.36. (a) A J-V curve of a commercial Si solar cell. (b) Photo-charging and discharging V-t curves of symmetric WO ₃ ECS integrated with the commercial Si solar cell.	54
Figure 2.37. The photovoltaic performances of the PSCs utilizing in the two PVCSs before integration, the bleached PVCS, and the colored PVCS. The <i>J-V</i> curves of (a) co-anode PVCS and (b) co-cathode PVCS, respectively. The PSCs in the PVCSs is at a low-power working state under the colored state of the PVCSs.	57
Figure 2.38. Photo-stability characterization of the as-fabricated PSC and the bleached/colored co-cathode PVCS during 5-hour continuous illumination: normalized 4 parameters (a) <i>V_{oc}</i> , (b) <i>J_{sc}</i> , (c) FF and (d) PCE as a function of the illumination time. The original values (0 min) of the 4 parameters are set as 1. The variations of the parameters with illumination time are normalized according to the values at 0 min.	59
Figure 3.1. Resistive switching behaviors. (a) Unipolar switching. (b) Bipolar switching. (c) Nonpolar switching. ^[1]	67
Figure 3.2 Schematics of the switching behavior in an oxide-based RRAM based on filamentary switching mechanism. ^[2]	71
Figure 3.3. Resistive switching behaviors in M/PCMP/SRO and M/Nb:STO/Ag devices. ^[25]	75
Figure 3.4. Schematics of switching mechanisms in CBRAM. ^[28]	76
Figure 3.5. Resistive switching behavior in Au/Nb:STO junction: IV characteristics and switching mechanism. ^[56]	80
Figure 3.6 (a) Schematics of a RRAM device with nanoparticle layer. (b) and (c) Resistive behavior in the Cu/ZnO/Cu(3 nm)/ZnO/Pt RRAM. ^[58] (d) and (e) Resistive switching behavior in the Al/Alq ₃ /Al(5 nm)/Alq ₃ /Al RRAM. ^[59]	81
Figure 3.7. Single-layer MoS ₂ based optoelectronic memory. (a) Device structure. (b) Optically programmed multi-level storage. (c) Band diagram illustrating the charge transfer between MoS ₂ and Au nanoparticles. (d) Retention properties. (e) Endurance tests. ^[66]	85
Figure 3.8. MoS ₂ optoelectronic memory for image sensing application. (a) Device structure. (b) Switching mechanism. (c) The linear relationship between output current and illumination time. (d) Data retention properties. ^[67]	85
Figure 3.9. An optoelectronic memory with structure of ITO/CeO _{2-x} /AlO _y /Al. (a) Schematics of switching mechanism. (b) IV curves of optical programming and electrical erasing. (c) Wavelength-dependent resistance states. (d) Multi-level data storage by controlling the light intensity and wavelength. ^[68]	86
Figure 3.10. (a) Schematic device structure of perovskite based RRAM. (b) The as-prepared perovskite thin film deposited on FTO glass substrate by one-step solution method, indicating good coverage of perovskite layer on the FTO glass. (c) XRD patterns of the as-prepared perovskite thin film. * represents the peaks of FTO glass. (d) XPS survey spectrum of the as-prepared perovskite thin film. (e) Narrow scan of Cl 2p core level and negligible signal of Cl 2p peak is detected. This suggests that most of the Cl escape with	

the form of intermediate phase.....	91
Figure 3.11. (a)The I-V characteristics of electrical switching behavior of perovskite based memory. (b) Cyclic tests for 50 cycles (c) Electrical reliability test for 12 h before and after electrical switching, showing no obvious degradation in HRS and LRS. (d) Cumulative probability plots for the SET and RESET voltages.	93
Figure 3.12. The I-V characteristics of low-voltage photo-assisted switching behavior of perovskite based memory. The SET process is conducted under the white light illumination with a power density of 3.20 mW/cm ² . The perovskite based memory then is RESET under the dark condition.....	95
Figure 3.13. Distributions of the average SET/RESET voltage and HRS/LRS.	96
Figure 3.14. Pulse switching endurance and (d) retention test for two resistance states. The pulse condition for HRS is 0.13 V for 100 μs with white light illumination (3.20 mW/cm ²) and for LRS is -1.6 V for 250 μs. The readout voltage is 0.05 V.	96
Figure 3.15. Stability tests of perovskite RRAM at the ambient environment with humidity of 50~55 %. (a) Electrical switching and (b) Optical switching.	96
Figure 3.16. The SET processes under different light intensities. (f) Light-intensity controlled multiple resistance states. The voltage pulse for the set processes is 0.13 V for 100 μs. The duration of optical pulses used is 1 s.	97
Figure 3.17. UPS spectra of perovskite thin film on FTO glass at (a) cut-off region and (b) valence band region obtained with $h\nu = 21.2$ eV. The binding energy is referred to the Fermi level. The work function is determined as 4.37 eV from the intercepts. A broad distribution of hole traps is observed above the valence band edge. The difference between valence band and Fermi level can be determined as 1.32 eV. (c) Absorbance spectrum of perovskite thin film on FTO glass and the bandgap obtained from the absorption edge is 1.63 eV. The band diagram of perovskite film is schematically illustrated in the inset of Figure 3.17. (d) The cut-off region in the UPS spectrum of FTO glass. The work function of FTO is calculated as 4.33 eV, which is considered to form an ohmic contact with perovskite layer.....	99
Figure 3.18. Variation of resistances at ON and OFF states of perovskite memory devices with different effective areas for (a) electrical switching and (b) photo-assisted switching. (c) electrical switching and (d) photo-assisted switching mechanism including four states: I. initial state corresponding to HRS: hole trapping centers locate at the perovskite surface; II. SET process: hole trap states are filled, shifting the Fermi level to the valence band; III. remove light electricity: a lowered barrier and quasi ohmic contact are resulted corresponding to LRS. IV. electrical reset: holes are extracted from the trap states and a transition from LRS to HRS occurs.	101
Figure 3.19. Demonstrations of logic operations and coincidence detection of the perovskite based memory. (a) A demonstration of AND logical operation. We defined the light pulse (>3.2 mW/cm ² , 1 s) as logic '1', light pulse (<0.3 mW/cm ² , 1 s) as logic '0', electrical pulse (0.13 V, 100 μs) as logic '1' and electrical pulse (0.01 V, 100 μs) as logic '0'. (b) A demonstration of OR logical operation. we define the light pulse (3.2 mW/cm ² , 1 s) as logic '1', light pulse (0.5 mW/cm ² , 1 s) as logic '0', electrical pulse (2 V, 250 μs) as logic '1' and electrical pulse (0.1 V, 100 μs) as logic '0'. HRS and LRS are defined as logic '1' and logic '0' in both AND and OR logic operations. (c) A demonstration of 3-pulse	

coincidence detection. Three input pulses are optical pulse (3.2 mW/cm^2 , 1s), electrical pulse applied to the top electrode (0.05 V, 1s) and electrical pulse applied to the bottom electrode (-0.05 V, 1s). The output current Y can represent the coincidence of the three input pulses. Only in the case that the three pulses appear coincidently, there shows an output current corresponding to the LRS of the memory device. 104

LIST OF TABLES

Table 2.1. Lists of internal resistance, energy density, average power density and areal capacitance of two types of PVCSs. The calculations are according to the discharge curve.	53
Table 2.2. Lists of V_{oc} , J_{sc} , FF and PCE extracted from the $J-V$ curves shown in the Figure 5(a) and 5(b).	57

CHAPTER 1 Introduction: Demands for Multifunctional Integrated Electronic Devices

Nowadays, smart-phone, smart-home, smart farming, smart transport and infrastructure systems have well-connected the world more than we ever thought possible. This intelligent network system is described as “Internet of Things (IoT)”. In the era of information explosion, IoT network expands rapidly, which brings data gathering and communication to existing and huge number of common objects via the Internet.^[1] The IoT objects are usually embedded with sensors for data gathering, actuators for action invoking, memories for data storage, processors for data processing and also wireless communication units for information transfer. ^[2]

With the rapidly increased number of IoT devices, IoT will drive unprecedented volumes and demands for the electronics industry. The number of connected devices worldwide is estimated to increase from 23.14 to 75.44 billion from year 2018 to 2025 in the IoT network.^[3] The dramatically increased number of IoT devices can consequently result in the increase of internet traffic. A multi-functional and highly integrated device can well benefit the IoT system operation and cater for the demands of smart device, such as reducing cost and device occupation area, and lowering energy consumption and electric loss.

Wireless sensor network (WSN) is the basis component in the IoT network system which gathers information from the IoT objects and long-term operation of wireless sensors requires continuous and sustainable supply of electric power. As the gradual

decrease of fossil fuels and global warming have posed threats to the sustainable development in human life, naturally renewable energies have been largely explored in recent years, *e.g.* solar energy, wind energy, wave energy, geothermal energy, tidal energy. However, these renewable energies are always intermittent and have variable outputs, and they rely on the weather conditions, which means it can only be used as it is generated. Considering from this concern, energy storage devices such as batteries and supercapacitors are essential and promising for balancing electricity supply converted from the intermittent renewable energies. Therefore, the integration of energy harvesting and storage devices plays a vital role in saving electric energy and providing environmentally-friendly sustainable electric energy to sensor nodes.

The sensory data collected by the wireless sensors from IoT objects is required further to be stored and processed. As conventional sensors, data storage and data processing devices are usually separated, the huge amount of IoT devices required can cause Internet traffic and require huge computing power consumption. To develop smart devices with integrated functions, such as sensing, data storage and data processing are demanded for reducing the power consumption in computing and data transfer, lowering the number of electronic devices and improving the data processing speed.

Therefore, considering from the two aspects discussed above, we will focus on designing two types of multifunctional and highly integrated electronic devices for IoT application in this thesis including: (1) multifunctional self-powered supercapacitors integrating solar cell and supercapacitors and (2) novel optically-controlled

multifunctional memory devices integrating light sensing, data storage and processing functions.

This thesis will introduce the projects accomplished during my PhD study from five parts: (1) Chapter 1 offers a brief introduction of project motivation (2) Chapter 2-5 introduce the three projects: Multifunctional Perovskite Photovoltachromic Supercapacitor, Low Voltage Optoelectronic Memory with Integrated Sensing and Logic Operation, UV-Switchable Transition Metal Oxide Optoelectronic Memory, respectively. (3) Chapter 5 summarizes the projects and gives an outlook for further studies.

References

1. Kortuem, G., F. Kawsar, V. Sundramoorthy, and D. Fitton, IEEE Internet Computing **2010**, 14, 44.
2. Bonomi, F., R. Milito, J. Zhu, and S. Addepalli. *Fog computing and its role in the internet of things*. in *Proceedings of the first edition of the MCC workshop on Mobile cloud computing*. 2012. ACM.
3. Madakam, S. and H. Date, *Security mechanisms for connectivity of smart devices in the internet of things*, in *Connectivity Frameworks for Smart Devices*2016, Springer. p. 23.

CHAPTER 2 Multifunctional Solar-Powered Supercapacitor

2.1 Introduction

Integration of energy harvesting and storage systems play a significant role in the IoT applications for providing continuous and sustainable energy sources for sensors, reducing electrical loss during power transmission and device occupation area. This project is focusing on integrating novel and low-cost solar cells and electrochromic supercapacitor into one device configuration and realizes a multifunctional solar-powered supercapacitor. This introduction section will first briefly review the working principle and materials for supercapacitor, followed by the introduction of a novel multifunctional electrochromic supercapacitor which will be employed in the integrated systems and finally will the developments of solar-powered supercapacitor reported till now will be reviewed. Followed with the introduction, our designed multifunctional perovskite photovoltachromic supercapacitors will be introduced and discussed in the section 2.2.

2.1.1. Energy storage devices

Batteries and supercapacitor are the two most promising and reliable energy storage devices in electrochemical energy storage. Batteries and supercapacitor adopt similar device structure including anode, cathode, separator and current collectors. However,

the two devices exhibit obvious difference in the energy storage performances.

Current rechargeable batteries include lead–acid, Ni–Cd, Ni–MH, lithium ion batteries (LIBs), which store energy based on the redox reaction occurred at the electrode material. Figure 2.1 a shows a generally working mechanism in the batteries. As diffusion process dominates in the redox reaction, the slow process enables high energy density of 100~265 Wh/Kg, but a low power density of <1500 W/Kg for LIBs. Also, due to the destructive electrochemical process at the battery bulk electrode, cycling ability of batteries is poor (500~1000 cycles for LIBs). For supercapacitors, according to different charge storage mechanisms (Figure 2.1b), it can be classified into electrical double-layer capacitors (EDLC) and pseudocapacitors, for which charges are stored based on electrical double-layer effect and redox reactions, respectively. Since the reaction or electrical double-layer effect occurs at electrolyte/electrode interface, the charge insertion/extraction or electrostatic induction is very fast which leads to an ultra-high power density of 3000~40000 W/Kg and ultra-long cycle life up to 10^7 , but a relatively lower energy density of 4~10 Wh/kg. Interestingly, in previous reports, Dunn *et al.* have also reported some special materials, which can help to achieve battery-like supercapacitor behavior. For examples, pseudocapacitors based on Nb₂O₅ exhibit fast cation intercalation and de-intercalation^[1], which behaves with both high capacitance and charging/discharging rate (Figure 2.1c).

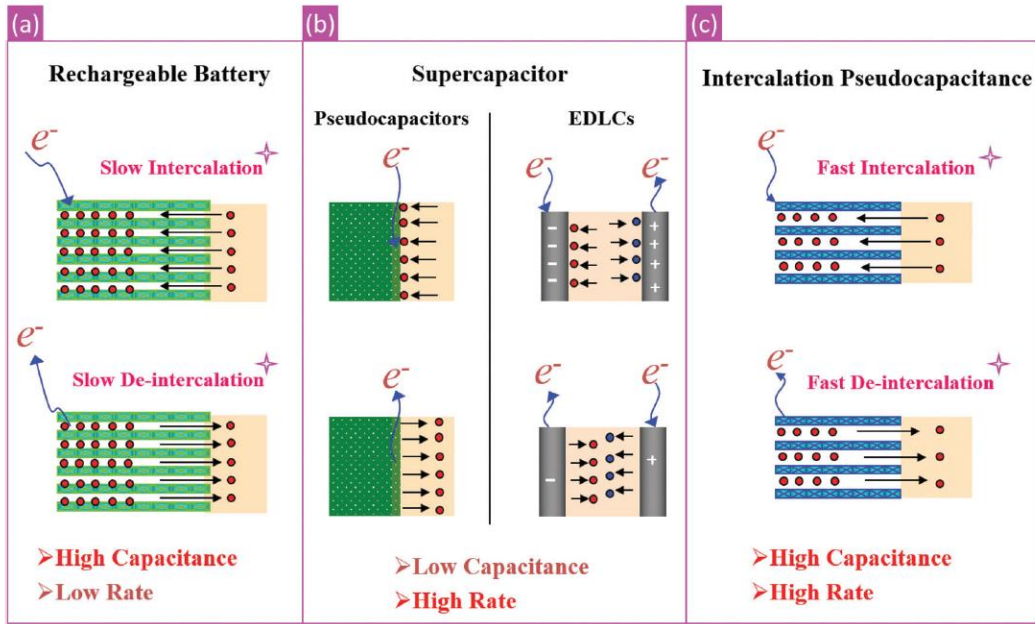


Figure 2.1. Charge storage mechanisms of rechargeable battery, supercapacitor and intercalation pseudocapacitance.

A Ragone plot of energy density and power density of various energy storage devices is demonstrated in the Figure 2.2.^[2] Supercapacitor locates between batteries and traditional capacitors. Taking the advantages of higher power density and long cycle life of supercapacitors, this chapter will mainly introduce the operations of supercapacitors in the later part.

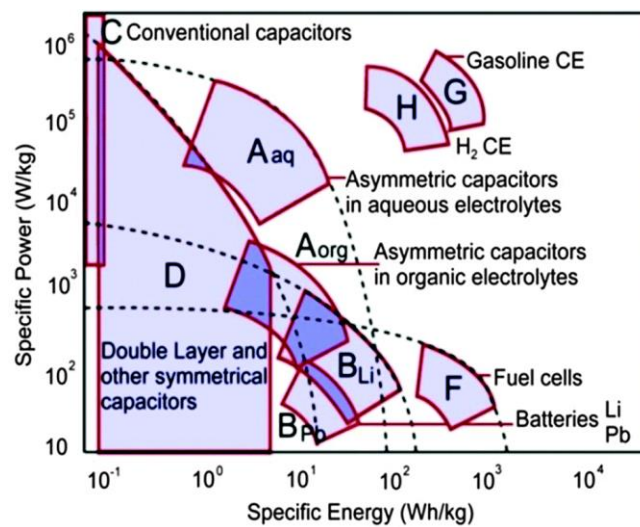


Figure 2.2. Ragone plot with energy density vs power density of various energy storage devices.^[2]

2.1.1.1. Supercapacitors: working principles and materials

Supercapacitors can be classified into three types: EDLCs, pseudocapacitors and hybrid capacitors, which corresponding to non-Faradaic mechanism, Faradaic mechanism and a combination of non-Faradaic and Faradaic processes, respectively [3]. Faradaic processes involve charge transfer and oxidation/reduction reactions. Non-Faradaic process does not involve the chemical reaction and generally store charge electrostatically.

Similar to the traditional capacitor, EDLCs store charges through electrostatic effect. A schematic of working process is illustrated in Figure 2.3. Under an electric field, ions provided by electrolyte move towards to the electrodes, accumulate on the electrode surfaces and are separated by the dielectric separator. A double-layer of charge is formed at the electrode. Since no charge transfer between the electrolyte and electrode and no volume loss or no damage in morphology in the electrodes, the whole processes is non-Faradaic, leading to a long cycle life and high power density. Because of the excellent cycle life time, EDLCs can be well employed in non-user serviceable locations (*e.g.* mountains) [4-6]. The electrochemical performances of EDLCs are closely related to the electrolyte used. Aqueous and organic electrolyte can both be utilized in EDLCs. Compared with organic electrolyte, the use of aqueous electrolyte (*e.g.* H₂SO₄ and KOH) is more environmentally friendly and has lower ESR. The requirement of pore size of electrode material in EDLCs with aqueous electrolyte is lower than that with organic electrolyte. However, the breakdown voltage in water-based electrolyte system is much lower than organic electrolyte system because of the hydrolysis.

Because of the trade-off between lower ESR and larger voltage window, the choice of electrolytes is dependent on the specific applications.

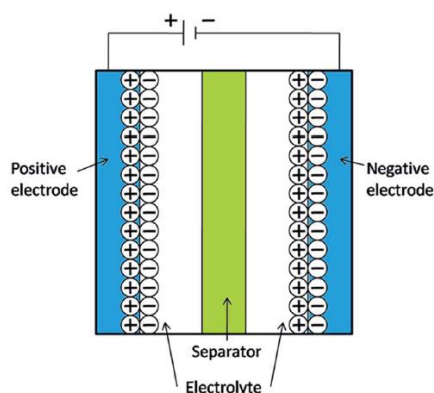


Figure 2.3 Schematics of working mechanisms of EDLCs.^[7]

As for the material systems in EDLCs, carbon electrode is the most commonly used material for its large surface area, easy fabrication process, high chemical stability, good electrical property, low cost and wide operating temperature range.^[8] Other types of carbon materials, such as activated carbons, carbon aerogels, carbon nanotubes (CNTs) and graphene have also been widely applied in the EDLCs.^[9] Due to a large specific surface area of porous activated carbons ($>2000 \text{ m}^2/\text{g}$), the capacitances of EDLCs can reach around 100 F/g and 200 F/g in aqueous and organic electrolytes, respectively.^[10] Further improvements have been done by using a hierarchical porous carbon with high specific surface area of $\sim 2700 \text{ m}^2/\text{g}$. The specific capacitance for the as-prepared capacitor reaches 307 F/g.^[11] For CNTs, although high electrical conductivity of CNT also enables it as promising electrode material for achieving good electrochemical performances, the relatively small surface area limits the capacitance (30~80 F/g).^[12, 13] 2D graphene has also demonstrated great potential in the supercapacitor applications for the excellent electrical conductivity and high charge mobility. The graphene based supercapacitor even exhibits similar performances to the

traditional capacitors. [14]

In contrast to EDLCs, pseudocapacitors store charges based on the Faradaic processes, which involves in the charge transfer between electrolyte and electrode. The Faradaic processes that may occur at the electrode includes: redox reaction (transition metal oxides, adsorption of ions, electrochemical doping (conducting polymers). Compared with EDLCs, pseudocapacitors adopt higher energy density and capacitance since that the Faradaic processes can also occur inside the electrode material. However, the redox reaction involved leads to a poorer cyclic performance and lower power density. [7]

Metal oxides are class of materials that have been widely used in pseudocapacitors, such as NiO, $\text{WO}_3 \cdot \text{H}_2\text{O}$, $\text{MnO}_2 \cdot \text{H}_2\text{O}$, V_2O_5 , Co_3O_4 , $\text{RuO}_2 \cdot \text{H}_2\text{O}$, $\text{IrO}_2 \cdot \text{H}_2\text{O}$, SnO_2 and Fe_2O_3 . [15] Hydroxides (*e.g.* $\text{Co}(\text{OH})_2$ and $\text{Ni}(\text{OH})_2$) are also common materials for pseudocapacitors application. [16] Ru-based electrodes have demonstrated remarkable performance. The redox reaction at Ru-based electrodes requires successive electron transfer with the valance change from Ru^{4+} to Ru^{3+} to Ru^{2+} . The CV curve of Ru-based supercapacitor usually presents a rectangular shape, similar to the EDLCs. [17] Colloidal ruthenic acid nanosheets have been reported by Sugimoto *et al.* with higher electrode kinetics than the electrode used in batteries. [18] The supercapacitor also exhibits high capacitance of 601 F/g at a scan rate of 50 mV/s, which may be attributed that interlayer surfaces are also usable for charge storage. Hu *et al.* synthesized $\text{RuO}_x \cdot n\text{H}_2\text{O}$ nanoparticles and deliver a high capacitance of 1084 F/g at a current of 0.5 A/g. [19] Although Ru-based electrode has presented excellent properties, the environmental

harmfulness it brings limits the further applications in the supercapacitors. To cater for the application requirements, then materials that are cheaper and more environmentally friendly are developed, such as MnO₂. The theoretical capacitance based on MnO₂ can reach 1100 F/g.^[20, 21] Since the redox reaction MnO₂ involved is occurred at the surface instead of the intercalation in bulk material, the capacitance of MnO₂ cannot be comparable with RuO₂ and requires further improvements. Different MnO₂ nanostructures (porous structure^[22], nanotubes^[23], nanowires^[24] and microspheres^[25]) have been fabricated with showing improved performances. For example, porous α -, β -, and γ - MnO₂ exhibit a capacitance from 70 to 90 $\mu\text{F}/\text{cm}^2$. β - MnO₂ demonstrates better rate ability, which may be attributed to the faster ion transport.^[22] The supercapacitor based on a nanostructured MnO₂/CNT composite on a sponge exhibits high capacitance of 1230 F/g and excellent cycling stability (more than 10000 cycles).^[26] Except for MnO₂, V₂O₅ is another alternative for RuO₂. Guo *et al.* synthesized V₂O₅@C core-shell nanowires and demonstrated a high areal capacitance of 128.5 F/cm².^[27] The supercapacitors with V₂O₅/graphene electrode can also achieve a specific capacitance of 486 F/g and energy density of 68 Wh/kg.^[28]

In addition to the above metal oxides discussed, conducting polymers (*e.g.* polyaniline (PANI), poly(3,4-ethylenedioxythiophene) (PEDOT) and polypyrrole (PPy)) have also been a class of promising electrodes for pseudocapacitors. The redox reactions involved in the conducting polymer based supercapacitor will not cause the structural changes and are highly reversible. Additionally, the redox reaction can only happen at the surface, but also the through the bulk material. Among the conducting

polymers for pseudocapacitors, PPy and PANI are most widely used considering from the synthesis complexity, cost and chemical stability. PPy and PANI are usually employed as positive electrode since they can only be p-doped. To n-dope the two materials require the voltage much larger than a common electrolyte can achieve. The pseudocapacitors with conducting polymer electrodes have reported with excellent properties. For example, the PANI hydrogel electrodes deliver a capacitance of 750 F/g at a constant charging/discharging current of 1A/g.^[29] The solid-state supercapacitor based on PPy synthesized on stainless steel mesh exhibits a capacitance of 170 F/g.^[30] However, a challenge of the application of conducting polymers is the swell/shrink problem during the intercalation/de-intercalation processes. This can lead to a low cycling lifetime. To improve the cycling performances, researchers have composited the conducting polymers with other materials. Zhao *et al.* found that the PANI/porous carbon composite can exhibit a high capacitance of 531 F/g. It is worthy to mention that there is only 3 % degradation in capacitance after 10⁴ cycles. Later research work also designed a 3D PANI/graphene composite and delivers long cycling life time and excellent capacitance of 531 F/g.^[31]

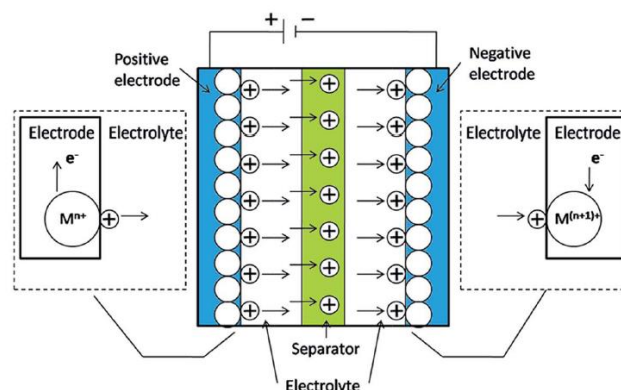


Figure 2.4. Illustration of a typical working mechanism in the pseudocapacitors. ^[7]

2.1.1.2. Electrochemical characterizations

Cyclic voltammetry (CV)

Cyclic voltammetry (CV) test is a typically potentiodynamic electrochemical measurement. Three-electrode setup (reference electrode, working electrode and counter electrode) is usually employed for characterizing the electrode electrochemical performances. As to determine the electrochemical performances for a two-terminal device, two-electrode setup (reference electrode and working electrode) is generally used. CV plot illustrates the variation of current as a function of a cycle of sweeping voltage. The sweeping voltage is the working electrode potential against to the reference electrode and the current described in the CV measurement is the current flowing through the working electrode.

Usually, the working electrode potential ramps linearly with time, as shown in Figure 2.5a. The potential first linearly increases from E1 to E2 and then reversely sweeps back to E1. Figure 2.5b shows a typical CV curve corresponding to the voltage sweeping in. A cathodic peak and anodic peak can be clearly observed in the figure, corresponding to a reduction reaction and redox reaction, respectively. These featured peaks can be attributed to the diffusion layer formed near the electrode and reflects the change of charge concentration gradient with the voltage. As a voltage is swept, electrons begin to flow and as a redox/reduction reaction happens, the current ramps rapidly and reaches a peak. The thermal equilibrium at the electrode surface can be expressed by Nernst equation:

$$E = E^\theta + \frac{RT}{nF} \ln \frac{(R)}{(O)} \quad 2.2.1$$

Where E is the applied potential is difference and E^θ is the standard electrode potential. The above discussion is for a Faradaic process, as for a non-Faradaic process (EDLCs), no redox reaction peaks appear in the CV curve. A comparison of Faradaic and non-Faradaic CVs has been discussed in the Chapter 1.

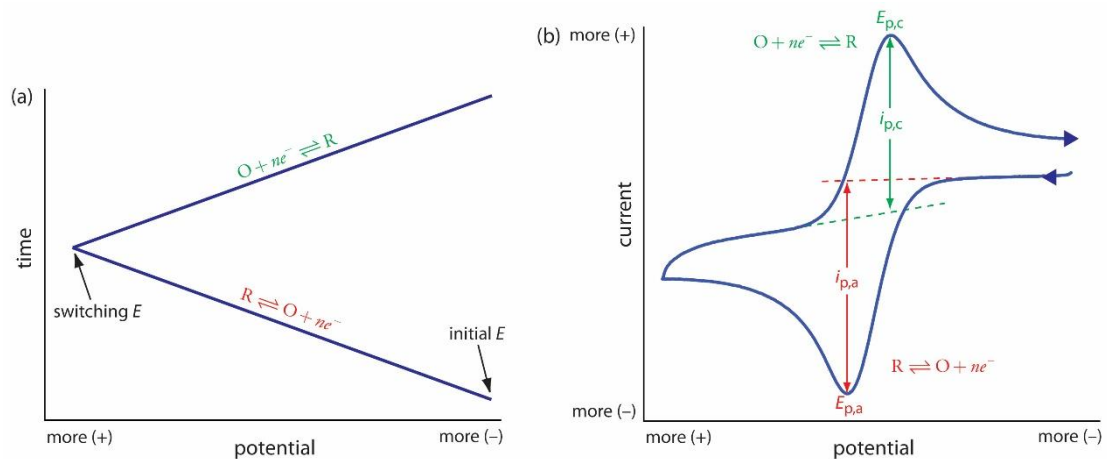


Figure 2.5 (a) Voltage (E) vs time (t) in the CV measurements. The voltage ramps linearly with time. (b) A typical CV curve corresponding to the voltage sweeping in (a).^[32]

CV plot is an important method to determine the capacitance of an electrode or an energy storage device. The capacitance C of an electrode material or a supercapacitor device can be calculated as below:

$$C = \frac{\int IdV}{vmV} \quad 2.2$$

Where I is the current, V is the applied potential, v is the scan rate and m is the mass of the electrode material or the supercapacitor.

Galvanostatic discharge/charge (GCD)

Galvanostatic discharge/discharge (GCD) measurement is another reliable method to extract the capacitance in an electrode material/supercapacitor and examine the maximum and minimum charge/discharge current rate the electrode

material/supercapacitor can withstand. In the GCD measurement, a constant current is applied to charge an electrode material/supercapacitor and the potential in the electrode/supercapacitor as a function of charging/discharging current can be recorded. The extraction of capacitance from GCD is more efficient and it can be calculated as shown below:

$$C = \frac{I\Delta t}{m\Delta V} \quad 2.3$$

Where I is the discharge current, m is the mass of an electrode or a supercapacitor, Δt stands for the total discharge time and ΔV represents the working voltage window. The energy density of a supercapacitor can also be calculated from the GCD curve:

$$E = \int_{t_1}^{t_2} IV dt = \frac{1}{2}C(V_1 + V_2)(V_2 - V_1) \quad 2.4$$

V_1 and V_2 are the end of charging voltage and discharging voltage, respectively. Figure 2.6 demonstrates the difference in calculating the energy density for EDLC and hybrid supercapacitor from the GCD curves.

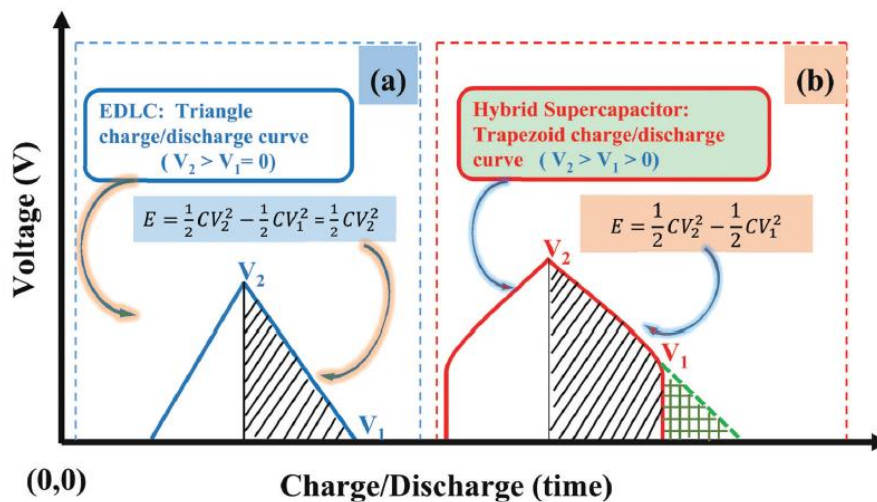


Figure 2.6. Typical GCD curves for EDLCs and hybrid supercapacitor. ^[10]

2.1.2. Smart supercapacitor: electrochromic supercapacitor (ECS)

2.1.2.1. Electrochromism & traditional electrochromic cell

Electrochromism can be employed to describe the color change phenomena under a voltage for an electrochromic material. The basic principles of electrochromism involved are the charge insertion/extraction or redox/reduction reactions. Electrochromic materials has drawn great attention in the industry for their great potentials in smart windows application (or also called “electrochromic window”). Smart window can be used to describe the window that has electrochromism, which means it can change its optical transmittance under the external voltage. Smart windows are basically an electrochromic cell (also an electrochemical cell), in which two electrodes are separated by an electrolyte material. A schematic structure of an electrochromic cell is illustrated in Figure 2.7.^[33] The electrochromic cell consists of two transparent electrodes, an electrochromic layer, electrolyte and separator and a counter electrode. At the open circuit condition, the device is semi-transparent, allowing light and heat to transmit through. As a voltage is applied, ions in the electrolyte move towards to the electrode and redox reaction/charge insertion occurred at the electrochromic material. The redox reaction/charge insertion is accompanied with color change. A counter electrode is employed for balancing the charges. At this state, the electrochromic cell turns to deep color, which prevents light and heats.

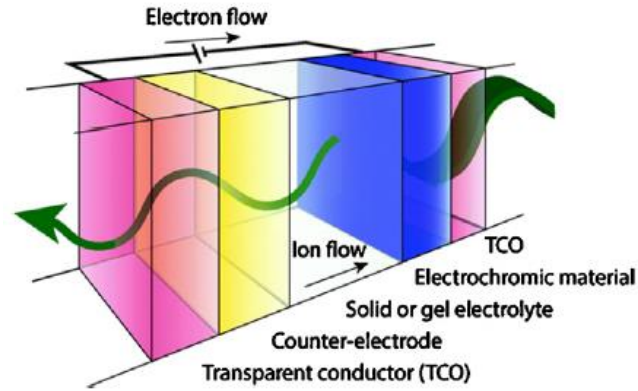


Figure 2.7. A schematic of electrochromic cell.^[33]

The smart windows can modify the sunlight into a room or building for saving energy and avoiding the light pollution. The color of smart windows can be tuned from clear to dark at different levels according to people's requirements and weather conditions, which brings more comfortable inside environments to people. The characteristics of color change are also appropriate for other application scenarios expect for the building architecture, such as air planes, sunglasses, vehicle windows and displays.

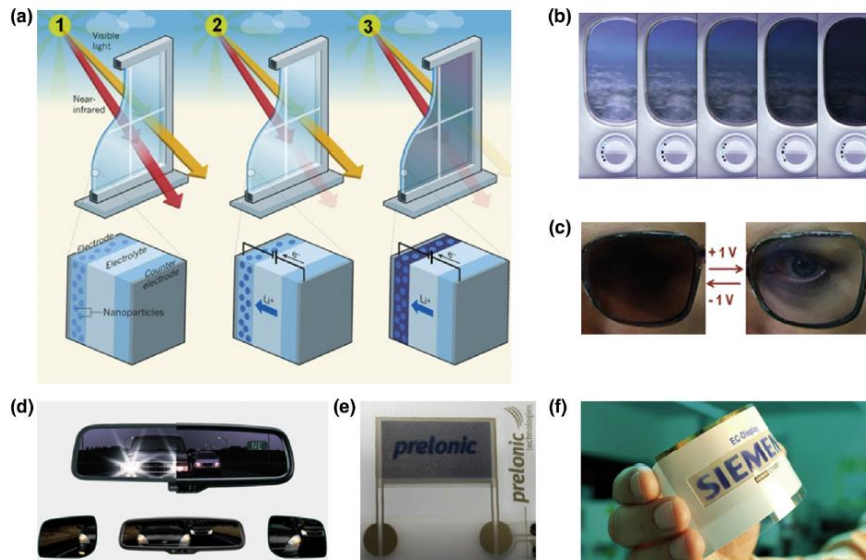


Figure 2.8. Applications of electrochromic windows.^[34, 35]

2.1.2.2. Integration possibilities for electrochromic supercapacitor (ECS)

As the device structure and operation mechanism are similar to supercapacitors, it is possible to integrate an electrochromic cell with energy storage. Briefly, as the redox reaction or charge insertion occur at the electrochromic layer, the color of the electrochromic material can change, accompanied with charge storage in the electrochromic layer. In this case, charge storage/release and color change/bleach can occur simultaneously. This type of device can be named as electrochromic supercapacitor (ECS). In the ECS, the color can indicate the amount of energy stored or released. Then the energy level can be “visible”, which provides much convenience in the supercapacitor daily use. Furthermore, the working scheme of the electrochromic cell can make best use of the energy. As a “dark mode” of the smart window is required, energy can also be stored in the device and as if the “bright mode” is required, the stored energy can be utilized to power other devices. Thus, the integration of electrochromic cell and supercapacitor provides great potential in multi-functional device applications. The successful integration and ECS device fabrication is from 2012.

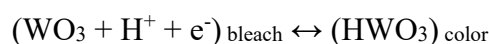
2.1.2.3. Material candidates

(1) Metal oxides

As the working mechanism of electrochromic cell is very similar to pseudocapacitors, metal oxides are also a common class of materials for ECS applications. The electrochromic oxides can be classified into cathodic electrochromic

oxide and anodic electrochromic oxide, according to the electrochromic material as cathode and anode, respectively.

Tungsten oxides are the most widely used cathodic electrochromic materials in the ECS. The reaction that tungsten oxides involved can be expressed below:



This reaction is based on the proton contained electrolyte. Li^+ based electrolyte can also be used for WO_3 coloration. In the ECS device, another important parameter which describes the electrochromism characteristics is the coloratio efficiency (CE):

$$\text{CE}(\lambda) = \frac{\Delta OD}{Q} = \frac{\log\left(\frac{T_b}{T_c}\right)}{Q}$$

Where OD stands for optical density and ΔOD is the change of optical density, T_b and T_c are the transmittance at a certain wavelength in the bleached state and colored state, respectively. The obtained CE is fixed at a certain wavelength λ , Q is the amount of charge insertion or extraction.

Yang *et al.* first emphasized a combination of electrochromic cell and supercapacitor based on WO_3 electrodes prepared by thermal evaporation in 2014. Both excellent capacitance and coloration efficiency are obtained in WO_3 electrode. More specifically, WO_3 electrode exhibits a coloration efficiency of $54.8 \text{ cm}^2\text{C}^{-1}$ and an abrupt change in transmittance from 91.3 % to 15.1 % at a wavelength of 633 nm. It shows fast color response with coloration time of 3.1 s and bleach time of 0.9 s (at an alternative voltage of $\pm 0.6 \text{ V}$ vs Ag/AgCl). The capacitance of a solid-state symmetric WO_3 supercapacitor can reach 160 F/g .^[36] It is worthy to mention this ECS is distinct to the previous WO_3 electrochromic cell reported. For the WO_3 electrochromic cell, as

a negative voltage can color the device (deep blue), only as a positive voltage is applied, the device can be bleached. However, in WO₃ ECS, the device can be recovered to semi-transparent state by consuming all the power or discharging the device to 0 V. Thus, a reverse voltage bias is not required to bleach the device. Later Zhu *et al.* synthesized WO₃ layer by solution-based electrodeposition method and quantitatively determine the energy storage with some simple transmission measurements. The different color change levels and corresponding optical transmission can well-indicate the exact amount of energy in the supercapacitor.^[37] Shen *et al.* fabricated WO₃/Ag nanowire composites on flexible substrates. The flexible ECS device reaches a high coloration efficiency of 80.2 cm²/C and capacitance of 138.2 F/g (13.6 mF/cm²).^[38] In addition to WO₃, Nb₂O₅ and TiO₂ are also common cathodic electrochromic material used in electrochromic cells. However, currently there is no investigations that report an electrochromic supercapacitor based on the two materials.

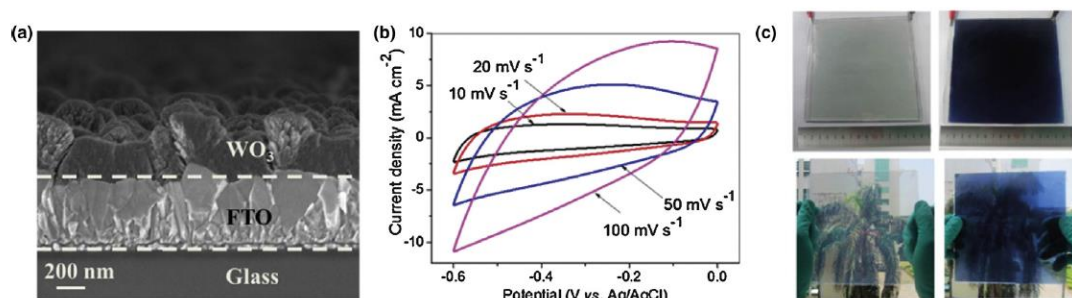


Figure 2.9. Multifunctional WO₃ electrochromic supercapacitor reported by Yang *et al.*^[36]

As for the anodic electrochromic material, nickel oxides have drawn great attention for the low cost and good cycling stability. The reaction involved can be expressed as below:



This expression is based on proton based electrolyte. Wen *et al.* reported both electrochromism and charge storage capacity in the NiO_x films prepared by sputter technique, as shown in Figure 2.10. The measurements are conducted in LiClO₄-propylene carbonate (PC) electrolyte. It has been found the charge exchange in NiO_x is mainly due to the surface process and both cations and anions are involved in the processes.^[39] This is distinct to the previous reports based on NiO and WO₃. This new working scheme provides further possibilities in realizing high-performance ECS device. Manganese oxide (MnO_x) is another possible electrochromic electrode for ECS, which has been reported with good coloratio efficiency of 41.7 cm²/C.^[40] However, till now, although the separate devices MnO_x electrochromic cell and MnO_x supercapacitor have been demonstrated, no studies integrating the electrochromic properties and good energy storage capabilities into one device have been reported.

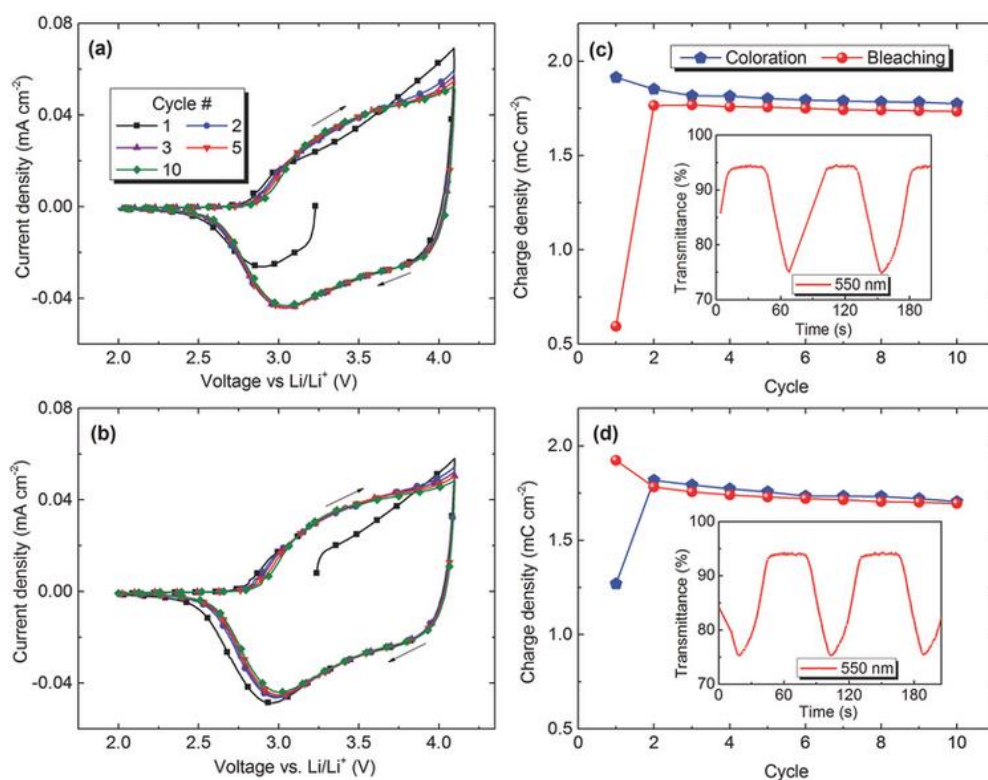


Figure 2.10. Electrochromism and energy storage properties in NiO_x.^[39]

In addition to cathodic electrochromic material WO_3 and anodic electrochromic material NiO for ECS device, Vanadium pentoxide (V_2O_5) is a special material which can be both cathodic and anodic electrochromic material. Wei et al. reported a symmetrically gyroid-structured V_2O_5 ECS device, which demonstrates both good electrochromic performance and energy storage capability. The optical transmittance can be tuned within the range of 30 % to 80 % at the wavelength of 700 nm. A high capacitance of 155 F/g can be achieved in the lithium salt electrolyte. [41]

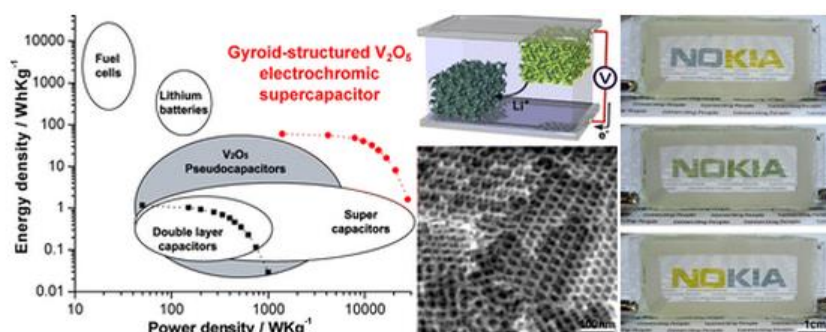


Figure 2.11. Energy storage performances and electrochromism in the V_2O_5 ECS. [41]

(2) Conducting polymers

Conducting polymers, which offer advantages of low cost, fast color response time and high coloration efficiencies, have also drawn great attention in ECS device fabrication. [42-44] PANI and PPy are two commonly used conducting polymers for electrochromic materials. An energy storage smart window integrating energy storage and electrochromic function based on PANI nanowires as electrode was first reported by Wang *et al.* This device exhibits a capacitance of 17 mF/cm^2 at a scan rate of 5 mV/s . As the device was charged to 0.7 V, the color changes from yellow to green and as it was discharged, the green color will be recovered. This multifunctional energy storage smart window can be potentially used as smart windows for vehicles, roofs or rooms. [45]

In addition to PANI, the wide tunable colors render PPy as a promising candidate for ECS device. The insulating PPy is yellow-to-blue color and while it is doped to conductive state, the color can change to blue-to-violet. Reddy *et al.* fabricated an ECS based on a derivative PEDOP of PPy. The electrode employed in this device design is PEDOP-Au@WO₃. Figure 2.12 shows the transmittance of PEDOP-Au@WO₃ film vs applied voltage and time, which demonstrates both electrochromic and energy storage capabilities. [46]

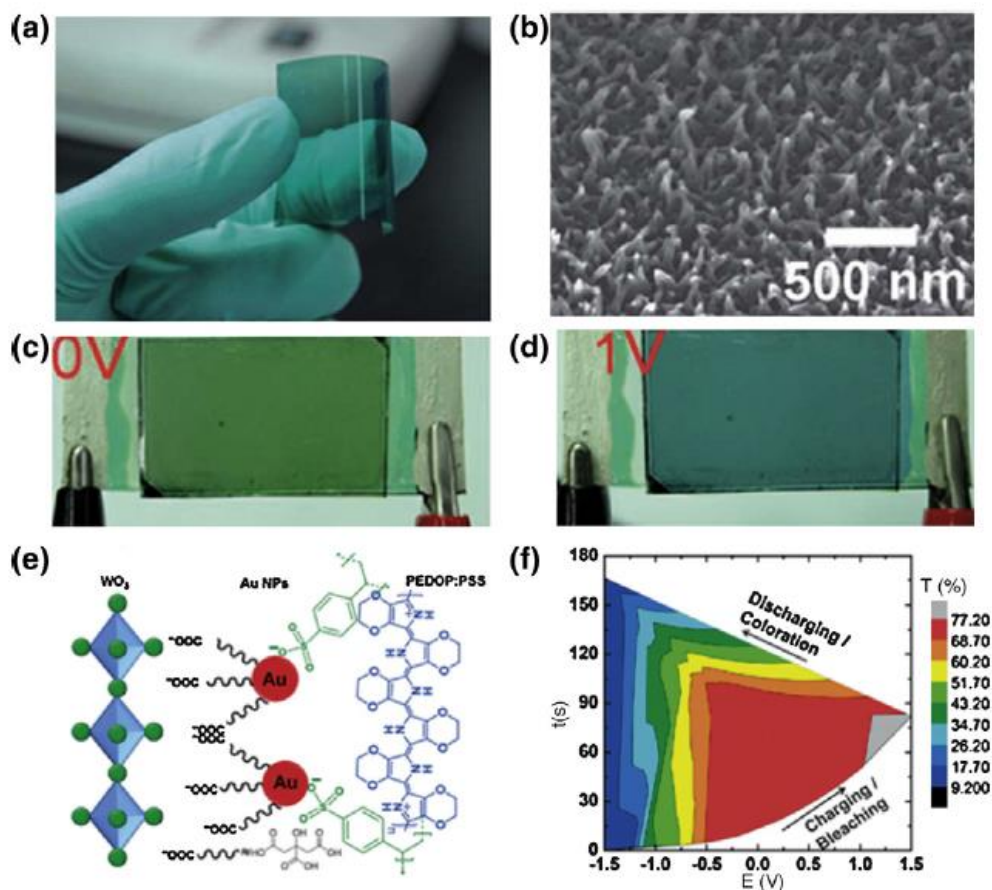


Figure 2.12 Conducting polymers for electrochromism and energy storage (a)-(d) PANI energy storage smart window.^[45] (e) Schematics of PEDOP-Au@WO₃ structure. (f) Optical transmittance of PEDOP-Au@WO₃ electrochromic material vs voltage and time.^[46]

(3) Inorganic non-oxides

Prussian blue (PB) have been a promising material in electrochromism,

electrocatalysis and energy storage. Lou group designed a self-powered rechargeable battery, which is also an electrochromic cell. The device can be self-colored and self-bleached by connecting and disconnecting the aluminum (Al) and PB electrodes, respectively. As connecting Al and PB, PB can be reduced to Prussian white in KCl electrolyte; as disconnecting Al and PB, PW can be oxidized to PB due to the oxygen dissolving in the electrolyte.^[47] This color change process and variation in optical transmittance are illustrated in Figure 2.13 (a) and (b).

In recent years, graphene-based material has drawn rising attentions in energy storage device. Previously, Polat *et al.* have demonstrated different types of electrochromic cells based on multilayer graphene.^[48] In a recent work, Hu *et al.* investigated the influences of Li⁺ intercalation/de-intercalation on electrical and optical properties of 3-60 layer-graphene. With the Li⁺ intercalation, the conductivity and optical transmittance have increased dramatically. This phenomena offers a promising method for designing an ECS device.^[49]

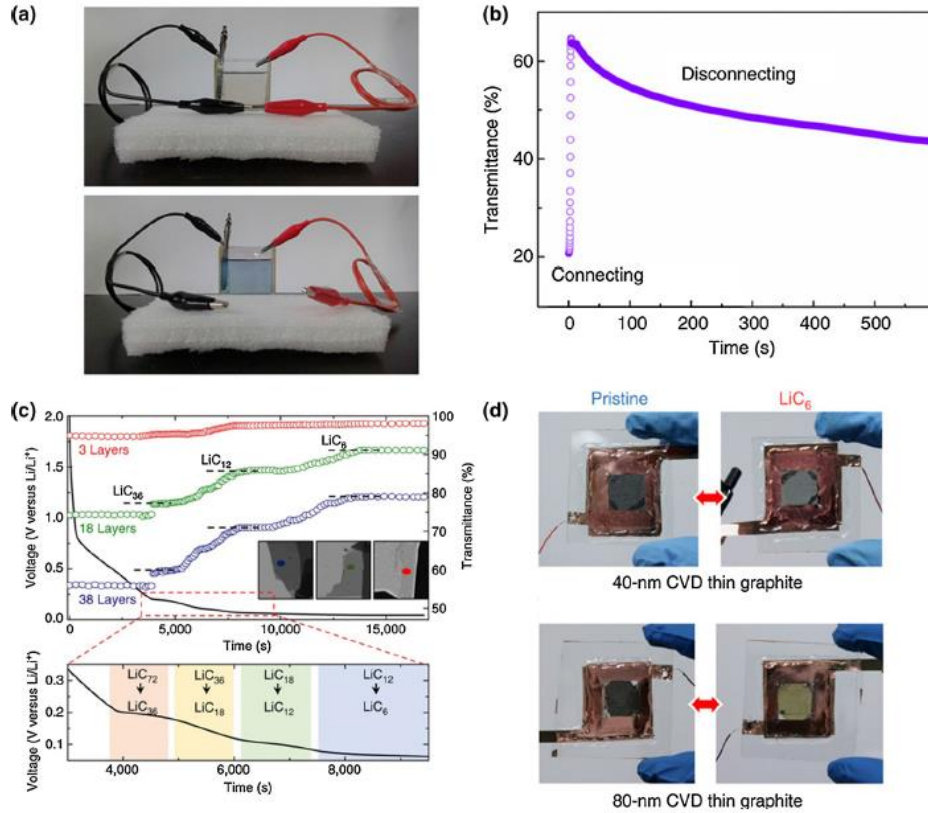


Figure 2.13. (a) and (b) optical photos and *In situ* optical transmittance of Prussian based ECS device.^[47](c) and (d) Optical transmittances during Li intercalation process and photos of color change before and after the intercalation process.^[49]

2.1.2.4. Challenges and outlook

Electrochromic supercapacitor can change their color and store energy during the same process, which is more superior to the single electrochromic cell and supercapacitor/batteries considering from the functions it possesses. However, the high electrochromic characteristics are contradictory with high energy storage capabilities. A low charge density is required for realizing high coloration efficiency and fast switching response; while a high charge density is essential for a supercapacitor or battery. Thus, there is a trade-off between electrochromism and energy storage. More techniques are desired to be developed to realize an ECS with both good

electrochromism characteristics and energy storage capability.

2.1.3. Integration of energy harvesting/storage systems

The developments of self-powered systems that harvest the driving energy from the nature environments are demonstrating great potentials in the future smart, portal and wearable electronics. Especially, the self-powered electrochemical energy storage systems are essential for providing sustainable energy for various electronics. There have been different types of self-powered energy storage systems reported, such as solar powered,^[50] and piezoelectric,^[51] triboelectric^[52] or pyroelectric-driven,^[53] supercapacitors/batteries. Among the energy harvesting systems, solar energy is considered as one of the greenest and abundant renewable energy source. This section will mainly review a development of solar powered energy storage systems.

2.1.3.1. Solar powered supercapacitors

The energy harvesting and conversion of solar energy can be directly completed by the solar cells and then be stored in the supercapacitors/batteries. In the past decades, due to the high-cost and fabrication complexity of Si solar cells, dye-sensitized solar cells (DSSCs) ^[54, 55] and polymer solar cells^[56, 57] have received increasing attentions and have been widely investigated in the energy harvesting/storage applications.

The most important parameters that represents the energy harvesting/conversion capability is the energy conversion efficiency $\eta_{\text{conversion}}$, which is defined as:

$$\eta_{\text{conversion}} = \frac{FF \times V_{OC} \times J_{sc}}{P_{in}}$$

Where FF is the fill factor, V_{OC} is the open circuit voltage and J_{sc} is the short circuit current of solar cells. Figure 2.14 shows a typical J-V curve of solar cells with and without light illumination, where V_{OC} and J_{sc} are indicated.

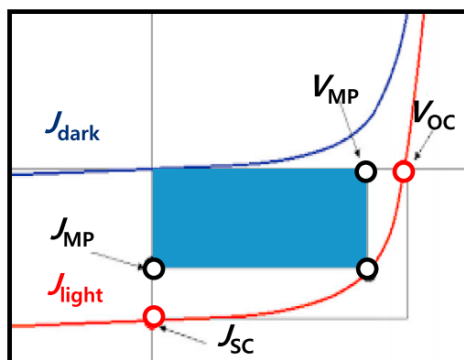


Figure 2.14. A typical J-V curve of solar cells with and without light illumination.

DSSCs are first reported in 1991 for its low-cost and simple fabrication processes.^[58] Till now, the highest $\eta_{\text{conversion}}$ for DSSCs reported is 14.3%.^[59] Figure 2.15 describes a typical DSSC and energy diagram.^[60, 61] Briefly, as light is illuminated and absorbed by the dye. Pairs of electrons and holes are generated. The electrons are then injected into the conduction band of TiO_2 and are collected. The collected electrodes flow through the external circuit to Pt electrode. At the cathode, after receive an electron from Pt electrode, I_3^- is reduced to I^- in the electrolyte. The oxidized dye then will be reduced to the neutral state after receiving an electron from I^- . DSSCs have been widely used in the integration of energy harvesting and storage devices for its easy fabrication processes.

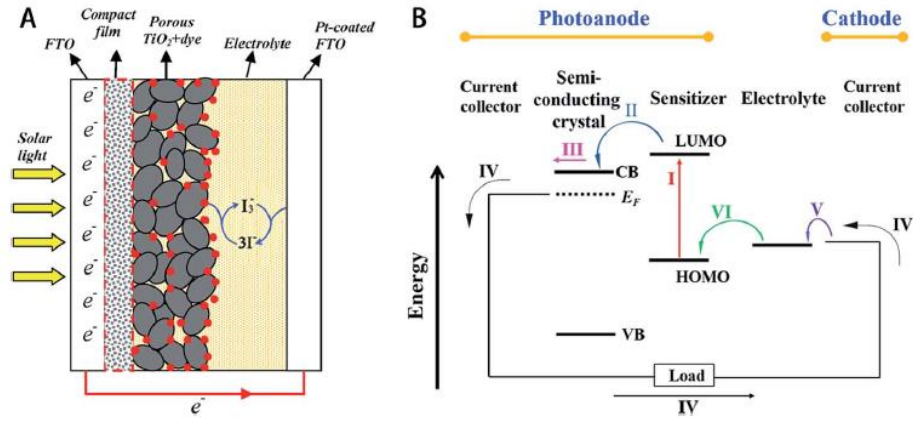


Figure 2.15. (a) Schematics of a DSSC.^[60] (b) Energy diagram of a typical DSSC.^[61]

The simplest way to integrate an energy harvesting device and an energy storage device is to connect the two devices through the external circuit. However, the two separated devices are space consuming and limit the practical applications. To this end, the integrated devices in fiber shape are developed and have been received with increasing attentions. Yang *et al.* first reported a fiber-shaped DSSC powered CNT supercapacitor (Figure 2.16).^[62] By connecting terminal 12 and 34, under the light illumination, the supercapacitor can be photo-charged to 0.65 V within 1 s. The charging current and charging voltage of the supercapacitor are determined by the solar cells. To discharge the device, terminal 15 and 46 are connected and the supercapacitor can be discharged for 41 s at a constant discharging current of 0.1 A/g. The fiber-shaped integrated device also performances well even under stretching and bending. An overall efficiency of energy conversion and storage in this device reaches 1.83%. The overall efficiency can be calculated as:

$$\eta_{overall} = \frac{E_{output}}{E_{input}} = \frac{0.5 \times C \times V^2}{P_{in} \times S \times t_c \times \eta_{conversion}}$$

$$\eta_{overall} = \eta_{conversion} \times \eta_{storage}$$

Where C is the supercapacitor capacitance, V is the voltage window, P_{in} is the power density of incident light, S is the effective area of energy conversion and t_c is the photo-charging time.

Although the fiber-shaped integrated device can be portable and flexible, the energy harvesting part and storage part are connected through the external circuit, which can bring high internal resistance and electric loss. Then three-electrode device configuration has been proposed and fabricated. In a three-electrode device configuration, a common electrode of the two devices are employed. Guo *et al.* fabricated an integrated device configuration by stacking DSSC on top of a LIB, in which the devices share a Ti electrode with TiO_2 nanotubes deposited on both sides, as shown in Figure 2.17.^[63] In this configuration, the electrons injected into TiO_2 can transport directly through the Ti foil to the LIB anode, instead of transporting through the external circuit. The LIB can be photo-charged to 2.996 V within 8 min. The $\eta_{storage}$ and $\eta_{overall}$ are calculated as 41 % and 0.82 %, respectively. To cater for the demands of future electronics, fiber-shaped power packs for its lightness and flexibility based on three-electrode configuration are also developed. Chen *et al.* designed a twisted wire with integrated energy conversion and storage (Figure 2.18 a and b).^[64] Ti wire is employed as a common platform. The $\eta_{storage}$ and $\eta_{overall}$ reaches 68.4 % and 1.5 %, respectively. In addition to Ti, other electrodes have also been utilized as the common platform, such as polyaniline coated stainless steel (PANI-SS). A $\eta_{overall}$ of 2.1 % has been reported in the fiber-shaped energy pack with common PANI-SS electrode (Figure 2.18 c and d). Even though the integration of DSSC and supercapacitors/batteries have

achieved great progresses, the liquid electrolyte in the DSSC requires both DSSC and supercapacitor to be sealed, which results in a complex fabrication process.

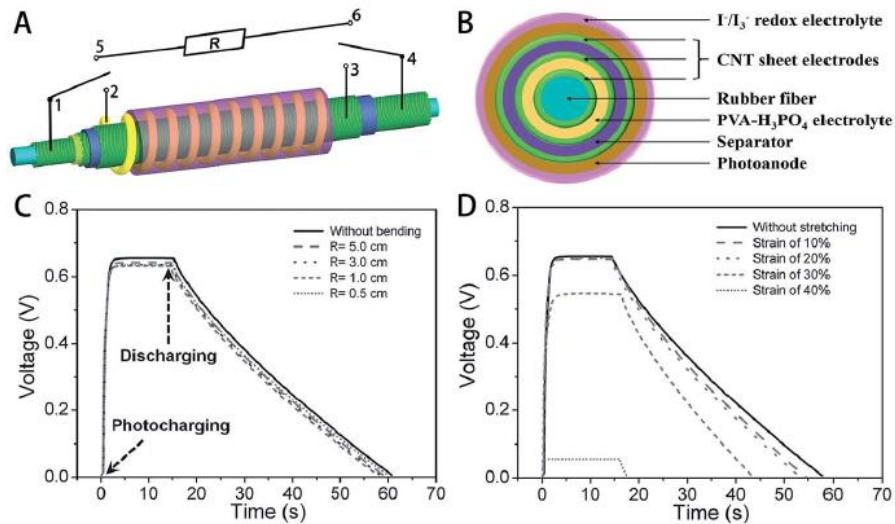


Figure 2.16. (a) Schematics of an integrated DSSC and CNT supercapacitor. (b) Cross-section of the fiber-shaped device. (c) Photo-charging and discharging curves. (d) The charging and discharging performances under stretching.^[62]

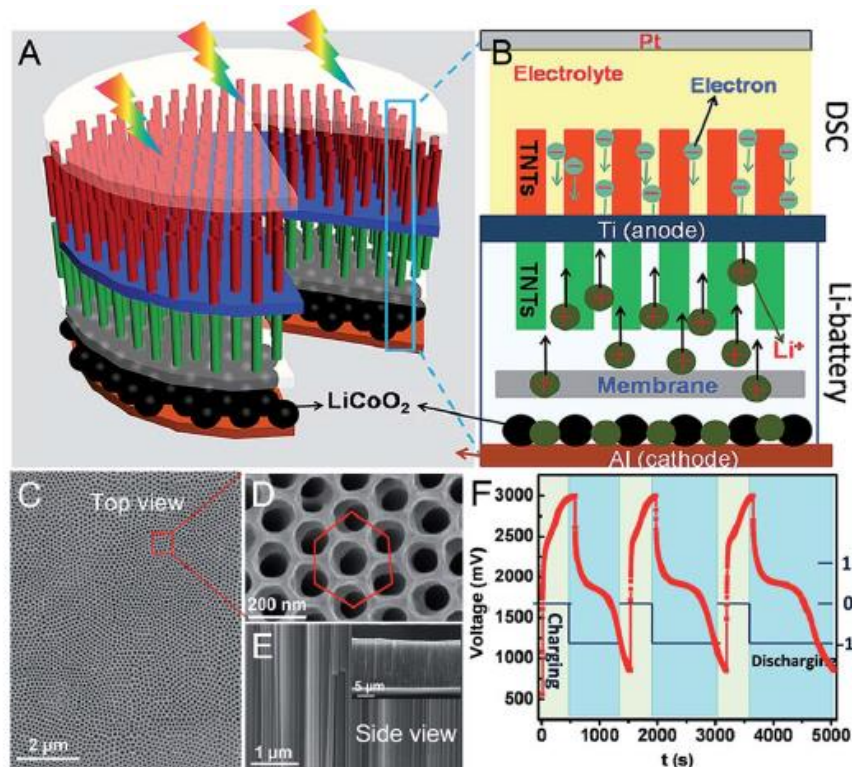


Figure 2.17 (a) A power pack including DSSC and LIB with Ti substrate as a common platform. (b) Schematics of illustrated working mechanism. (c)(d)(e) SEM images of TiO₂ nanotubes on the Ti foil. (f) Photo-charging and discharge curves.^[63]

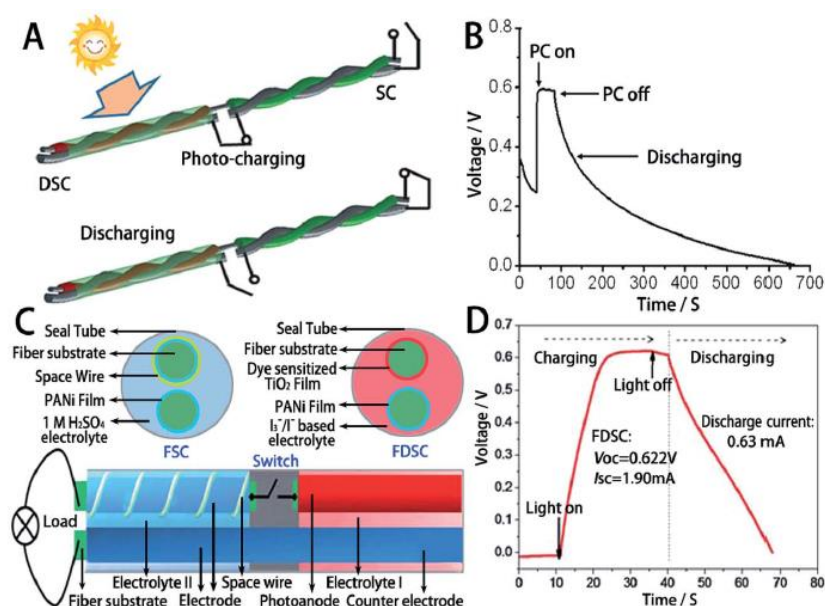


Figure 2.18. A fiber-shaped energy pack in three-electrode configuration by using Ti wire as a common platform. (a) Schematics of photo-charging and discharging. (b) Photo-charging and discharging curves. A fiber-shaped energy pack with PANI-ss as the common electrode. (c) Schematics and cross section image. (d) Photo-charging and discharging curves.^[64]

Thus, later with the development of polymer solar cells, the polymer solar cells have gradually replaced the DSSC in the energy pack. The polymer solar cells have the advantages of low cost, easy fabrication procedure and high power conversion efficiency.^[65, 66] The power conversion efficiency of polymer solar cells currently can reach 10 %. Currently, the high efficiency polymer solar cells are dominated by polymer-fullerene systems. Generally, polymer solar cell consists of an active layer (polymer donor and fullerene acceptor), an electron transport layer, a hole transport layer and two metal electrodes. The working principle is illustrated in Figure 2.19.^[67] As the light is illuminated and absorbed by the conjugated polymer, electron and hole pairs are generated in the active layer. The electrons transfer from the active layer to the electron transport layer and are then collected by the cathode. The holes generated transfer from the active layer to the hole transport layer and are collected by the anode.

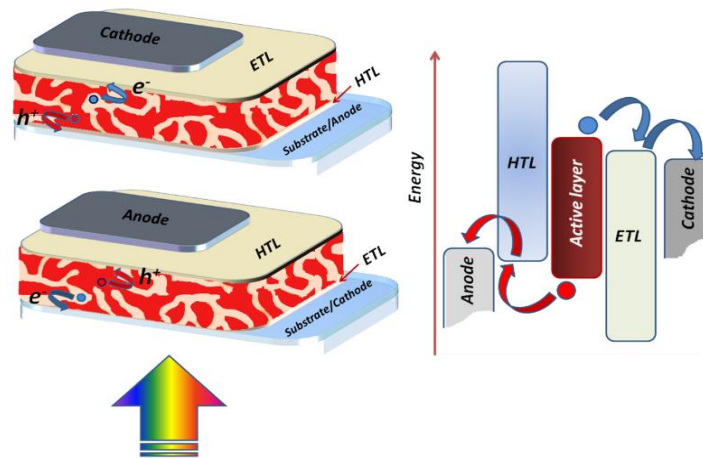


Figure 2.19. Schematics and working mechanisms of a typical polymer solar cell.^[67]

Polymer solar cells have great potentials in the applications of solar-powered supercapacitors. The polymer solar cell/supercapacitor packages have reported with light weight, good flexibility and high overall energy conversion and storage efficiency. Lu *et al.* reported a printable and solid state polymer solar cell/CNT supercapacitor, in which Al electrode serves as both current collector for supercapacitor and cathode for polymer solar cell (Figure 2.20).^[68] The device shows a light weight less than 1 g and the internal resistance is only 60% of the integrated devices that are connected through external circuit. Fiber-shaped power packs including polymer solar cell and supercapacitor are also fabricated to cater for the light, flexible and waveable electronics. Zhang *et al.* designed a fiber-shaped power package in a coaxial structure, as shown in Figure 2.21.^[69] The overall efficiency of the device is only 0.8 %, which is due to a low power conversion efficiency of the polymer solar cell.

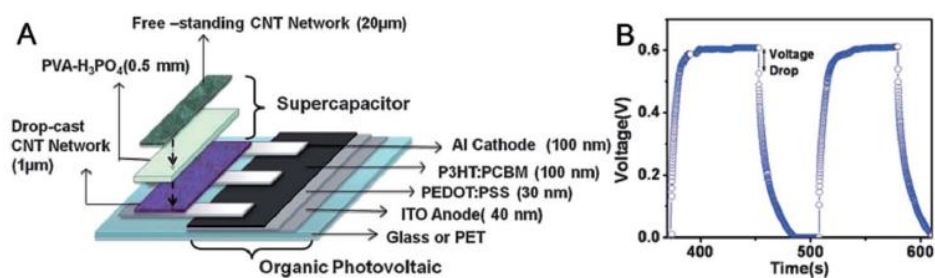


Figure 2.20. Polymer solar cell/CNT supercapacitor package. (a) Device structure. (b) Photo-charging and discharging curves.^[68]

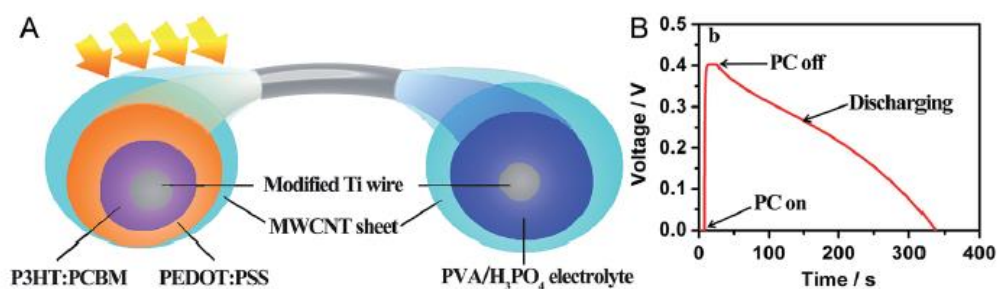


Figure 2.21 (a) A fiber-shaped energy pack. (b) Photo-charging and discharging curve.^[69]

The liquid electrolyte in the DSSC and relatively low power conversion efficiency in polymer solar cells limit the development of solar-powered energy storage devices application. In recent years, based on the DSSC structure, solid-state hybrid organic-inorganic perovskite solar cells (PSCs) have developed with excellent power conversion efficiency. Till now, a power conversion efficiency of 22.1 % has been achieved,^[70] which is comparable to a CIGS solar cell and is approaching the high efficiency of Si solar cells. A typical PSC generally consists of an organic-inorganic perovskite absorption layer, TiO₂ electron transport layer, Spiro-OMeTAD hole transport layer and two metal electrodes. The organometal halide perovskites (OHPs) adopts a general formula of MAPbX₃ (MA=CH₃NH₃, X=I, Br or Cl). It has shown excellent light absorption, long electron-hole diffusion length and tunable band gap, which determines a high power conversion efficiency of a PSC.^[71, 72]

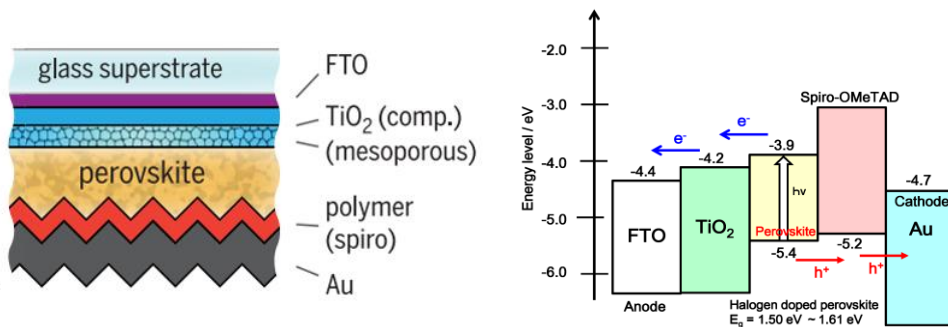


Figure 2.22. A typical perovskite device structure and band diagram.^[70]

PSCs are also promising candidates for the integrated energy package for the solid-state device, low cost and high power conversion efficiency. It can solve the issues of liquid electrolyte in DSSCs and relatively low power conversion efficiency in polymer solar cells. Currently, the investigations of PSC/supercapacitor energy packs are very limited and the study of integration so far is at the stage of connecting the two device through external circuit. A power pack based on PSC and polypyrrole-based supercapacitor was reported by Xu *et al.* The two devices are connected by the external wires. The power conversion efficiency of PSC can reach 13.6%. The polypyrrole based supercapacitor can be photo-charged to 0.7 V within 350 s. An overall efficiency of the 10 % can be delivered in this power pack, which is much higher than that reported before.^[73] This study further prove the potentials of perovskite solar cell in energy harvesting/storage power pack design.

2.1.3.2. Challenges and outlook

The selection of energy harvesting and energy storage devices are significant for the power pack with excellent performances. Low cost, integration level, high conversion efficiency, flexibility and portability are all important parameters for the energy harvesting/storage device integration. As the liquid electrolyte in DSSC and relatively

low power conversion efficiency in polymer solar cells, the integration of perovskite solar cells and supercapacitors/batteries are promising for the next-generation energy pack. However, currently the integration of perovskite solar cell and supercapacitors has not been extensively studied and the integration level is still relatively low, possibly due to the difficulties in the fabrications and common electrode selection of the integrated device with three-electrode configuration. To develop a perovskite solar cell powered supercapacitor with high integration level is highly desirable.

2.2 Multifunctional perovskite photovoltachromic supercapacitor

2.2.1. Motivation

Optically switchable materials have broad applications in the building architectures, vehicle windows, aircrafts, and sunroofs, because they not only reduce cooling/heating costs and ventilation loads, but also enhance the thermal and visual comfort for indoor users.^[74-79] Therefore, the smart windows with electrochromic (EC) have been put into applications in human life. In recent years, with the increasing attentions on energy issues, self-powered smart windows, such as photoelectrochromic (PECC) and photovoltachromic cells (PVCC) have been designed, where a solar cell and an electrochromic material or electrochromic cell are integrated. The optical transmittance change of the system can be stimulated and reversed in response to an external light stimuli. Figure 2.23a illustrates the schematics of PECC and PVCC. In the conventional PECC, Pt counter electrode in dye-sensitized solar cells (DSSC) is replaced by WO_3

electrode, where the color change can be driven by photovoltaic potential resulted from optical illumination. Compared with PECC, patterned WO_3/Pt electrochromic electrode are used in PVCC, which can be colored under short-circuit condition, and realize tunable transmittance states and fast responses.^[80-83] In these conventional PECC and PVCC devices, the electrochromic materials are typically employed as only one of the electrodes of the device, and their transmittances can fast response to the illumination and switch between the bleached and colored states (Figure 2.23c). In addition to the PVCC in which energy is harvested by the DSSC, recently a perovskite solar cell powered electrochromic cell have also been reported, in which perovskite solar cell is stacked on WO_3 based electrochromic cell (Figure 2.24). However, for all the investigations discussed above, the energy harvested from the solar cell in these kinds of devices is only used to trigger the change of optical transmittance, and the devices lack of the ability of storing the harvested solar energy because of the limited capacity of the counter electrode (*e.g.*, indium tin oxide) of the capacitor. Thus, the harvested solar energy is not fully used in these kinds of device configurations.

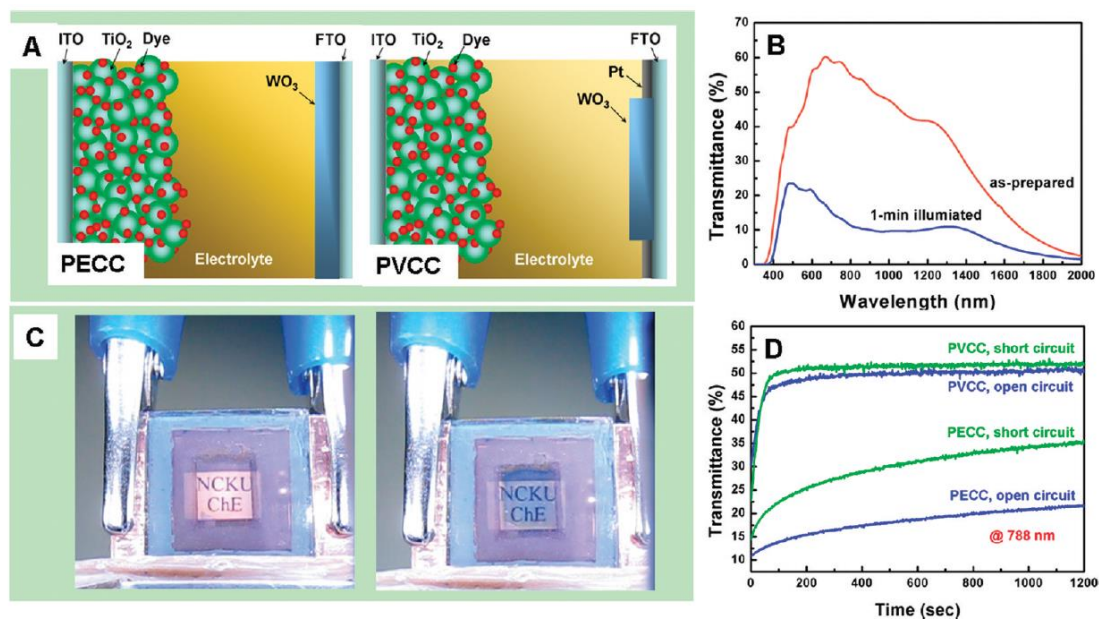


Figure 2.23. (a) Schematics of PECC and PVCC. (b) Transmittance spectra of PECC at as-prepared and colored states (open-circuit condition). (c) Photos of PECC and PVCC colored states. (d) The transmittance spectra illustrating the bleaching of PECC and PVCC at open circuit condition and short circuit condition at a wavelength of 788 nm.

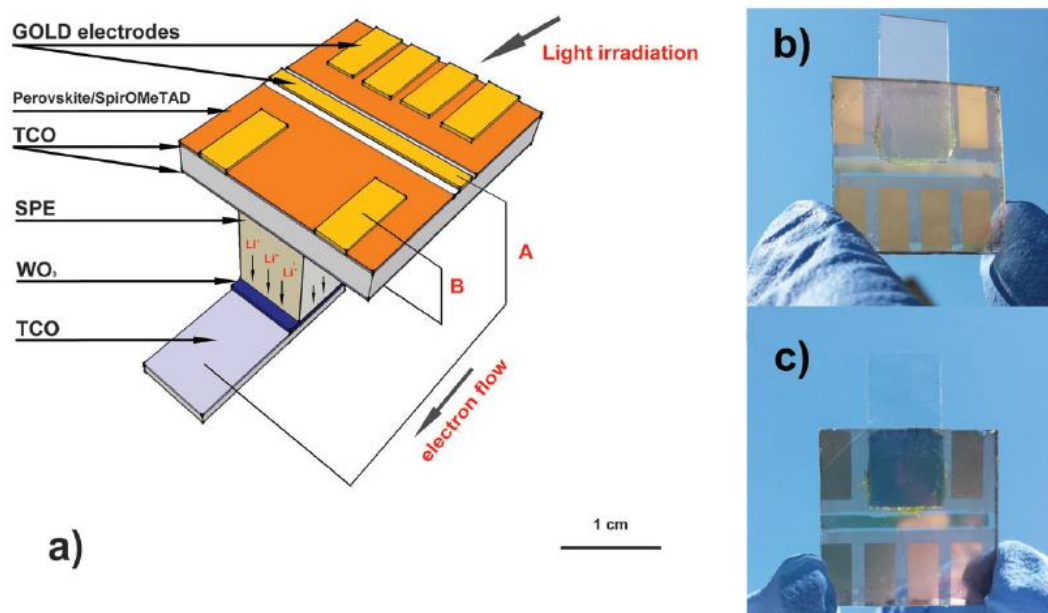


Figure 2.24 (a) Schematics of a PVCC device based on perovskite solar cell and WO₃ electrochromic cell. (b) and (c) Photos of PVCC at bleached state and colored state, respectively.

The light sources for photovoltaic devices are usually intermittent and unpredictable. The integration of photovoltaic and energy storage/electrochromic cell together makes it possible to provide sustainable power source and retain the PVCC in

a desired colored state. There have been a number of works integrating the photovoltaic cells and energy storage devices (supercapacitor or battery) together to realize a self-powered energy storage device.^[84-88] Xu *et al.* demonstrated the integration of perovskite solar cell (PSC) and lithium ion batteries, and reported a high total photoelectric and energy conversion efficiency (~7.8%) and excellent cycling stability.^[89] Wang's research group integrated organometallic PSC and polypyrrole-based supercapacitor, and realized a high output voltage of 1.45 V and high energy conversion efficiency of 10%.^[90] Integrated smart electrochromic windows for energy storage application have also been studied recently.^[91-94] However, these prototypes are connected by two separated energy conversion and storage devices through external wires or power management circuit. This configuration reduces the integration level, causes additional Ohmic loss, and lacks of dynamic solar light control.

Subsequently, researchers have made lots of efforts to combine energy conversion and storage functions into one device and improve the integration level. Wee and his co-workers demonstrated a stacked photo-supercapacitor, in which the organic photovoltaics (OPV) and carbon nanotube (CNT) supercapacitor share a common electrode, and the internal resistance of the device is reduced by 43% as well as the power loss.^[95] This kind of structure has also been studied for dye-sensitized solar cell (DSSC) integrated with the CNT supercapacitors.^[96-98] However, there is still quite few works that report the integration of electrochromic supercapacitor and semitransparent solar cell into one device, which possesses higher integration level, allows dynamic solar light control and enables a smarter device.

In this work, we integrate the semitransparent PSC and electrochromic WO_3 supercapacitor into a photovoltachromic supercapacitor (PVCS) in a vertically stacked configuration. Our structures improve the integration level, achieve widely and automatically tunable optical transmittance of the integrated device, and store the electrochemical energy accompanying with the color change. In addition, the electrochromic supercapacitor enhances the photo-stability of PSC by blocking part of the solar light during the fully charged state, which alleviates the photo-degradation issue of the PSC for outdoors application under long-term solar light exposure. This multifunctional PVCS device provides unprecedented advantages over conventional smart window design.

2.2.2. Experiments

Fabrication and Characterization of Perovskite Solar Cell. Figure 2.25 shows the process flow of PSC fabrication. The patterned fluorine-doped tin oxide (FTO) coated glass substrates were cleaned with acetone, isopropanol and deionized water sequentially. The pre-cleaned substrates were then dried with nitrogen gas and further cleaned by UV-Ozone treatment. A solution prepared by mixing 1.25 ml acetic acid and titanium (IV) isopropoxide (TTIP) solution (1.25 ml) in anhydrous ethanol (15 ml) was spin coated (3500 rpm, 30 s) onto the cleaned substrates to form a compact titanium dioxide (c-TiO₂) layer. The prepared c-TiO₂ layer was then baked at 450 °C for 2 hours in air. A one-step spin coating was applied to the deposition of perovskite layer ($\text{CH}_3\text{NH}_3\text{PbI}_{3-x}\text{Cl}_x$) in this work. The spin coating solution for the perovskite layer was

prepared by mixing 2.4 M methylammonium iodide and 0.8 M lead chloride in N, N-dimethylformamide (DMF). The spin-coated perovskite thin film was then dried at 65 °C for 15 min and annealed at 105 °C for 45 min until the color turned to dark brown. To prepare the 2,2',7,7'-tetrakis(N,N-di-p-methoxyphenylamine)-9,9-spirobifluorene (spiro-MeOTAD) solution, 29 µl of 4-tert-butyl pyridine and 18 µl of lithium bis(trifluoromethanesulfonyl)imide (Li-TFSI) solution (520 mg Li-TFSI in 1 ml acetonitrile, Sigma-Aldrich, 99.8%) was added into 953 µl of chlorobenzene dissolved with 80 mg spiro-MeOTAD powder. The solution was then spin coated on the perovskite layer at 4500 rpm for 30s. The prepared FTO/c-TiO₂/CH₃NH₃PbI_{3-x}Cl_x/spiro-MeDTAD films were annealed in oxygen to enhance the cell performance. Finally, MoO₃/Au/MoO₃ electrodes (15 nm/ 12 nm/ 20 nm) were evaporated onto the devices, through which the device active area was defined as 0.06 cm². The solar source was provided by the Newport solar simulator (ORIEL Sol3ATM) and the electrical measurement was performed by B1500A semiconductor analyzer. The absorption spectra of perovskite film on quartz were examined using a UV-2550 Shimadzu UV-Vis spectrophotometer. X-ray diffraction (XRD) patterns of the perovskite film was determined by a Rigaku SmartLab X-ray diffractometer with a 2θ range from 10° to 70° in a step of 0.01°. Scanning electron microscopy (SEM) image was performed by Hitachi S-4800 field emission scanning electron microscope.

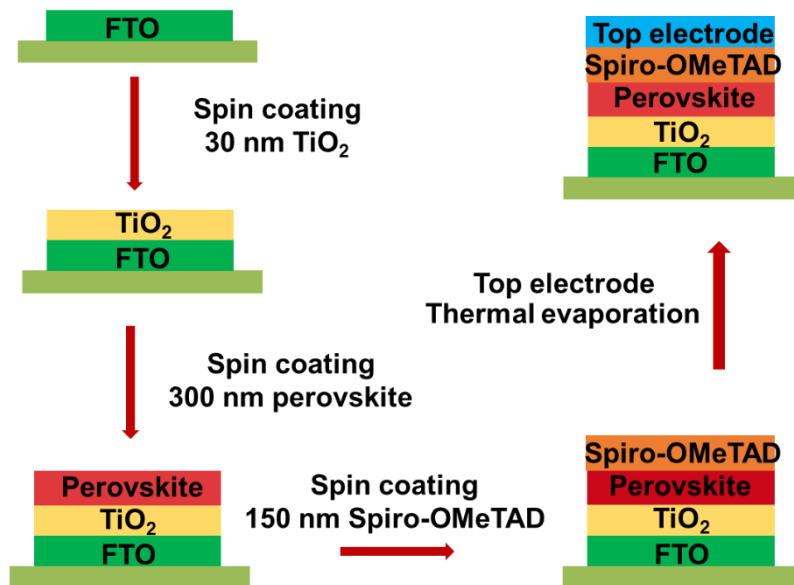


Figure 2.25. Fabrication process flow of the PSC.

Fabrication and Characterization of Electrochromic Supercapacitor. A 300 nm-thick WO₃ thin film was thermally evaporated onto an FTO substrate as supercapacitor electrode. The deposition was carried out with the background pressure of 5×10^{-6} Torr and the chamber pressure during the deposition was maintained at 3×10^{-5} Torr. The symmetric electrochromic supercapacitor was assembled by two identical WO₃ electrodes coated with the mixture of polyvinyl alcohol (PVA) and 1M H₂SO₄. Atomic force microscopy (AFM) image was examined by Bruker nanoscope 8. The electrochemical performances were characterized by electrochemical working station (CHI 660e, Shanghai Chenhua).

Integrated Device Characterization. The photo-charging process was performed under AM 1.5 illumination and the supercapacitor was discharged through electrochemical workstation. The transmittance spectra were obtained by using the UV-2550 Shimadzu UV-Vis spectrophotometer.

2.2.3. Results and discussions

Integration of Co-anode and Co-cathode PVCSs. Figure 2.26a and Figure 2.26b show the absorption spectra and SEM image of the perovskite thin film. Figure 2.27a shows the schematic diagram and photo of a PSC with a MoO₃/Au/MoO₃ (MAM) transparent electrode, which is used for our integrated PVCS structures. The structure of the other PSC part is similar to our previous works.^[99] Here we replace top electrode with a stacked transparent structure, MoO₃ (adjacent to spirOMeTAD)/Au/MoO₃ (15 nm/12 nm/20 nm), which has been also employed as transparent electrodes in organic photovoltaic cells (OPV) and light emitting diodes (LED).^[100-102] The transparent MAM structure shows a transmission of 77.1% at the wavelength of 600 nm and the average visible transmission (AVT) of 70.6% within the wavelength range of 380~780 nm (Figure 2.27b). The whole PSC device with the MAM top electrode has a higher transmission (>40%) at a longer wavelength above 650 nm (Figure 2.27c). We demonstrate a typical PSC with the transparent MAM top electrodes, showing good power conversion efficiencies (PCE) of 12.54 % and 9.35 % with the light illuminated from both FTO side and MAM side, respectively, as shown in Figure 1d. This all-transparent-electrode PSC provides photo voltage for the electrochromic part, and allows solar light to be illuminated from both sides. We also fabricated a typical PSC device with Au top electrode for comparison, which exhibits a high efficiency of 16.4%, as shown in the Figure 2.26c.

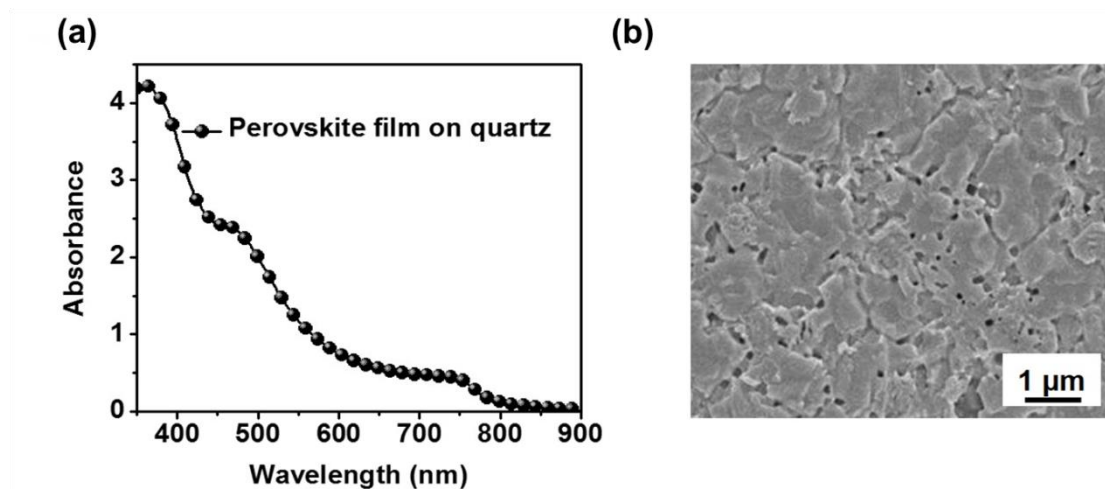


Figure 2.26. (a) Absorption spectra of perovskite film on quartz. (b) SEM image of perovskite film.

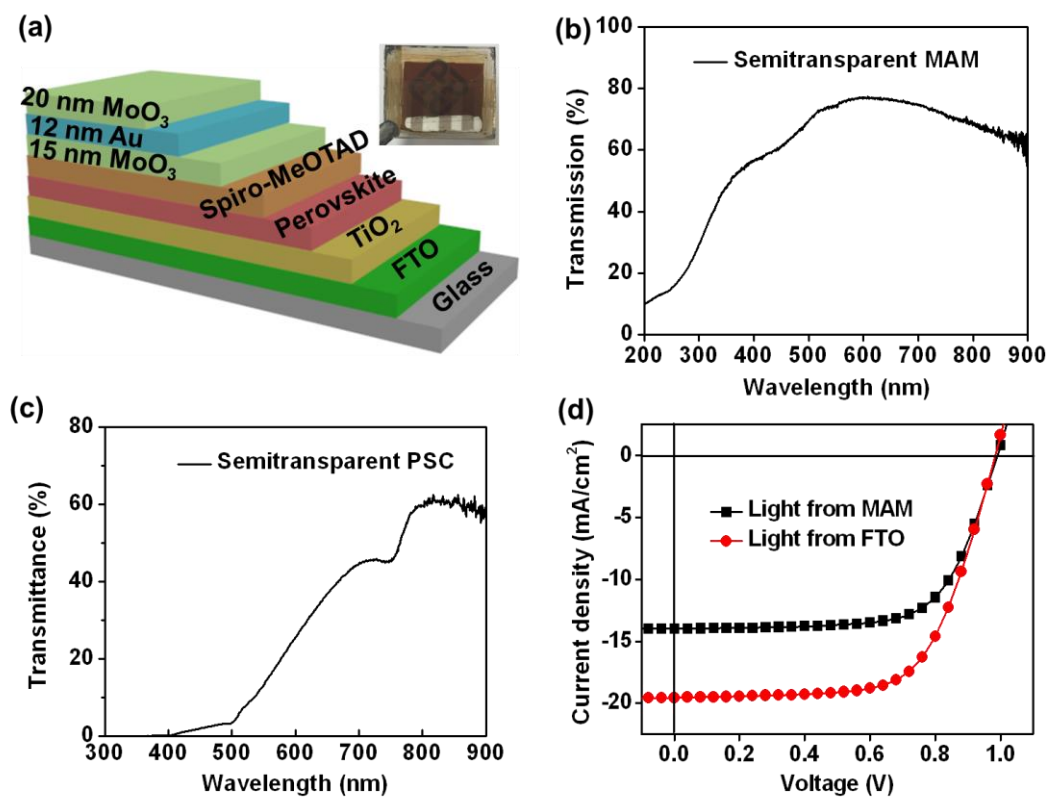


Figure 2.27. (a) Schematic diagram and photo of PSC with MAM transparent electrode. (b) UV-Vis spectra of the as-fabricated MAM, showing an AVT of 70.6 %. (c) UV-Vis spectra of the whole PSC device with the MAM top electrode. (d) J - V curves of a typically semitransparent PSC (MAM electrode) with the light illuminated from both FTO side and MAM side, exhibiting PCEs of 12.54% and 9.35%, respectively.

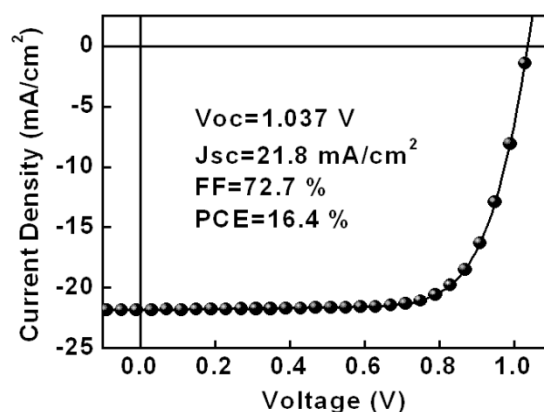


Figure 2.28. A J - V curve of a typical PSC device with Au top electrode, showing a PCE of 16.4 %.

Both electrochromism and energy storage of WO_3 electrode involve the electrochemical reaction at the interface between electrode and electrolyte, where the valence states of electrochromic WO_3 electrode are changed and lead to energy storage in the meantime. [103-106] The integration of WO_3 based electrochromic device together with PSC enables a new type of PVCC structures. [80] Figure 2.29 shows characterization results of the WO_3 thin films by thermal evaporation. Figure 2.29a shows the schematic diagram of a symmetric WO_3 electrochromic supercapacitor (ECS). A 200-nm-thick WO_3 thin film was deposited onto a fluorine-doped tin oxide (FTO) substrate as supercapacitor electrode. Polyvinyl alcohol (PVA) doped with 1 M H_2SO_4 was used as the electrolyte. The symmetric ECS was assembled by two identical WO_3 electrodes coated with PVA. Figure 2.29b and c are representative atomic force microscopy (AFM) image and scanning electron microscopy (SEM) image of the as-deposited WO_3 thin film, respectively. The nearly spherical grains are observed with a grain size of 50-200 nm and a roughness of 22.9 nm. Lots of voids are presented between the grains, providing large surface area and effective paths for ion storage and redox reaction. Figure 2.29d and S3e show the X-ray photoelectron microscopy (XPS) spectra of the

WO₃ thin film. Four peaks are separated from the W 4f peak, corresponding to W⁶⁺ and W⁵⁺ oxidation states, respectively. The strong W⁶⁺ peaks suggest W⁶⁺ oxidation state is the dominating state in the as-prepared WO₃ thin film, which is in agreement with the transparent state. We further integrate all-transparent-electrode PSC with electrochromic supercapacitor (ECS) in a vertically stacked configuration to form a PVCS, which possesses both wide range for tunable transmittance and seamless integration of energy conversion and storage.

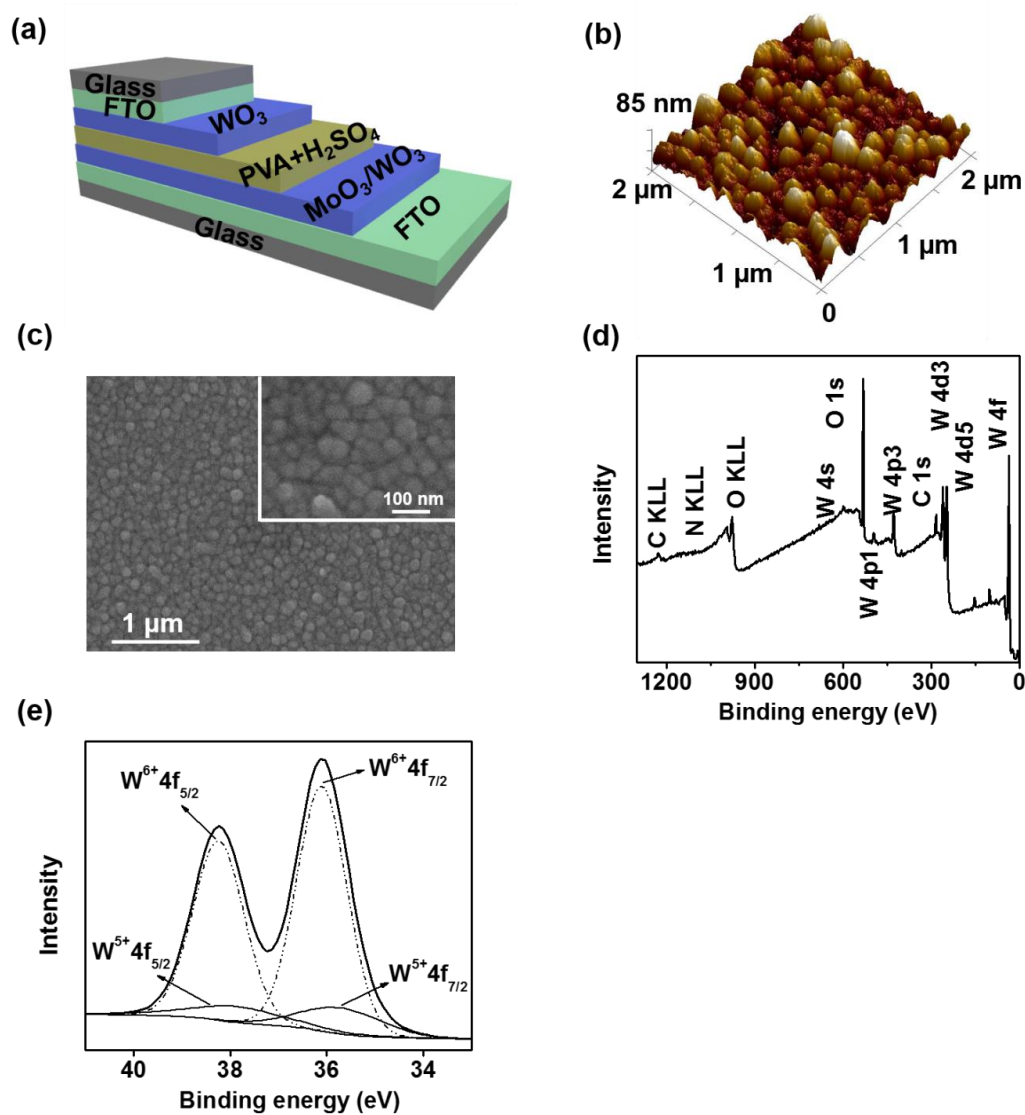


Figure 2.29. (a) Schematic diagram of a symmetric WO₃ ECS. (b) AFM and (c) SEM image of the as-deposited WO₃ thin film. (d) and (e) XPS spectra of the WO₃ thin film.

Figure 2.30 a and c show the schematic diagrams of the two stacked PVCS structures, namely co-anode structure and co-cathode structure. In the co-anode structure (Figure 2a), a transparent ECS device is integrated and shares an electrode with the semitransparent PSC. Figure 2.30 b shows the cross-sectional image of the co-anode structure. The light is illuminated from the top side and transmitted through the ECS cathode to PSC. We fabricated both PSC part and ECS anode on one common glass. The transparent MAM electrode (15 nm/12 nm/20 nm) serves as a co-anode for both PSC and ECS. We then deposited another 200 nm MoO₃ thin film in the ECS part as the ECS anode to obtain a better capacity. The top WO₃ electrode of the ECS was assembled with the PSC and the ECS anode through the gel-like PVA/H₂SO₄ electrolyte, and works as both the “electrochromic shelter” of the PSC and the cathode of the ECS. This type of PVCS structure avoids of the use of electrical wires during the photo-charging compared with the PVCC designed in Ref. 7. For the co-cathode structure (Figure 2d), a symmetric WO₃ ECS is stacked on the PSC. The PSC and ECS share a glass with both sides coated with FTO, where both sides are electrically connected. The FTO serves as the cathodes for both PSC and ECS. The WO₃ thin film was first deposited on one side of FTO, and the PSC part was fabricated on the other side of the FTO. The WO₃ anode on single-side FTO was then assembled with the above parts through the PVA/H₂SO₄ electrolyte.

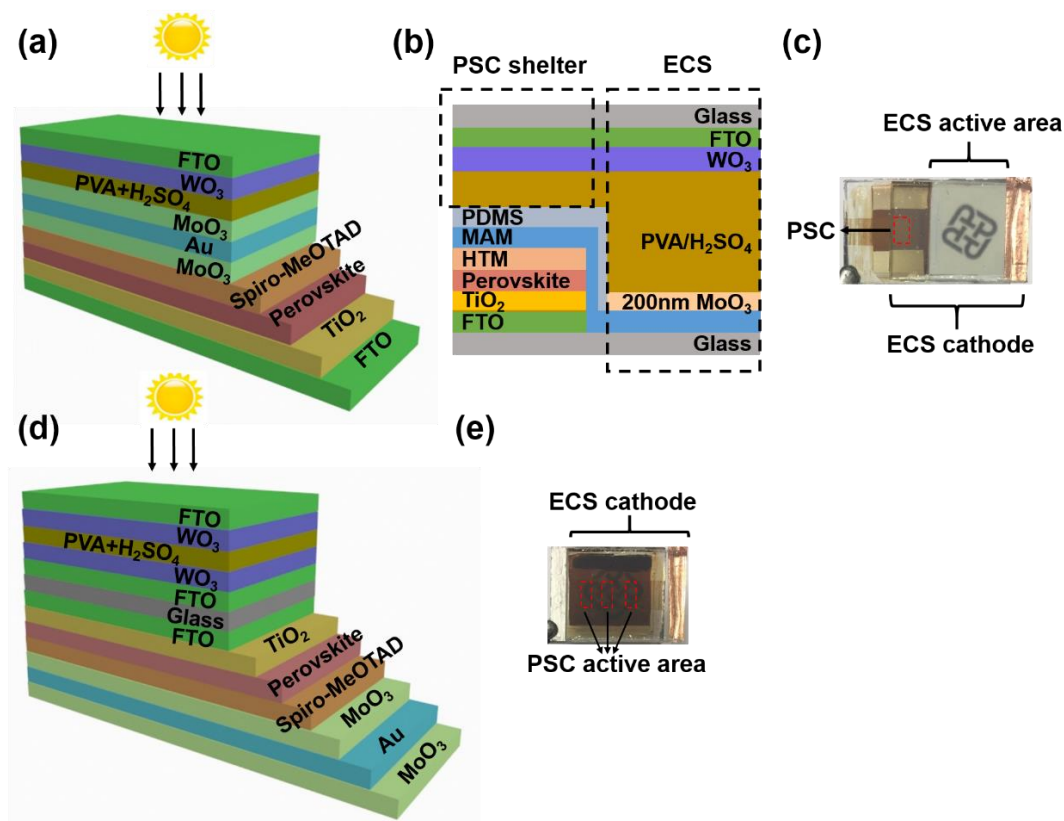


Figure 2.30. (a), (b) and (c) three-dimensional schematic, cross-section and photo of co-anode PVCS. (d) and (e) three-dimensional schematic and photo of co-cathode PVCS. The red dashed boxes represent the active area of PSCs.

Tunable Optical Transmittance of PVCSs. For the integrated co-anode and co-cathode PVCSs, the solar light can illuminate from the side of ECS, and transmit through the ECS device to the PSC. Figure 2.31 a-c and d-f schematically show the working mechanisms of the co-anode and co-cathode devices, where the initially charged state, fully charged state and bleached state are illustrated, respectively. For both co-anode and co-cathode PVCSs, the devices were photo-charged under AM 1.5 illumination in the short-circuit condition by connecting terminal A and C. Discharging process was conducted through the external circuit by connecting terminal A and B of the two ECS electrodes, where the discharged current density was controlled as 0.1 mA/cm^2 . For the co-anode device, during the photo-charging process, the electrons and holes are generated in the perovskite layer, and are transported to the electron

conducting layer TiO₂ and the hole transport layer Spiro-OMeTAD, respectively. The semitransparent MAM electrode collects holes, which serves as the anode of both ECS and PSC at terminal B. For the co-cathode device, the two FTO cathodes of the PSC and ECS are kept connected at terminal B during the whole charging process and collect the photo-generated electrons. The photovoltaic potential drives the re-distribution of ions in the electrolytes, and the electricity is stored at the WO₃ electrode of the ECS in the form electrochemical energy. Then the charged PVCSs can be discharged through the external circuit by connecting terminal A and B. During the photo-charging process of the two integrated PVCSs, electrons are injected into the WO₃ cathode and H⁺ moves towards the ECS anode driven by the electric-field ($\text{WO}_3 + \text{H}^+ + \text{e} \rightarrow \text{HWO}_3$). Charges are stored at the WO₃ cathode during the oxidation reaction, and the color changes from transparent to blue, which is accompanied with the chemical state of W changing from 6+ (bleached state) to 5+ (colored state).^[107-108] The other ECS anode works as a charge balancing counter electrode. During the discharging stage, the reversible reduction process releases the charge ($\text{HWO}_3 \rightarrow \text{WO}_3 + \text{H}^+ + \text{e}$), and the WO₃ thin film recovers to be transparent, which allows a new working cycle of the integrated device.

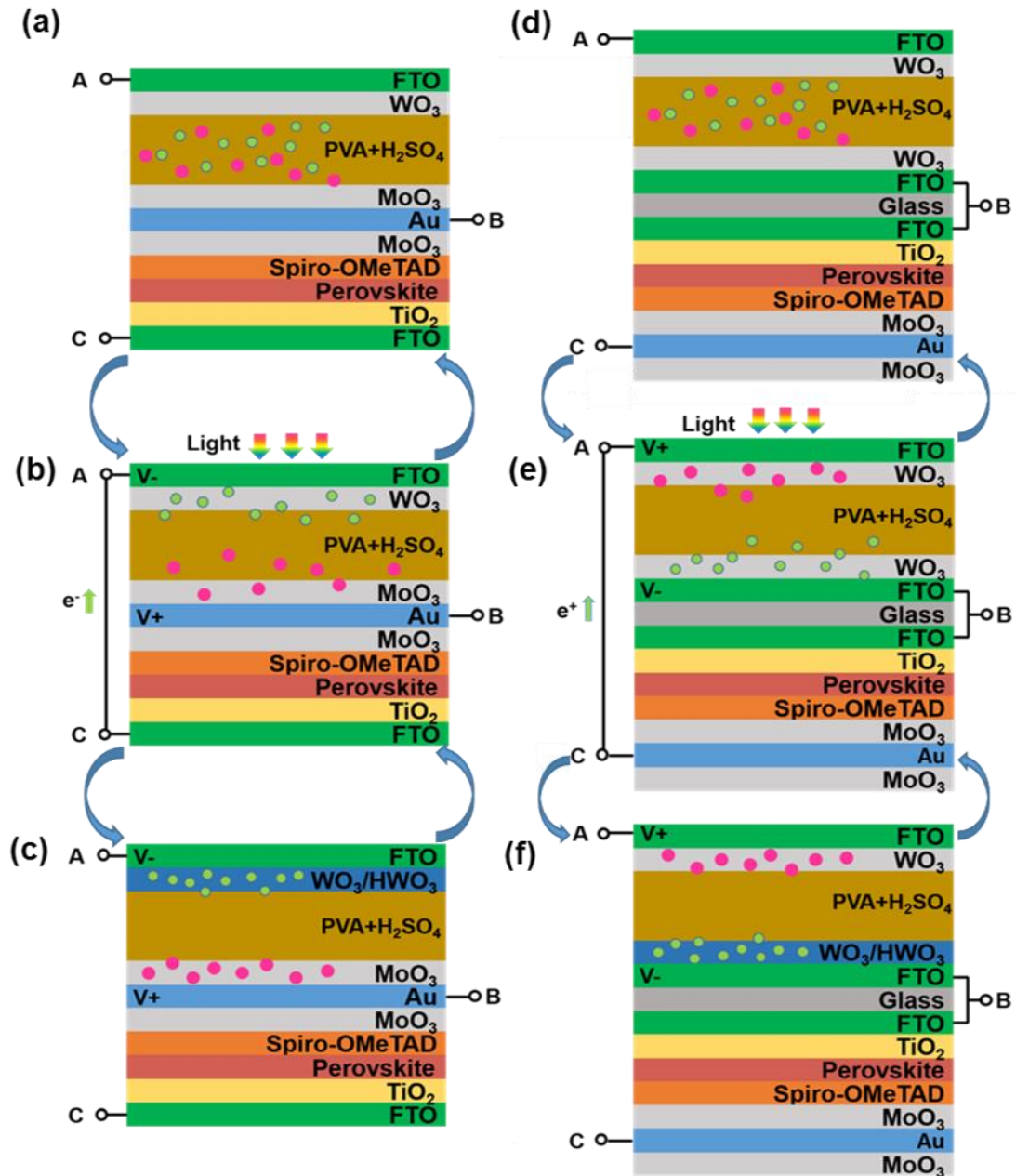
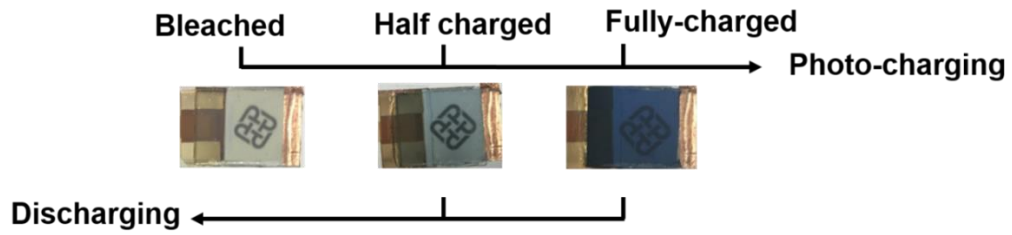


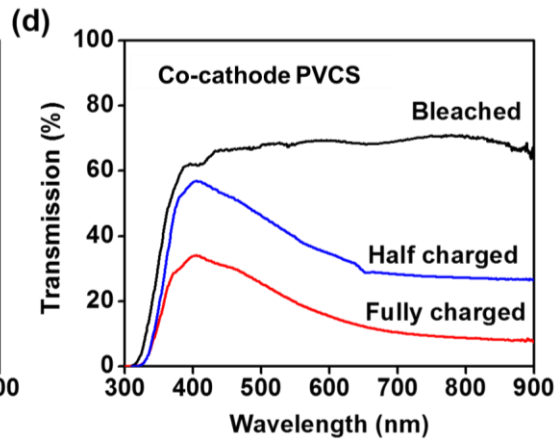
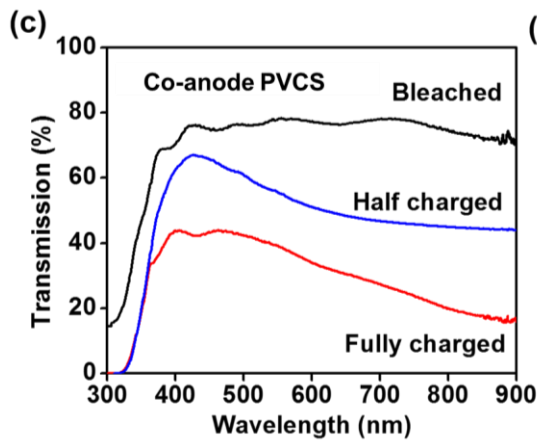
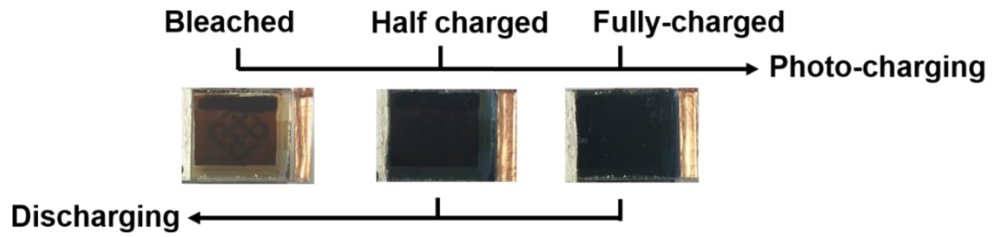
Figure 2.31. Schematics of co-anode and co-cathode PVCS working mechanism. Original states of (a) co-anode and (d) co-cathode PVCS. At the original states, ECS parts are transparent and at a bleached states, which allow solar light to pass through. Initial charged states of (b) co-anode and (e) co-cathode PVCS: under the solar illumination, electric-fields are formed in the PSC parts which power the ECS. Electrons are injected into the WO_3 cathode, and H^+ moves towards to the WO_3 cathode driven by electric-field. Charges are stored at the WO_3 cathode during the reversible oxidation reaction. The colors are starting to change. (c) and (f) Fully charged states: with the continuous light illumination, the PVCSs reach their fully charged states. The ECS color turns to blue, accompanying with the chemical state of W charging from $6+$ (bleaching state) to $5+$ (coloring state). These whole processes are reversible. After the discharging through external circuit, the reversible reduction process releases the charge and the WO_3 thin film recovers to be transparent, thus the PVCSs recover to their bleached states.

Tunable color states can be achieved in our PVCS devices. Figure 2.32 a and b show the photos of the co-cathode and co-anode PVCSs under bleached, half charged and fully charged states. The color of the ECS parts turn to deep blue during the photo-charging and recovers to transparent after discharging. We define a ‘PSC shelter’ here to describe the PVCS working states. The light transmits from the PSC shelter to the PSC. In the co-anode device, the PSC shelter is FTO/WO₃/PVA electrolyte; and in the co-cathode device, the PSC shelter is FTO/WO₃/PVA electrolyte/WO₃/FTO/glass. Figure 2.32 c and d demonstrate the transmission spectra of PSC shelters in the two integrated PVCSs corresponding to different colored states. The transmission peaks in blue-purple region are exhibited in the colored PSC shelters, and the other wavelengths in the visible light region are largely reduced. The AVT of co-anode (co-cathode) PVCS is significantly reduced from 76.2% (68.7%) to 54.2% (38.2%) to 35.1% (23.0%) corresponding to the bleached, half charged and fully charged states of the PSC shelters in the PVCSs. Figure 2.32e demonstrates the color coordinates of the “PSC shelters” with transmission spectra of Figure 2.32 c and d under AM 1.5 illumination plotted on the CIE xy 1931 chromaticity diagram. The color coordinates of both bleached PSC shelters lie in the central region in the chromaticity diagram, close to the AM 1.5 illumination. As the PVCSs are kept charging, the PSC shelters are colored, and there is a shift from central to blue region. However, the coordinate of the colored PSC shelters still locate close to the central region of CIE diagram, demonstrating good color neutrality. This neutrality renders this PVCS with great potential in the building application.

(a) Co-anode PVCS



(b) Co-cathode PVCS



(e)

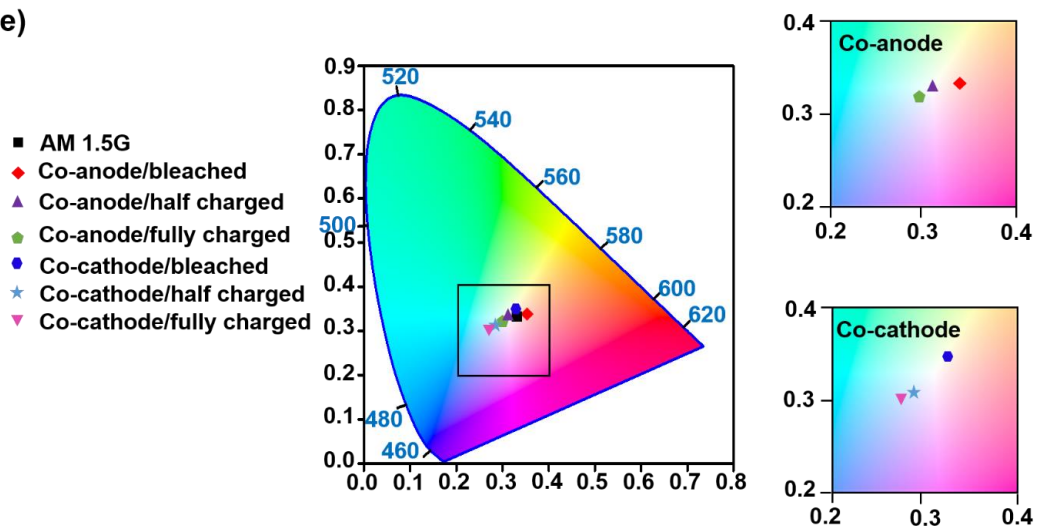


Figure 2.32. The photos of (a) Co-anode and (b) co-cathode PVCS color states under bleached, half charged and fully charged. Transmission spectra of PSC shelters in (c) co-anode PVCS and (d) co-

cathode PVCS corresponding to different color states. Accompanying with energy storage, the color of PSC shelters changes from transparent to blue with a reduction in AVT from 76.2 % (68.7%) to 35.1 (23.0%) for co-anode PVCS and co-cathode PVCS, respectively. (e) Color coordinates of the PSC shelters with transmission spectra of 3(c) and (d) under AM 1.5 illumination plotted on the CIE xy 1931 chromaticity diagram.

In-situ Energy Storage of PVCSs. The tunable color state of the PVCS is also an indicator of the amount of energy stored in the cell, which allows us to estimate the stored energy in PVCS by differentiating its colored state. Figure 2.33a and b show the voltages of the two PVCSs as a function of time evolution during the photo-charging and discharging process, and the color states corresponding to the charging and discharging processes. The discharging process was conducted at a constant current density of 0.1 mA/cm² by disconnecting terminals A and C (shown in the Figure 2.31) and no additional solar input will charge the supercapacitor during the discharging process. The co-anode PVCS was charged to 0.61 V within 60 s, and the co-cathode PVCS was charged to 0.68 V within 85 s. For the color change response, the co-anode (co-cathode) PVCS starts to change its color at a voltage of 0.55 (0.50) V, corresponding to a charging time of 10 s (13 s), and reach a saturated color state until the charging continues for 40 s (56 s). The energy density, average power density and specific areal capacitance of PVCS through photo-charging are calculated as 13.4 (24.5) mWh/m², 187.6 (377.0) mW/m² and 286.8 (430.7) F/m², respectively, as documented in Table 2.1. Figure 2.36a shows the areal capacitances at different current densities. The areal capacitance of the device reaches 119.5 F/cm² at a current density of 0.12 mA/cm². Figure 2.36b is the Ragone plot of the WO₃ ECS, which demonstrates an average power density of 6.8 W/m² at a charging current density of 1.20 mA/cm², and an energy density of 14.8 Wh/m² at a charging current density of 0.12 mA/cm². We calculated the specific capacitance and energy density according to the discharging

processes. According to the discharge curves, the total energy density of device can be calculated as:

$$E_{total} = \int U dQ = \int UI dt_{dis} = I \int U dt_{dis} = IS$$

Where I is the discharge current density, U is the charged voltage, t_{dis} is the total discharge time and S is the enclosed area of the discharge curve and coordinate axis.

The average power density can be expressed as:

$$P_t = \frac{E_{total}}{t_{dis}}$$

Based on the calculated energy density, the supercapacitor areal capacitance can be calculated as:

$$E_{total} = \frac{1}{2} CU^2$$

$$C = 2 \frac{E_{total}}{U^2}$$

The energy density of our PVCS is much larger than other types of self-powered energy storage systems, such as pizeo-supercapacitor and triboelectric nanogenerator.^[109-110]

The specific areal capacitances of our PVCSs are much larger than those of the graphene-based photo-supercapacitor,^[90-91] the integrated energy fiber based on CNT fiber and Ti wire,^[85] and other energy fiber integrating DSSC and electrochemical supercapacitor based on TiO₂ nanotube-modified Ti wire.^[92] This is also higher than self-powered smart electrochromic window based on WO₃ supercapacitor.^[91]

We also integrate the discrete energy harvesting and storage devices through external wires. Figure 2.35 shows the integration of a PSC with MAM anode and a symmetric WO₃ ECS connected by external wires. The supercapacitor was fully charged to 0.80 V within a 60-70 s light illumination and the discharging process lasted for 400 s at a current density of 0.1 mA/cm². The energy density, average power density and areal capacitance of the integrated device are 35.9 mWh/m², 461.5 mW/m² and 459.6 F/m²,

respectively. The performance is comparable with the device integrating commercial Si solar cell and ECS (Figure 2.36). However, this configuration with separated PSC and ECS not only reduces the integration level, but also fails to dynamically control the light transmission through the PVCS.

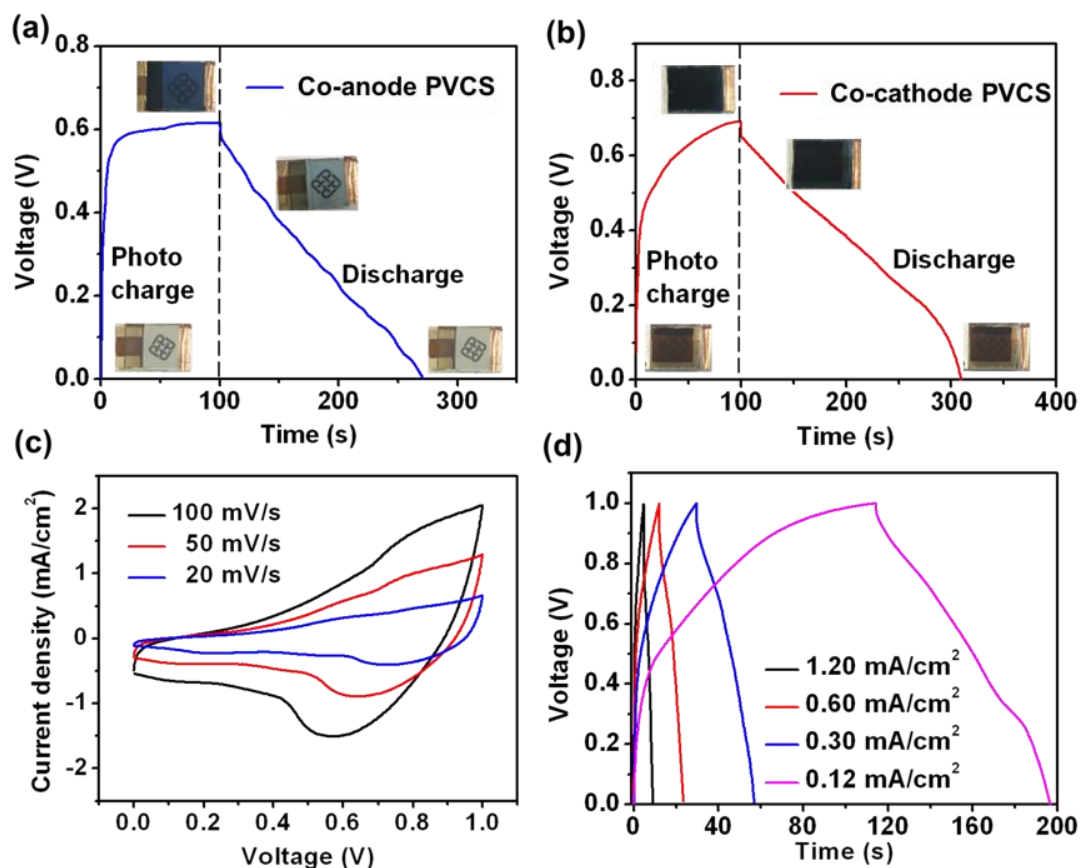


Figure 2.33. (a) and (b) The V-t curves of the co-anode PVCS and co-cathode devices for the photo-charging process within 100 s and discharging process at a current density of 0.1 mA/cm². (c) and (d) CV curves and GCD curves of a symmetric WO₃ ECS.

Table 2.1. Lists of internal resistance, energy density, average power density and areal capacitance of two types of PVCSs. The calculations are according to the discharge curve.

Device Type	Internal resistance (Ω)	Energy density (mWh/m ²)	Power density (mW/m ²)	Areal capacitance (F/m ²)
Co-anode	215	13.4	187.6	286.8
Co-cathode	275	24.5	377.0	430.7

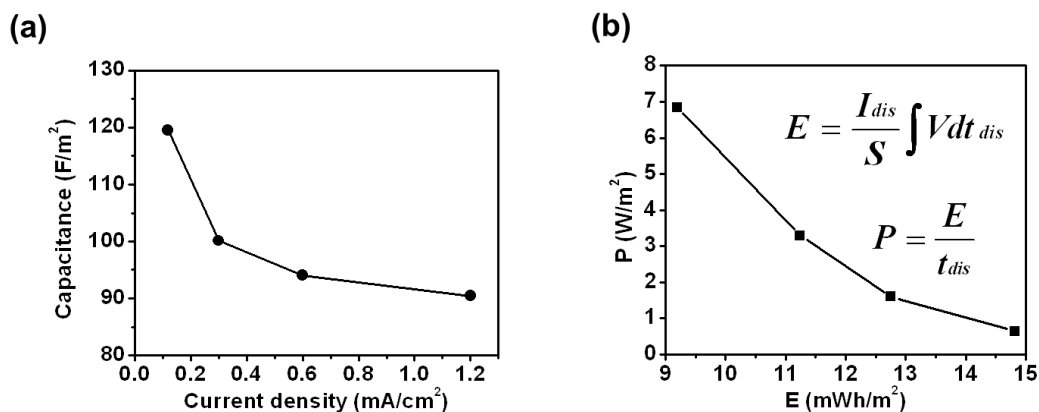


Figure 2.34. (a) The areal capacitances as a function of different current densities. (d) The Ragone plot of WO₃ ECS, showing the relationship between power density and energy density.

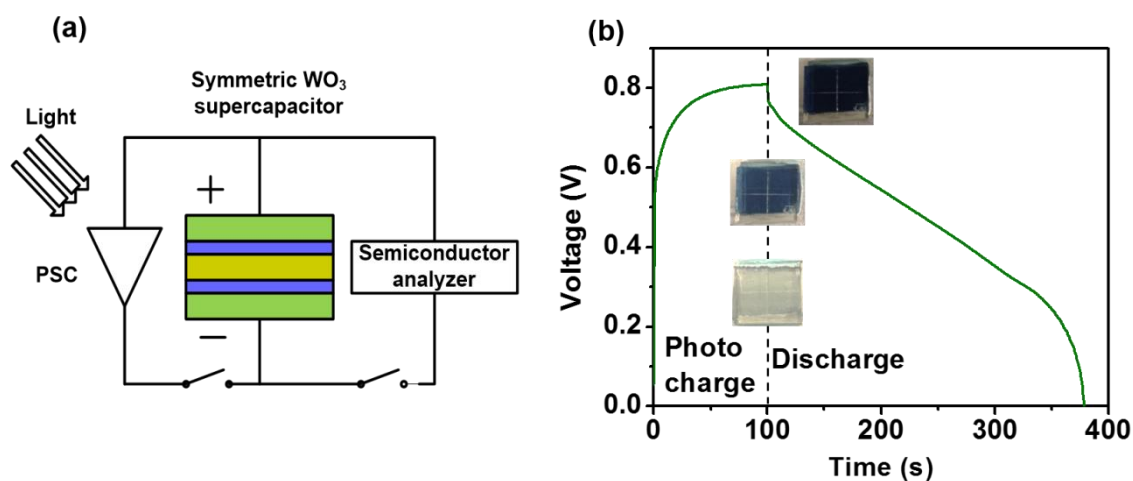


Figure 2.35. (a) Schematic illustration of the integration of the PSC with MAM anode and symmetric WO₃ ECS connected by external wires. (b) V-t curves of photo-charging and discharging processes and the color changes during the processes.

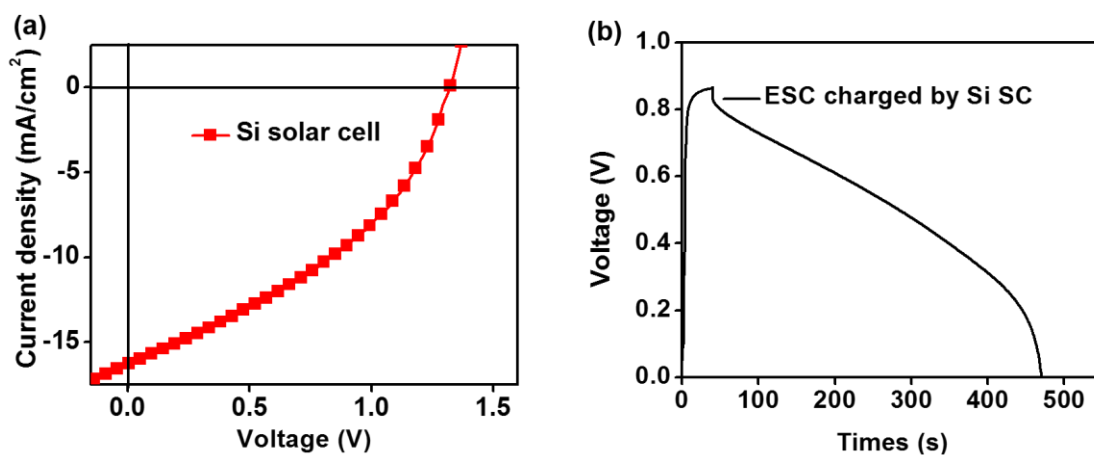


Figure 2.36. (a) A J-V curve of a commercial Si solar cell. (b) Photo-charging and discharging V-t curves of symmetric WO₃ ECS integrated with the commercial Si solar cell.

In other types of integrated solar-powered electrochromic windows reported in Ref. 80 and 93, the researchers usually employed the structure of TCO/WO₃/electrolyte/TCO in the ECS part. The TCO counter electrodes have very limited charge storage capability, and cannot provide sufficient balancing charge during the discharging process of the ECS. After the PVCC is converted to the colored state by a positive voltage (V), a reverse bias (-V) is required for converting the PVCC from the colored to the bleaching state. From the typical CV curve of the WO₃/electrolyte/TCO, there is no current response under a voltage scanning from V to 0, unless a reverse bias -V is applied. [80, 93] In contrast, our integrated PVCS devices enable an automatically working cycle of the color change during the charging/discharging process by replacing commonly used TCO anode with MoO₃/WO₃ as a charge balancing counter electrode. An extra reverse bias is not required for converting back to the bleached state, because the MoO₃/WO₃ counter electrode in our PVCS can provide more balancing charge than the ITO electrode in conventional PVCC. Our PVCSs can be bleached by discharging the ECS through external load. After the stored electrochemical energy is consumed, the ECS recovers to be transparent, and a new working cycle can be initiated. This feature can be also confirmed from our cyclic voltammetry (CV) curve and galvanostatic charging/discharging (GCD) curve. [111] Figure 2.29 c and d show the CV and GCD curves of a symmetric WO₃ ECS. Within a voltage scanning range 0-V, a cycle of forward and reverse voltage scanning can realize a color change from bleached state to

colored state, and back to the original bleached state. These characteristics provide an automatically working PVCS device for both energy storage and tunable colored states.

The considerably reduced charging current density can be responsible for a higher energy accumulated. The energy density (24.5 mWh/m²) and areal capacitance (430.7 F/m²) of the ECS charged to 0.68 V by PSC in our co-cathode PVCS configuration are higher than those of discretely symmetric WO₃ ECS (14.8 mWh/m² and 119.9 F/m²) through electrochemical working station, which is charged with a small current density of 0.12 mA/cm² to a higher voltage of 1 V (shown in Figure 2.34). These characteristics can be attributed to the charging way by photovoltaic device. As the light on, the PSC generates the photocurrent within a few seconds, which is considered as the initial charging current (0.4 mA/cm²) and leads to a fast charging rate. As the supercapacitor is kept charging and colored, the current density supplied by the PSC is significantly reduced. Additionally, as the supercapacitor reaches its fully charged state, the charging current is reduced continuously until the supercapacitor reached saturation.^[97-98] After the supercapacitor is charged to 0.45-0.5 V, there is a significant drop in the charging rate, which suggests a continuously reduced charged current density, thus leading to higher capacitance and energy density accumulated.

Photo-Stability Enhancement of Perovskite Solar Cells. Figure 2.37 a and b show the *J-V* curves of the two PSCs utilized in the co-anode and co-cathode PVCSs under different states. We first characterize the performance of the PSCs utilized in the two integrated co-anode and co-cathode PVCSs, respectively. The PSC (PDMS/MAM/spirOMeTAD/perovskite/TiO₂/FTO/Glass) for the co-anode PVCS with the light illumination from the MAM side demonstrates the V_{oc} of 0.983 V, J_{sc} of

12.46 mA/cm², fill factor (FF) of 65.4%, and PCE of 8.25%; the PSC (Glass/FTO/TiO₂/perovskite/ spirOMeTAD/MAM) for the co-cathode PVCS with the light illumination from the FTO side exhibits the V_{oc} of 1.000 V, J_{sc} of 18.17 mA/cm², FF of 65.4% and PCE of 11.89%, as shown in the Table 2.2. After the integration with the transparent ECS, both J_{sc} and PCE of the two PVCSs decrease to about 68% of single PSCs because the ECS has a certain level of light absorption. With the color change of the ECS by photo-charging, J_{sc} are further reduced by about half. The PCE of the co-anode and co-cathode PVCSs drops to 3.73% and 2.26%, respectively. This suggests the PSCs in the PVCSs supply the ECS part in a small current density and are at a low-power working state under the colored state of PVCSs.

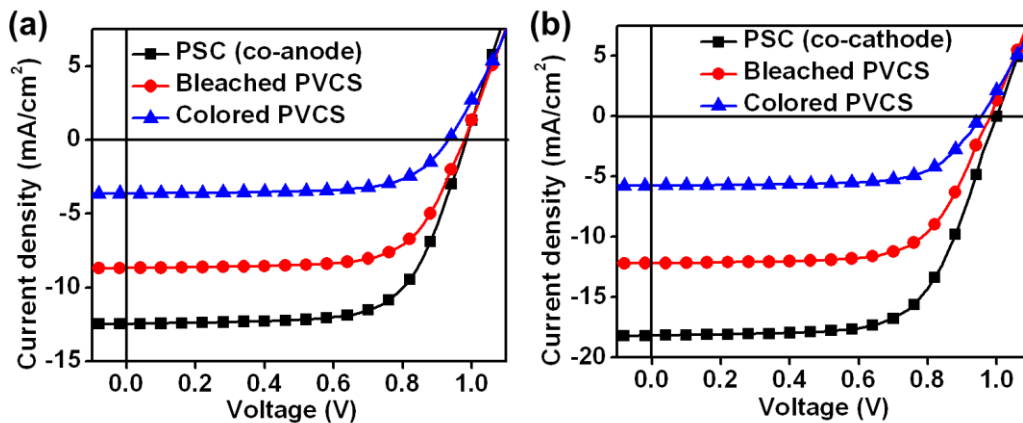


Figure 2.37. The photovoltaic performances of the PSCs utilizing in the two PVCSs before integration, the bleached PVCS, and the colored PVCS. The J - V curves of (a) co-anode PVCS and (b) co-cathode PVCS, respectively. The PSCs in the PVCSs is at a low-power working state under the colored state of the PVCSs.

Table 2.2. Lists of V_{oc} , J_{sc} , FF and PCE extracted from the J - V curves shown in the Figure 5(a) and 5(b).

Type	V_{oc} (V)	J_{sc} (mA/cm ²)	FF (%)	PCE (%)
Single PSC utilized in co-anode PVCS	0.983	12.46	67.3	8.25
Bleached co-anode PVCS	0.978	8.68	68.1	5.78
Colored co-anode PVCS	0.932	3.64	66.6	2.26
Single PSC utilized in co-cathode PVCS	1.000	18.17	65.4	11.89

Bleached co-cathode PVCS	0.981	12.18	66.8	7.98
Colored co-cathode PVCS	0.955	5.75	67.9	3.73

The low-power working state of PSC under the colored state of PVCSs also suggests an advantage of energy conservation in our device with extended lifetime. The color change of the ECS automatically switches off the solar light harvesting of the PSC and the photo-charging of the ECS, preventing the PSC from the long-time exposure under solar light, and slowing down the degradation of the PSC by blocking part of the solar light. Currently, the practical applications of the PSC are hindered by its stability, which can be resulted from ambient moisture or photo-degradation. ^[112-115] In view of this point, we conducted the photo-stability characterization of the as-fabricated PSC and our integrated co-cathode PVCS. Figure 2.38 shows the 4 normalized parameters (V_{oc} , J_{sc} , FF and PCE) as a function of the illumination time. We examined the photovoltaic performances of the PSC, bleached PVCS (to hold the device in a bleach stage, we disconnected the terminals A and C shown in the Figure 2.31 and keep the device in an open-circuit condition) and colored PVCS, which were continuously exposed to AM 1.5 G illumination for 5 hours. The PSC without the integration of ECS exposed directly to the solar light, and exhibited the most significant degradation, which is represented by its severe decreased J_{sc} and PCE to around 20% of their original values. The bleached PVCS shows a relatively slighter degradation, where the PCE is reduced to around 70% of the initial value after the continuous 5-hour photo-exposure. The photo-stability enhancement can mostly be attributed to that the bleached ECS selectively absorbs the part of the light and reflects the thermal radiation. ^{[80-81], [100]} When the ECS is fully

charged and turns to deep blue in the PVCSSs, the PSC part is under a low-power working state and its lifetime is prolonged. Once the ECS part is discharged and its color turns to be transparent, the PSC recovers to a working state.

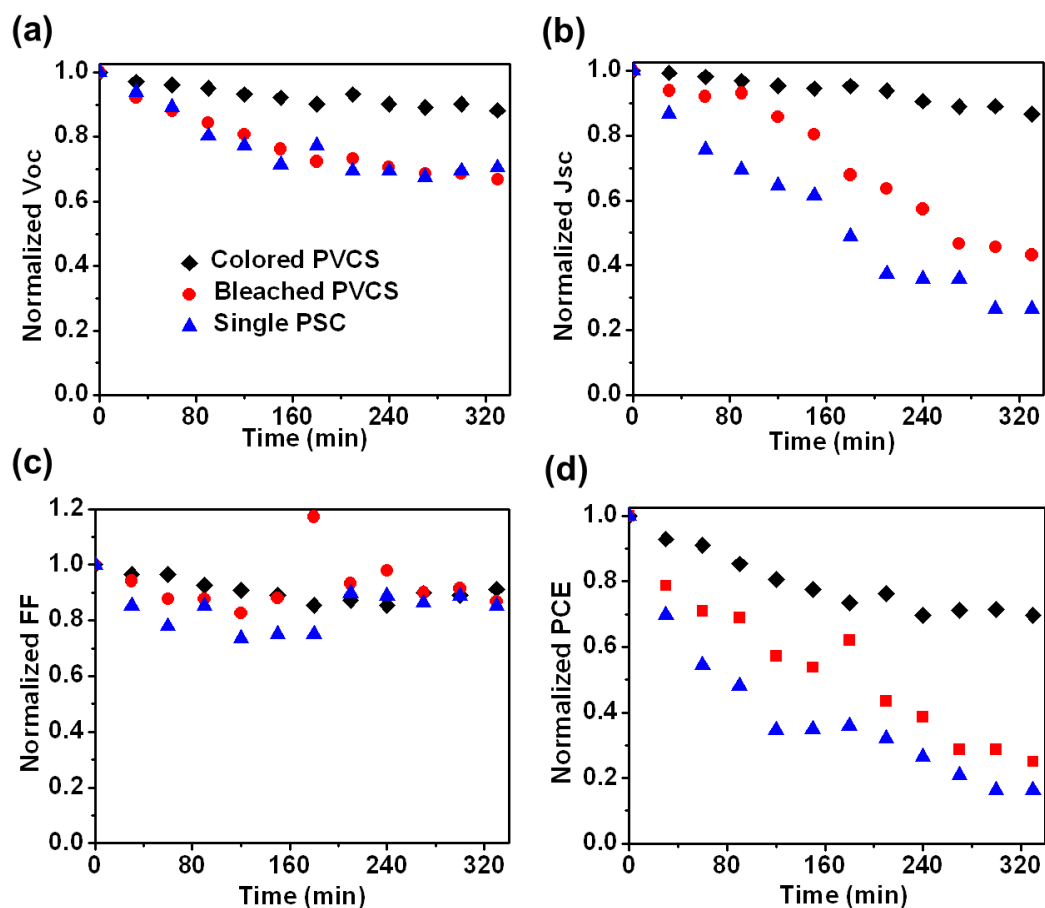


Figure 2.38. Photo-stability characterization of the as-fabricated PSC and the bleached/colored co-cathode PVCSS during 5-hour continuous illumination: normalized 4 parameters (a) V_{oc} , (b) J_{sc} , (c) FF and (d) PCE as a function of the illumination time. The original values (0 min) of the 4 parameters are set as 1. The variations of the parameters with illumination time are normalized according to the values at 0 min.

2.2.4. Summary

In summary, we demonstrate co-anode and co-cathodes PVCSSs integrating both semitransparent PSC and ECS. The PVCSSs provide a seamless integration of energy harvesting and storage device, automatic and wide color tunability, and enhanced

photo-stability of PSCs. The light power efficiency of the PV component in the co-anode (co-cathode) PVCS is 8.25 (11.89) %. The energy density, power density and areal capacitance of the co-anode (co-cathode) PVCS are 13.4 (24.5) mWh/m², 187.6 (377.0) mW/m² and 286.8 (430.7) F/m², respectively. Accompanied with energy storage, the color of energy storage part (“electrochromic shelter” of PSC) changes from semitransparent to dark-blue with a reduction in AVT from 85% (76.2%) to 35.1% (23.0%) for co-anode (co-cathode) PVCS. As the colored PVCS blocks off most of the illuminated light, it automatically switches off the photo-charging. The PSC then works under a low-power operating state, which prevents the PSC from long-time photo-exposure and prolongs its lifetime. Our works provide unprecedented advantages over conventional smart window design.

References

1. Augustyn, V., J. Come, M.A. Lowe, J.W. Kim, P.-L. Taberna, S.H. Tolbert, H.D. Abruña, P. Simon, and B. Dunn, *Nat. Mater.* **2013**, 12, 518.
2. Chae, J., K. Ng, and G. Chen, *Proceedings of the Institution of Mechanical Engineers, Part A: Journal of Power and Energy* **2010**, 224, 479.
3. Halper, M.S. and J.C. Ellenbogen, The MITRE Corporation, McLean, Virginia, USA **2006**, 1.
4. Conway, B.E., *Electrochemical supercapacitors: scientific fundamentals and technological applications* 2013: Springer Science & Business Media.
5. Burke, A., *J. Power Sources* **2000**, 91, 37.
6. Kötzt, R. and M. Carlen, *Electrochim. Acta* **2000**, 45, 2483.
7. Shi, F., L. Li, X.-l. Wang, C.-d. Gu, and J.-p. Tu, *Rsc Advances* **2014**, 4, 41910.
8. Wang, G., L. Zhang, and J. Zhang, *Chem. Soc. Rev.* **2012**, 41, 797.
9. Yu, Z., L. Tetard, L. Zhai, and J. Thomas, *Energy Environ. Sci.* **2015**, 8, 702.
10. Wang, Y., Y. Song, and Y. Xia, *Chem. Soc. Rev.* **2016**, 45, 5925.
11. Li, M., C. Liu, H. Cao, H. Zhao, Y. Zhang, and Z. Fan, *J. Mater. Chem. A* **2014**, 2, 14844.
12. Zhang, Y., N.W. Franklin, R.J. Chen, and H. Dai, *Chem. Phys. Lett.* **2000**, 331, 35.
13. Futaba, D.N., H. Hatori, K. Hata, M. Yumura, O. Tanaike, S. Iijima, T. Yamada, T. Hiraoka, Y. Kakudate, and Y. Hayamizu, *Nat. Mater.* **2006**, 5, 987.
14. Miller, J.R., R. Outlaw, and B. Holloway, *Science* **2010**, 329, 1637.
15. Manthiram, A., A.V. Murugan, A. Sarkar, and T. Muraliganth, *Energy Environ. Sci.* **2008**, 1, 621.
16. Faraji, S. and F.N. Ani, *J. Power Sources* **2014**, 263, 338.
17. Conway, B.E., *J. Electrochem. Soc.* **1991**, 138, 1539.
18. Sugimoto, W., H. Iwata, Y. Yasunaga, Y. Murakami, and Y. Takasu, *Angew. Chem. Int. Ed.* **2003**, 42, 4092.
19. Yuan, C., L. Hou, D. Li, L. Yang, and J. Li, *International Journal of Electrochemistry* **2012**, 2012.
20. Fang, J., B. Ding, and H. Gleiter, *Chem. Soc. Rev.* **2011**, 40, 5347.
21. Toupin, M., T. Brousse, and D. Bélanger, *Chem. Mater.* **2004**, 16, 3184.
22. Luo, J.-Y. and Y.-Y. Xia, *J. Electrochem. Soc.* **2007**, 154, A987.
23. Zhu, J., W. Shi, N. Xiao, X. Rui, H. Tan, X. Lu, H.H. Hng, J. Ma, and Q. Yan, *ACS applied materials & interfaces* **2012**, 4, 2769.
24. Jiang, H., T. Zhao, J. Ma, C. Yan, and C. Li, *Chem. Commun.* **2011**, 47, 1264.
25. Jiang, H., T. Sun, C. Li, and J. Ma, *Journal of Materials Chemistry* **2012**, 22, 2751.
26. Chen, W., R. Rakhi, L. Hu, X. Xie, Y. Cui, and H.N. Alshareef, *Nano Lett.* **2011**, 11, 5165.
27. Guo, Y., J. Li, M. Chen, and G. Gao, *J. Power Sources* **2015**, 273, 804.
28. Wu, Y., G. Gao, and G. Wu, *J. Mater. Chem. A* **2015**, 3, 1828.
29. Guo, H., W. He, Y. Lu, and X. Zhang, *Carbon* **2015**, 92, 133.
30. Huang, Y., J. Tao, W. Meng, M. Zhu, Y. Huang, Y. Fu, Y. Gao, and C. Zhi, *Nano Energy* **2015**, 11, 518.
31. Deng, Y., E. Peng, Y. Shao, Z. Xiao, Q. Dong, and J. Huang, *Energy Environ. Sci.* **2015**, 8, 1544.
32. ; Available from: <https://chem.libretexts.org/LibreTexts/>.
33. Runnerstrom, E.L., A. Llordés, S.D. Lounis, and D.J. Milliron, *Chem. Commun.* **2014**, 50,

- 10555.
34. Korgel, B.A., Nature **2013**, 500, 278.
 35. Österholm, A.M., D.E. Shen, J.A. Kerszulis, R.H. Bulloch, M. Kuepfert, A.L. Dyer, and J.R. Reynolds, ACS applied materials & interfaces **2015**, 7, 1413.
 36. Yang, P., P. Sun, Z. Chai, L. Huang, X. Cai, S. Tan, J. Song, and W. Mai, Angew. Chem. Int. Ed. **2014**, 53, 11935.
 37. Zhu, M., Y. Huang, Y. Huang, W. Meng, Q. Gong, G. Li, and C. Zhi, J. Mater. Chem. A **2015**, 3, 21321.
 38. Shen, L., L. Du, S. Tan, Z. Zang, C. Zhao, and W. Mai, Chem. Commun. **2016**, 52, 6296.
 39. Wen, R.T., C.G. Granqvist, and G.A. Niklasson, Adv. Funct. Mater. **2015**, 25, 3359.
 40. Chigane, M., M. Ishikawa, and M. Izaki, J. Electrochem. Soc. **2001**, 148, D96.
 41. Wei, D., M.R. Scherer, C. Bower, P. Andrew, T. Ryhänen, and U. Steiner, Nano Lett. **2012**, 12, 1857.
 42. Sonmez, G., H.B. Sonmez, C.K. Shen, and F. Wudl, Adv. Mater. **2004**, 16, 1905.
 43. Wang, K., H. Wu, Y. Meng, and Z. Wei, Small **2014**, 10, 14.
 44. Argun, A.A., P.-H. Aubert, B.C. Thompson, I. Schwendeman, C.L. Gaupp, J. Hwang, N.J. Pinto, D.B. Tanner, A.G. MacDiarmid, and J.R. Reynolds, Chem. Mater. **2004**, 16, 4401.
 45. Wang, K., H. Wu, Y. Meng, Y. Zhang, and Z. Wei, Energy Environ. Sci. **2012**, 5, 8384.
 46. Reddy, B.N., P.N. Kumar, and M. Deepa, ChemPhysChem **2015**, 16, 377.
 47. Wang, J., L. Zhang, L. Yu, Z. Jiao, H. Xie, X.W.D. Lou, and X.W. Sun, Nat. Commun. **2014**, 5, 4921.
 48. Polat, E.O., O. Balci, and C. Kocabas, Scientific reports **2014**, 4.
 49. Bao, W., J. Wan, X. Han, X. Cai, H. Zhu, D. Kim, D. Ma, Y. Xu, J.N. Munday, and H.D. Drew, Nat. Commun. **2014**, 5.
 50. Elbersen, R., W. Vijselaar, R.M. Tiggelaar, H. Gardeniers, and J. Huskens, Adv. Mater. **2015**, 27, 6781.
 51. Zhu, G., C. Pan, W. Guo, C.-Y. Chen, Y. Zhou, R. Yu, and Z.L. Wang, Nano Lett. **2012**, 12, 4960.
 52. Zeng, W., X.-M. Tao, S. Chen, S. Shang, H.L.W. Chan, and S.H. Choy, Energy Environ. Sci. **2013**, 6, 2631.
 53. Hunter, S.R., N.V. Lavrik, S. Mostafa, S. Rajic, and P.G. Datskos. *Review of pyroelectric thermal energy harvesting and new MEMS-based resonant energy conversion techniques*. in *Proc. SPIE*. 2012.
 54. Fakhruddin, A., R. Jose, T.M. Brown, F. Fabregat-Santiago, and J. Bisquert, Energy Environ. Sci. **2014**, 7, 3952.
 55. Qin, P., P. Sanghyun, M.I. Dar, K. Rakstys, H. ElBatal, S.A. Al-Muhtaseb, C. Ludwig, and M.K. Nazeeruddin, Adv. Funct. Mater. **2016**, 26, 5550.
 56. Shi, S., J. Yuan, G. Ding, M. Ford, K. Lu, G. Shi, J. Sun, X. Ling, Y. Li, and W. Ma, Adv. Funct. Mater. **2016**, 26, 5669.
 57. Zhao, J., Y. Li, A. Hunt, J. Zhang, H. Yao, Z. Li, J. Zhang, F. Huang, H. Ade, and H. Yan, Adv. Mater. **2016**, 28, 1868.
 58. O'regan, B. and M. Grätzel, Nature **1991**, 353, 737.
 59. Zhang, S., X. Yang, Y. Numata, and L. Han, Energy Environ. Sci. **2013**, 6, 1443.
 60. Yu, H., S. Zhang, H. Zhao, G. Will, and P. Liu, Electrochim. Acta **2009**, 54, 1319.
 61. Roy-Mayhew, J.D. and I.A. Aksay, Chem. Rev. **2014**, 114, 6323.

62. Yang, Z., J. Deng, H. Sun, J. Ren, S. Pan, and H. Peng, *Adv. Mater.* **2014**, 26, 7038.
63. Guo, W., X. Xue, S. Wang, C. Lin, and Z.L. Wang, *Nano Lett.* **2012**, 12, 2520.
64. Chen, T., L. Qiu, Z. Yang, Z. Cai, J. Ren, H. Li, H. Lin, X. Sun, and H. Peng, *Angew. Chem. Int. Ed.* **2012**, 51, 11977.
65. Søndergaard, R., M. Hösel, D. Angmo, T.T. Larsen-Olsen, and F.C. Krebs, *Mater. Today* **2012**, 15, 36.
66. Kim, T., J.-H. Kim, T.E. Kang, C. Lee, H. Kang, M. Shin, C. Wang, B. Ma, U. Jeong, and T.-S. Kim, *Nat. Commun.* **2015**, 6.
67. Li, G., R. Zhu, and Y. Yang, *Nature photonics* **2012**, 6, 153.
68. Wee, G., T. Salim, Y.M. Lam, S.G. Mhaisalkar, and M. Srinivasan, *Energy Environ. Sci.* **2011**, 4, 413.
69. Zhang, Z., X. Chen, P. Chen, G. Guan, L. Qiu, H. Lin, Z. Yang, W. Bai, Y. Luo, and H. Peng, *Adv. Mater.* **2014**, 26, 466.
70. Polman, A., M. Knight, E.C. Garnett, B. Ehrler, and W.C. Sinke, *Science* **2016**, 352, aad4424.
71. Bi, D., W. Tress, M.I. Dar, P. Gao, J. Luo, C. Renevier, K. Schenk, A. Abate, F. Giordano, and J.-P.C. Baena, *Science advances* **2016**, 2, e1501170.
72. Hodes, G., *Science* **2013**, 342, 317.
73. Xu, X., S. Li, H. Zhang, Y. Shen, S.M. Zakeeruddin, M. Graetzel, Y.-B. Cheng, and M. Wang, *ACS nano* **2015**, 9, 1782.
74. G. A. Niklasson, C. G. Granqvist, *J. Mater. Chem.* 2007, 17, 127.
75. N. I. Jaksic, C. Salahifar, *Sol. Energy Mater. Sol. Cells* 2003, 79, 409.
76. C. G. Granqvist, P. C. Lansaker, N. R. Mlyuka, G. A. Niklasson, E. Avendano, *Sol. Energy Mater. Sol. Cells* 2009, 93, 2032.
77. A. Cannavale, F. Fiorito, D. Resta, G. Gigli, *Energy Buildings.* 2013, 65, 137.
78. C. Bechinger, S. Ferrere, A. Zaban, J. Sprague, B. Gregg, *Nature* 1996, 383, 608.
79. R. Baetens, B. P. Jelle, A. Gustavsen, *Sol. Energy Mater. Sol. Cells* 2010, 94, 87.
80. A. Cannavale, G. E. Eperon, P. Cossari, A. Abate, H. J. Snaith, G. Gigli, *Energy Environ. Sci.* 2015, 8, 1578.
81. F. Malara, A. Cannavale, S. Carallo, G. Gigli, *Appl. Mater. Interfaces* 2014, 6, 9290.
82. M. Yang, H. Cho, J. Wu, *Nanoscale* 2014, 6, 9541.
83. J. Wu, M. Hsieh, W. Liao, W. Wu, J. Chen, *ACS Nano* 2009, 3, 2297.
84. X. Xiao, T. Li, P. Yang, Y. Gao, H. Jin, W. Ni, W. Ni, W. Zhan, X. Zhang, Y. Cao, J. Zhong, L. Gong, W. Yen, W. Mai, J. Chen, K. Huo, Y. Chueh, Z. Wang, J. Zhou, *ACS Nano* 2012, 6, 9200.
85. T. Chen, L. Qiu, Z. Yang, Z. Cai, J. Ren, H. Li, H. Lin, X. Sun, H. Peng, *Angewandte Chemie-International Edition* 2012, 51, 11977.
86. J. Bae, Y. J. Park, M. Lee, S. N. Cha, Y. J. Choi, C. S. Lee, J. M. Kim, Z. L. Wang, *Adv. Mater.* 2011, 23, 3446.
87. Q. Wang, H. Chen, E. McFarland, L. Wang, *Adv. Energy Mater.* 2015, 5, 1501418.
88. C. Chien, P. Hiralal, D. Wang, I. Huang, C. Chen, C. Chen, G. A. J. Amaratunga, *Small* 2015, 11, 2929.
89. J. Xu, Y. Chen, L. Dai, *Nat. Commun.* 2015, 6, 8103.
90. X. Xu, S. Li, H. Zhang, Y. Shen, S. M. Zakeeruddin, M. Graetzel, Y. Cheng, M. Wang, *ACS Nano* 2015, 9, 1782.
91. Z. Xie, X. Jin, G. Chen, J. Xu, D. Chen, G. Shen, *Chem. Commun.* 2014, 50, 608.

92. X. Chen, H. Sun, Z. Yang, G. Guan, Z. Zhang, L. Qiu, H. Peng, *J. Mater. Chem. A* 2014, 2, 1897.
93. A. L. Dyer, R. H. Bulloch, Y. Zhou, B. Kippelen, J. R. Reynolds, F. Zhang, *Adv. Mater.* 2014, 26, 4895.
94. K. Wang, H. Wu, Y. Meng, Y. Zhang, Z. Wei, *Energy Environ. Sci.* 2012, 5, 8384.
95. G. Wee, T. Salim, Y. M. Lam, S. G. Mhaisalkar, M. Srinivasan, *Energy Environ. Sci.* 2011, 4, 413.
96. Z. Yang, L. Li, Y. Luo, R. He, L. Qiu, H. Lin, H. Peng, *J. Mater. Chem. A* 2013, 1, 954.
97. T. Miyasaka, T. N. Murakami, *Appl. Phys. Lett.* 2004, 85, 17.
98. T. N. Murakami, N. Kawashima, T. Miyasaka, *Chem. Commun.* 2005, 26, 3346.
99. P. Yang, P. Sun, Z. Chai, L. Huang, X. Cai, S. Tan, J. Song, W. Mai, *Angewandte Chemie-International Edition* 2014, 53, 11935.
100. P. Yang, P. Sun, W. Mai, *Mater. Today.*, DOI: 10.1016/j.mattod.2015.11.007.
101. P. Yang, P. Sun, L. Du, Z. Liang, W. Xie, X. Cai, L. Huang, S. Tan, W. Mai, *J. Phys. Chem. C* 2015, 199, 16483.
102. S. Hashimoto, H. Matsuoka, *J. Appl. Phys.* 1991, 69, 15.
103. C. G. Granqvist, *Electrochim. Acta* 1999, 44, 3005.
104. R. Song, H. Jin, X. Li, L. Fei, Y. Zhao, H. Huang, L.W. Chan, Y. Wang, Y. Chai, *J. Mater. Chem. A* 2015, 3, 14963.
105. Y. Xie, Y. Liu, Y. Zhao, Y.H. Tsang, S.P. Lau, H. Huang, Y. Chai, *J. Mater. Chem. A* 2014, 2, 9142.
106. Z. Ren, A. Ng, Q. Shen, H. C. Gokkaya, J. Wang, L. Yang, W. Yiu, G. Bai, A.B. Djurisic, W. W. Leung, J. Hao, W. K. Chan, C. Surya, *Sci. Rep.* 2014, 4, 6752.
107. Z. Xue, X. Liu, N. Zhang, H. Chen, X. Zheng, H. Wang, X. Guo, *ACS Appl. Mater. Interfaces* 2014, 6, 16403.
108. K. Kim, T. Pfadler, E. Zimmermann, Y. Feng, J. A. Dorman, J. Weickert, L. Schmidt-Mende, *APL Mater.* 2015, 3, 106105.
109. K. Hong, K. Kim, S. Kim, I. Lee, H. Cho, S. Yoo, H. W. Choi, N. Y. Lee, Y. Tak, J. L., *J. Phys. Chem. C* 2011, 115, 3453.
110. J. Chen, J. Yang, Z. Li, X. Fan, Y. Zi, Q. Jing, H. Guo, Z. Wen, K. C. Pradel, S. Niu, Z.L. Wang, *ACS Nano* 2015, 9, 3324.
111. C. Law, L. Miseikis, S. Dimitrov, P. Shakya-Tuladhar, X. Li, P. R. F. Barnes, J. Durrant, B. C. O'Regan, *Adv. Mater.* 2014, 26, 6268.
112. T. Leijtens, G. E. Eperon, S. Pathak, A. Abate, M. M. Lee, H. J. Snaith, *Nat. Commun.* 2014, 4, 2885.
113. S. Ito, S. Tanaka, K. Manabe, H. Nishino, *J. Phys. Chem. C* 2014, 118, 16995.
114. G. Niu, X. Guo, L. Wang, *J. Mater. Chem. A* 2015, 3, 897

CHAPTER 3 Optoelectronic Random Access Memory with Integrated Sensing and Logic Operations

3.1 Introduction

In IoT systems, wireless sensors are usually embedded with memory devices to directly store the sensory data collected from the IoT objects and the stored data is then required to be transferred and processed in the data processing systems. In this processes, the data transfer from sensors to memories to processors can induce electric power consumption and slow the data transfer and process speed. To develop multifunctional devices integrated with sensing, data storage and processing is necessary for reducing the power consumption and the number of electronic devices in the integrated circuits and enables more efficient data sensing and processing systems. Optoelectronic resistive random access memories (RRAM) are one of the most promising devices for integrating sensing, data storage and processing functions. Different types of optoelectronic RRAMs with integrated functions and applications designed will be introduced and discussed in this and next chapters, respectively.

This introduction section will first briefly review the working principle and materials for conventional RRAMs operated by electrical methods, followed by the introduction of the optoelectronic memories and the related research development in recent years.

3.1.1. Overviews of Resistive Random Access Memories (RRAMs)

A random access memory (RAM) is a hardware device which is responsible for the data storage in the computer. RAM can be classified into volatile RAM and non-volatile RAM. For a volatile RAM, such as flash memory, static random access memory (SRAM) and dynamic random access memory (DRAM), the data will be erased once the power is removed. For these volatile memories, they all have advantages and disadvantages. For example, flash memories adopt high capacity, but the switching speed is relatively low. SRAMs have fast switching speed, but low capacity and also SRAMs are volatile devices. Although DRAMs have high density and capacity, but the power consumption is high since they are required to be refreshed frequently. In recent years, emerging non-volatile RAMs have drawn increasing attentions in the memory industry, in which the data can be stored and retained for a long time even the power is removed. There are many types of non-volatile RAMs, as phase change random access memory (PRAM), magnetic random access memory (MRAM), ferroelectric random access memory (FRAM), and resistive random access memory (RRAM). Among these non-volatile RAMs, RRAMs are considered as promising next-generation memory devices for the simple fabrication processes, high integration density, low power consumption, scalability, non-destructive readout process, and fast switching speed.

3.1.2. Basic working principles

A RRAM are generally in a MIM (metal-insulator-metal) structure, in which an

insulating layer is sandwiched between two metal electrodes. Two resistance states, high resistance state (HRS) and low resistance state (LRS), can be switched in RRAM device under the externally applied voltage. The HRS and LRS correspond to logic 1 and logic 0, respectively. The switching behaviors can be classified into unipolar switching, bipolar switching and nonpolar switching according to different voltage polarity. For unipolar switching, both set and reset processes are initiated by the voltage with same polarity. For the bipolar switching, the voltage polarity is opposite for set and reset processes. For the nonpolar switching, the set and reset processes can be done with either positive voltage bias or negative voltage bias. The three switching IV curves are illustrated in Figure 3.1. For all those switching behaviors, a compliance current is usually employed to limit the setting current and prevent the device from breaking down.

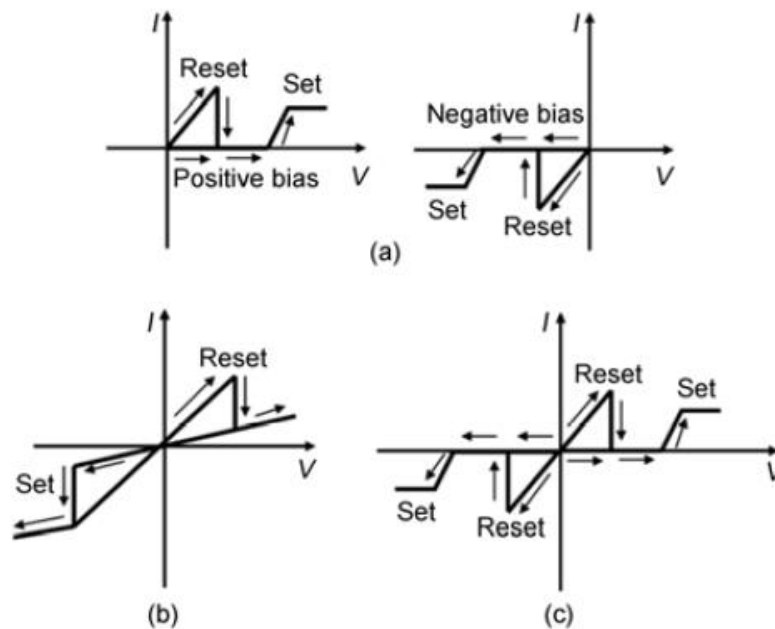


Figure 3.1. Resistive switching behaviors. (a) Unipolar switching. (b) Bipolar switching. (c) Nonpolar switching.^[1]

3.1.3. Key evaluation parameters

(1) Operation voltage

The operation voltage (including programming voltage and erasing voltage) is one of the key parameter in evaluating a RRAM performance. A low operation voltage can cause low power consumption. Additionally, the reliability can be an issue when the operation voltage is high. The operation voltages in RRAM devices are usually within a few volts.

(2) Switching speed

Switching speed can describe the shortest time to switch a device. The combination of fast switching speed and low operation voltage can bring a low power consumption in the memory cell. The switching speed of RRAMs is usually within the range of 100 ns, or even below the ns.

(3) ON/OFF ratio

ON/OFF ratio is the ratio of resistance at OFF state to the ON state. The accuracies of writing and erasing are directly dependent on the ON/OFF ratio. Generally, an ON/OFF ratio larger than 10 is required to differentiate the HRS and LRS. In RRAM devices, a large ON/OFF ratio allows for high density devices with multilevel storage.

(3) Endurance

Endurance can used to describe the cycling capability of a memory cell and is the number of working cycles before HRS and LRS cannot be distinguished. Currently, the endurance of RRAMs can reach up to 10^{12} cycles, which is comparable to the flash memory.

(4) Retention time

Retention time of a RRAM refers to the time that the resistance can be retained after set or reset process, which represents the time that the stored content can be retained in a memory cell. Generally, a retention time of at least 10 years have to be achieved in commercial memory products.

(5) Multilevel storage

Multilevel storage is the ability of memory cell to store multiple values, which means the memory cell can be operated to multiple resistance states. Memory cells with multilevel storage ability allows for high data storage density and are required to have large ON/OFF ratio to guarantee each resistance states are distinguishable. Multilevel storage can generally be realized by controlling the sweeping voltage or the compliance current.

3.1.4. Materials and switching mechanisms

This chapter will mainly overview three types of RRAM according to different materials and switching mechanisms, including oxide-based RRAM, conducting-bridge RAM (CBRAM) and carbon-based RRAM. In the oxide-based RRAM, the switching mechanism is dominated by the formation and migration of oxygen ions and oxygen vacancies. CBRAM is based on the formation of conductive filament consisting of metal atoms.

3.1.4.1. Anion migration

The storage media in anion-migration based RRAM are generally metal oxides and silicon oxides. Among the metal oxides, TaO_x, AlO_x, TiO_x, NiO_x and HfO_x are commonly used metal oxides in RRAM for their compatibility in CMOS and excellent resistive switching performances. The switching in the anion migration based RRAM is mainly based on the formation and migration of oxygen vacancies. During the switching processes, the oxygen vacancies can migrate under the externally applied voltage, which lead to the cation valance change in the oxide material. Thus, anion migration based RRAMs are also valence change memories (VCMs). Here, the switching in anion migration based RRAMs can be roughly classified into filament-based switching and interface-based switching.

(1) Filament-based switching

One of the common switching mechanism in oxide-based VCM is the filamentary switching mechanism based on the formation of conducting path which consists of continuous oxygen vacancies. These processes are usually accompanied with redox/reduction reactions. A schematics of a typical switching behavior is shown in Figure 3.2. Uner the electric field, O²⁻ will be ionized and drifted to the anode with leaving oxygen vacancies V_o in the oxide layer. The oxygen vacancies left in the oxide form a conductive path between the top and bottom electrodes, leading to a transition from HRS to LRS. The anode materials are required to be able to store the oxygen ions, such as noble metals or oxygen-poor films. During the reset process, oxygen vacancies migrated back to the oxide and recombine with oxygen ions and the device is switched

back to HRS. [2]

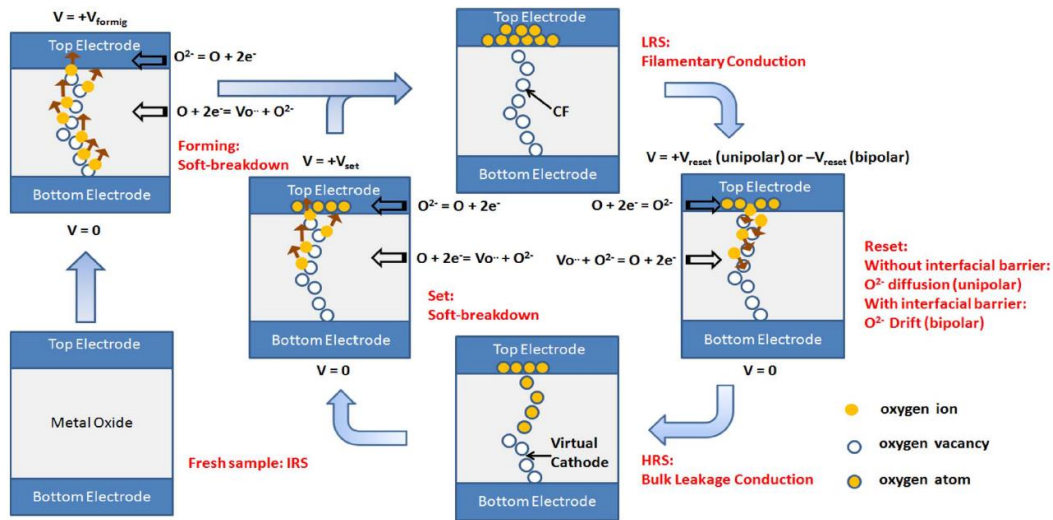


Figure 3.2 Schematics of the switching behavior in an oxide-based RRAM based on filamentary switching mechanism. [2]

The metal electrode material can influence the switching mode and behaviors in the oxide RRAM. In most of the cases, when both of the top and bottom electrodes are noble metals (*e.g.* Pt, Ru), the switching behavior is unipolar. The unipolar switching can usually be observed in the oxide systems, such as Pt/NiO/Pt, [3] Pt/TiO₂/Pt, [4] Pt/ZnO/Pt, [4] Pt/ZrO₂/Pt. [5] Bipolar switching usually occurs in the oxide RRAM with oxidizable electrodes, such as Ti or TiN. Typical bipolar devices are reported as TiN/ZnO/Pt, [4] Ti/ZrO₂/Pt, [6] TiN/HfO₂/Pt [7] and Pt/NiO/SrRuO₃. [8] The mechanisms of different switching modes are still controversial. Generally, the unipolar switching is ascribed to the Joule heating effect, which causes the filament rupture during the reset processes. [9] For the bipolar device, ionic migration model has been put forward, for which a reverse voltage bias can drive the oxygen ions back to the oxide layer. [10] The metal electrode selection can also affect the switching performances. It has been reported that better uniformity of RRAM can be obtained with Ti electrode. [11] By comparing with the Pt/ZrO₂/Pt and Al/ZrO₂/Pt devices, Ti/ZrO₂/Pt device exhibited

narrower distribution of operation voltages (set and reset) and resistances (HRS and LRS).^[11] Furthermore, the RRAM devices with metal electrodes, such as TaN, ZrN_x and TiN, exhibit excellent performances. The ZrN_x/HfO_x/Pt device shows better endurance larger than 10⁶ and longer retention time than the Pt/HfO_x/Pt device.^[12] This can be attributed to the formation of ZrON layer at the interface which can better store the oxygen ions.^[13, 14]

HfO_x with rich defects is a suitable material for the RRAM device. TiN/HfO_x/Pt is a common structure which exhibits good bipolar switching behavior.^[15] To further improve the switching performance and also make the fabrication more CMOS compatible, a buffer layer Ti is employed in the structure. The buffer layer Ti can serve as an oxygen reservoir and help to store the oxygen atoms from the HfO_x film. Lee *et al.* reported a 1T1R (1 transistor and 1 RRAM) structure, in which RRAM device is in a structure of TiN/Ti/HfO₂/TiN.^[16] The device achieves good endurance of 10⁶ cycles, fast operation speed of 10 ns, large ON/OFF ratio (>100), 100 % device yield, multi-level storage. Other metal capping layers such as Ta and AlCu are also applied into the HfO_x RRAM device, in which stable switching can be achieved but with a smaller ON/OFF ratio.^[12] AlO_x RRAM behaves similar to HfO_x based device. Superior to the HfO_x device, it demonstrates a lower reset current because of a larger band gap in AlO_x. Wu *et al.* first reported an Al/AlO_x/Pt device with reset current lower than 1 μA. Later, by doping the AlO_x with nitrogen, a reset current lower than 100 nA can be achieved, which also means a low power consumption.^[17] Furthermore, the high resistance at HRS allows for the application of large scale memory arrays without selectors.^[18]

Different from HfO_x , RRAM devices based on NiO usually exhibit unipolar switching behavior with metal electrodes such as Au, Pt, W, Ni and Ru. The set voltage and reset voltage are reported generally less than 3 V and 2V, respectively. Good data endurance ($>10^6$) and long retention time (1 year) can also be achieved in the NiO based RRAM device.^[19] By doping NiO with Ti, the operation speed can be further improved compared with the pure NiO. The Pt/Ti:NiO/Pt device achieved a fast switching speed ($<5\text{ns}$).^[20] More interestingly, the abnormal set process in pure NiO device can be suppressed since Ti serves as another oxygen reservoir in the system. Taking the advantages of unipolar switching behavior, NiO allows for the design of 1D1R (1 diode 1 memory) structure. However, the poor uniformity is a general issue in the NiO RRAM which can limit the application of 1D1R structure design.^[21] Among these metal oxides, TaO_x has demonstrated excellent endurance. TaO_x usually has two phases: more conductive TaO_{2-x} phase and more insulate $\text{Ta}_2\text{O}_{5-x}$ phase. Lee et al. reported a Pt/ TaO_{2-x} / $\text{Ta}_2\text{O}_{5-x}$ /Pt RRAM with demonstrating excellent endurance up to 10^{12} cycles.^[22] In addition to the metal oxides, silicon oxide has also considered as a promising material for RRAM device design, which adopts good chemical stability, endurance and retention. An endurance of 10^6 cycles has been reported in a Ni doped SiO_2 RRAM device and there is only slight degradation of ON/OFF ratio after 10^4 s at 85°C .^[23]

(2) Interface-based switching

For the interface-based switching, the barrier height between the metal and semiconductor layer greatly influences the current. The externally applied voltage can modify the barrier height, which corresponds to different resistances states. The

interface-based switching behaviors have been observed in perovskite oxides and binary oxides. In an interface-type VCM, the sandwiched semiconductor layer usually forms an Ohmic contact with one metal electrode and Schottky contact with other electrode.^[24] Figure 3.3 shows the typical interface-based switching in systems of $M/\text{Pr}_{0.7}\text{Ca}_{0.3}\text{MnO}_3/\text{SrRuO}_3$ (M/PCMO/SRO) and $M/\text{SrTi}_{0.99}\text{Nb}_{0.01}\text{O}_3/\text{Ag}$ (M/Nb:STO/Ag).^[25] M stands for the top electrode (Ti, Au or SRO). Ohmic contacts will form at Ag/Nb:STO interface and SRO PCMO. While the interfaces Au/Nb:STO, SRO/Nb:STO and Ti/PCMO exhibit rectifying behavior that can be observed from the IV curves, indicating the Schottky barriers formed. As a positive voltage is applied to the Ag electrode, oxygen vacancies can migrate and accumulate at the SRO/Nb:STO interface, which leads to a lowered Schottky barrier and a transition to a lower resistance state (Figure 3.3). Kim et al investigated the effects of different metal electrodes (Pd, Au, Al, Cr and Pt) on the resistive switching behavior of PCMO/Pt system.^[26] It has been observed in the experiment that only the devices with Cr and Al top electrode exhibit resistive switching behavior. One of the key factor that influences the switching behavior is the metal oxide formed at the metal/semiconductor interface. The as-deposited metal on the oxide layer can capture oxygen ions from the oxide layer, leaving oxygen vacancies in the oxide layer. For example, a thin TiO_x layer can be formed at the Ti/ TiO_2 interface, leading to the abundant oxygen vacancies in the TiO_2 layer. Thus, the resistive behavior can also be influenced by the abilities of the metal oxide formation. It has been reported by Yang *et al.*, the switching behaviors in $\text{La}_{0.7}\text{Ca}_{0.3}\text{MnO}_3$ (LCMO) are influenced by the formation energy of the metal oxides.^[27]

The investigations of switching behaviors with different metal electrodes provide more understandings of interface-based switching mechanisms.

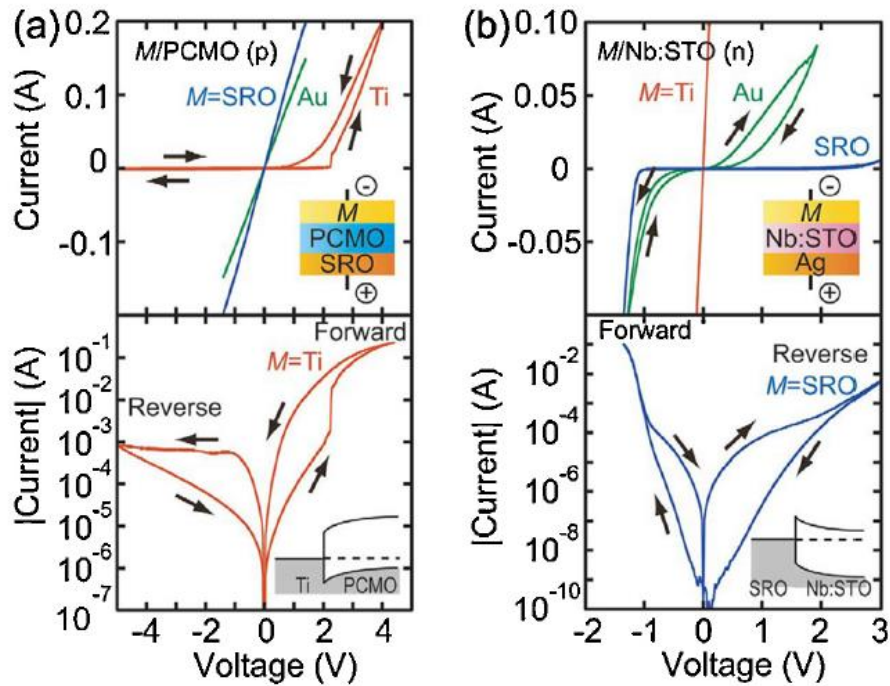


Figure 3.3. Resistive switching behaviors in M/PCMP/SRO and M/Nb:STO/Ag devices.^[25]

3.1.4.2. Cation migration

The cation-type RRAM involves in the formation and dissolution of conductive filament consisting of metal atoms, which is also named as conductive bridging RAMs (CBRAM). In the RRAMs based on cation migration, it usually includes an electrochemically active electrode (CE) (*e.g.* Ag or Cu) and an electrochemically inert electrode (IE) (*e.g.* W, Pt or Au). The formation of metal atom consisted filament can be expressed in the following steps with an Ag electrode as an example (Figure 3.4^[28]): (1) dissolution of Ag to Ag^+ under the externally applied voltage. (2) migration of Ag^+ toward the inert electrode under the electric field (3) reduction of Ag^+ to Ag (4) growth of Ag filaments. As the filament connects the top electrode and bottom electrode, a

transition from HRS to LRS will occur. Under a reverse bias voltage, the Ag filament will be dissolved and the device will be switched back to HRS.

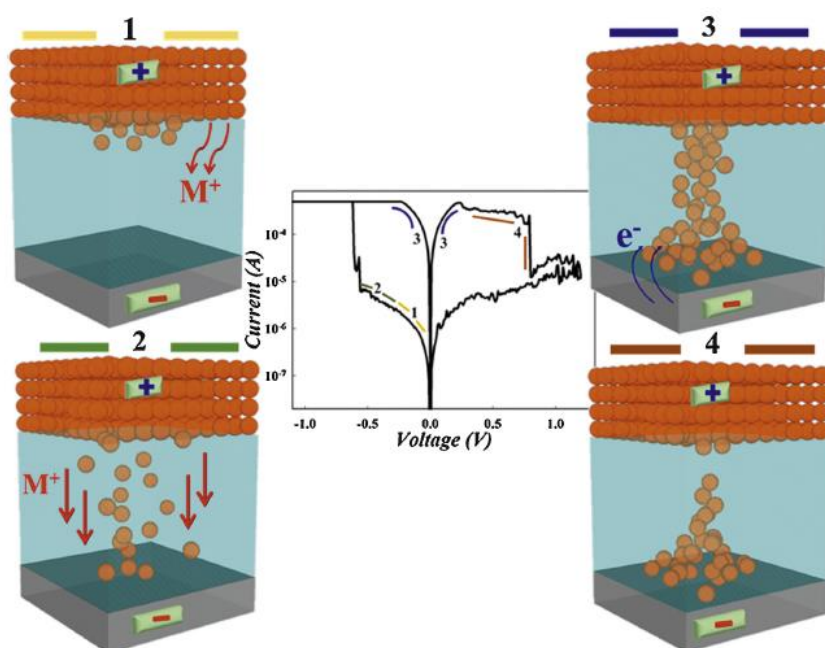


Figure 3.4. Schematics of switching mechanisms in CBRAM.^[28]

CBRAMs have drawn great attentions in the industry because of their excellent performances, such as low operation voltage, large ON/OFF ratio, compatibility with CMOS technology. Furthermore, the large ON/OFF ratio, generally larger than 10^6 , enables multi-level storage, which allows for the application of 1T2R structure instead of the SRAMs. This can reduce the power consumption and area occupation.

The electrochemically active electrodes used in CBRAM include Cu,^[29] Ni,^[30] Al,^[31] Ag,^[32] Zn,^[33] Nb,^[34] etc. Among the above metals, Cu and Ag are the most common metal for CBRAM because of the lower standard electrode potentials^[35, 36] and the weak interactions between $\text{Cu}^{2+}/\text{Ag}^{2+}$ and semiconductor layer. The relatively lower standard electrode potentials allows the metal ions to be easily electrochemically dissolved and the weak interaction with semiconductor material enable them to migrate easily inside. Various storage media have been explored for CBRAMs, including chalcogenides (*e.g.*

Ag₂S, GeSe_x, GeTe), oxides (e.g. SiO₂, Ta₂O₅, ZrO₂), halides (e.g. AgI), amorphous Si, and organic materials (e.g. fluorine, P3HT).

Ge-based chalcogenide glasses have been extensively studied as CBRAM storage media, in which Cu²⁺ and Ag²⁺ exhibit high ion mobility.^[37] Liaw et al and Choi et al. have reported a Ag/GeSe/W CBRAM with high ON/OFF ratio larger than 10⁵ and low set voltage of 0.2 V.^[38] Kozicki *et al.* reported a device with Ag/Ag₃₃Ge₂₀Se₄₇/Ag structure, which exhibits excellent endurance up to 10¹⁰.^[39] However, the operation speed in these systems are not sufficient for fast switching memory application. Hasegawa *et al.* later studied the response time in Ag₂S and Cu₂S based devices.^[40] The response time shows set voltage-dependent characteristics. It has been suggested that the response time of the memory device can be largely reduced with a higher set voltage exponentially. Good retention characteristics have also been reported in Ge-based chalcogenide devices. A retention time up to 11 h have been demonstrated in the Cu/Ge_{0.4}Se_{0.6}/W CBRAM device with a compliance current of 200 μA. Jameson *et al.*^[41] and Vianello *et al.* ^[42] also reported a good retention >10⁶ s at 200 °C and >10⁵ s at 130 °C in Ag/GeS₂/W and Cu/Sn:GeS₂/W CBRAM. Multi-level storage capability is also one of a significant characteristic for high-density data storage. Kund group demonstrated over 10 resistance states in Al/Cu/Ge_{0.2}Se_{0.8}/W memory cell by controlling the compliance current from 1 nA to 1mA.^[43] The Se content can affect the LRS current. With compliance current lower than 10 μA, the Ge_{0.2}Se_{0.8} based device shows higher LRS current than that in Ge_{0.5}Se_{0.5} since Cu²⁺ mobility is higher in the semiconductor layer with higher Se content. However, the HRS current degrades faster

in $\text{Ge}_{0.2}\text{Se}_{0.8}$ device because of the thinner filament formed. Thus, the switching behaviors can be controlled adjusting the composition in GeSe_x electrolyte according to different application demands.

Although chalcogenide based CBRAMs have exhibited excellent performances, the non-compatibility with CMOS technology restricts the applications for next-generation non-volatile memories. Thus, oxide-based CBRAM such as SiO_2 ,^[44] GeO_x ,^[45] Ta_2O_5 ,^[46] ZrO_2 ^[47] have been investigated for more compatible devices with CMOS technology. Schindler *et al.* reported low operation current of 1 nA in the W/Cu: SiO_2 /Cu memory cell.^[44] Good data retention and large ON/OFF ratio have been demonstrated in a Cu/ GeO_x /W device, in which the ON/OFF ratio reaches larger than 10^8 and both LRS and HRS can be retained over 200 h at 85 °C.^[48] Endurance larger than 10^7 has also been reported in the Cu/ SiO_2 /W CBRAM and the CBRAM exhibits multilevel storage controlled by different compliance currents. Good uniformity and stability have also been reported in the oxide-based RRAM. Liu et al. fabricated RRAM device with structure of Ag/ ZrO_2 /Cu nanoparticle/Pt.^[49] With the inserted Cu nanoparticle in the device, the device uniformity has been improved since the Cu nanoparticles can guide the filament growth and reduce the random filament formation and rupture. Although good performances can be achieved and compatibility can be solved in the CBRAMs, as the remaining filament exists after each switching cycle, the current at HRS varies from cycle to cycle. Thus, CBRAMs with bilayer materials are then developed with improved the cycling switching stability.

Bilayer materials such as $\text{MoO}_x/\text{GdO}_x$,^[50] Cu-Te/ GdO_x ,^[51] $\text{GeSe}_x/\text{TaO}_x$,^[52] Ti/ TaO_x

^[53] have been studied to control the metal ion diffusion and improve the uniformity in CBRAMs. By using bilayer MoO_x/GdO_x instead of single MoO_x layer in CBRAM, the reset current is reduced from 1mA to 300 μA.^[50] Comparing the single layer oxide based CBRAM Al/Cu/TaO_x/W with bilayer oxide based CBRAM Al/Cu/TiO₂/TaO_x/W, an improved LRS uniformity was observed in bilayer device, which can be attributed to the controlled Cu migration in the TiO₂ layer.^[53] The reset current is also lower in bilayer device than the single layer device. Similar characteristics have also been observed in the Cu/TiW/Al₂O₃/W device with showing low reset current of 10 μA. Excellent endurance >10⁷ cycles and fast switching response of 5 ns are reported with the employment of bilayer materials.^[54] The bilayer structured CBRAMs are promising for the next-generation non-volatile RRAM application.

3.1.4.3. Charge trapping/de-trapping

In addition to the ion migration, another common mechanism involved in RRAM is charge trapping and de-trapping.^[55] As the charge carriers are injected in from the electrodes, they may be trapped in the bulk semiconductor or metal/semiconductor interface. The charge carrier trapping can influence the charge carrier transport in the semiconductor material or modify the energy barrier of carrier injection, which then further lead to the resistive switching behavior. According to different distribution state of charge traps, the switching mechanisms can be classified into three categories.

(1) Interfacial charge traps

In this type of switching, there are charge traps existing at the semiconductor/metal

interface. The trapping states at the interface can determine the Schottky barrier and the contact resistance, which can be modulated by the external voltage. For example, at the Au/Nb:STO interface, a Schottky barrier can be formed and rectifying I-V behavior can be observed in Figure 3.5.^[56] The traps are introduced during the Au deposition process. As a negative bias is applied to the junction, electrons in the traps are extracted, leaving a lower and thinner Schottky barrier. Meanwhile, the device is switched to LRS. As a reverse bias is applied, the electrons are injected into the interfacial traps and the Schottky barrier recovers to the original state, corresponding to HRS. The similar switching behavior has also been reported in the Pt/BSTO/Pt devices.^[57]

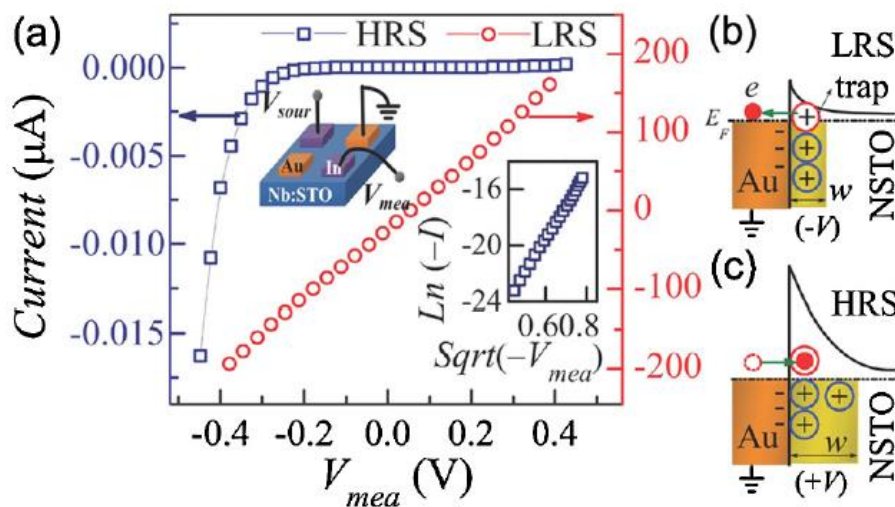


Figure 3.5. Resistive switching behavior in Au/Nb:STO junction: IV characteristics and switching mechanism.^[56]

(2) Charge traps provided by a nanoparticle layer

Figure 3.6a shows a schematic of nanoparticle layer as trap provider in an RRAM device. The semiconductor material can either be inorganic materials (*e.g.* ZnO^[58]) or organic materials (Alq₃)^[59]. The nanoparticles used in this case are usually Cu or Al nanoparticles with thickness below 10 nm.^[60] Both bipolar switching and unipolar

switching can occur for this switching mechanism. Figure 3.6b and c shows a typical bipolar switching in Cu/ZnO/Cu (3nm)/ZnO/Pt RRAM device.^[58] By fitting the IV curves, the IV characteristics at LRS satisfy the space charge limited current (SCLC) injection. Thus, the switching behavior in the device can be explained by the trap-filled SCLC model. Figure 3.6d and e illustrate an unipolar switching in a RRAM with structure of Al/Alq₃/Al(5 nm)/ Alq₃/Al.^[59] A positive voltage sweep to V_{\min} switches the device from LRS to HRS and a positive voltage to V_{th} switches the device to LRS. The region between V_{\max} and V_{\min} may be attributed to the tunneling of electrons in the traps and the induced electric field is in opposite direction with the external electric field, leading to a drop in current. The abrupt switching at V_{th} can be ascribed to the detrapping process of trapped electrons.

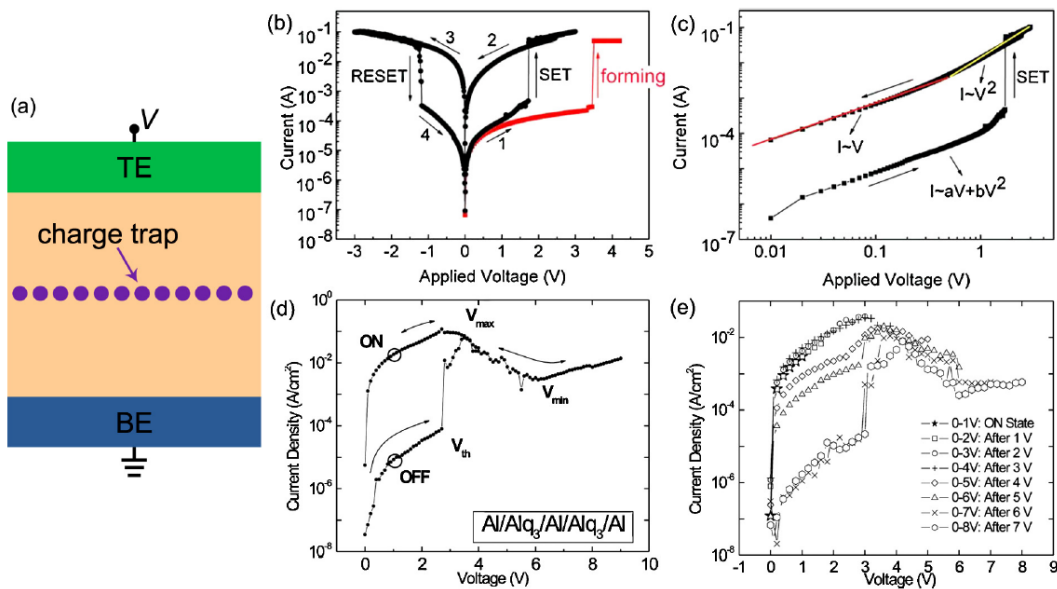


Figure 3.6 (a) Schematics of a RRAM device with nanoparticle layer. (b) and (c) Resistive behavior in the Cu/ZnO/Cu(3 nm)/ZnO/Pt RRAM.^[58] (d) and (e) Resistive switching behavior in the Al/Alq₃/Al(5 nm)/Alq₃/Al RRAM.^[59]

(3) Randomly distributed charge traps

The randomly distributed charge traps can be classified into nanoparticle and atomic

traps. The nanoparticle traps utilized in RRAM include metal nanoparticles (Au, Ag)^[60], semiconductor nanoparticles (ZnS, CdSe, ZnO)^[61], graphene quantum dots and carbon nanotubes^[62]. The switching mechanisms are similar to the mechanism discussed in the traps provided by a nanoparticle layer. The switching behaviors can be explained by trap-filled SCLC model. As for the atomic traps, the intrinsic crystal defects (*e.g.* vacancies) are common atomic traps for RRAM switching. The RRAM based on these traps also exhibit typical bipolar switching behavior and the switching characteristics satisfy the trap-filled SCLC model.^[63]

3.1.5. Optoelectronic resistive switching memories

Except for the conventional electrically switched RRAM, optical excitation is one of the methods to manipulate the RRAM operation, which allows to store light information with an electric readout at low programming voltages and involve in the storage and transport of secured information. By providing light as an extra control parameter, it is promising to realize integrated multi-functionalities in the computing systems, such as multi-level data storage, light-sensing, demodulating and arithmetic functions.

Optoelectronic RRAMs have been widely explored in recent years and have demonstrated the potentials in different applications such as image sensors, demodulators, and artificial retinas. The storage media in optoelectronic RRAMs that reported including ZnO nanorods, single layer and few-layer MoS₂, ZnO/SrTiO₃, CeO_{2-x}/AlO_y, graphene/MoS₂.

ZnO is commonly used storage medium in RRAM. By virtues of good light

absorption properties, it is also promising for an optoelectronic memory design. Yong developed an optically switched ITO/ZnO nanorods/Au memory device which exhibits light incident angle-dependent resistance states.^[64] The different illumination angle can select the switching behaviors, which is promising for the application of various functional devices. Wu group also synthesizes ZnO nanorods on SrTiO₃.^[65] The Schottky junction formed at interface exhibits rectification properties with an ON/OFF ratio of 10³. With the assistance of light, the ON/OFF ratio can be further increased to 10⁴, which can be attributed to the de-trapping of trapped electrons at ZnO/SrTiO₃ interface and thus a lowered Schottky barrier. Light tunable non-volatile resistive switching behavior can be achieved in the device, which also suggests a potential sensing function.

Single-layer and few-layer MoS₂ are attractive materials for optoelectronic memory application for the tunable bandgap, light absorption and unusual defect physics. A single layer MoS₂ optoelectronic memory was reported by Cho *et al.*, in which optically programmed ON/OFF ratio reaches >10⁷ and multi-level data storage, stable data storage can be achieved (Figure 3.7).^[66] In the device design, the single-layer MoS₂ serves as channel and light-absorption material. Au nanoparticles are introduced as charge trapping layers. The injected electrons from gate transfer from Au nanoparticles to MoS₂ valence band which prevent the recombination of photo-generated electrons and holes in MoS₂ and enables non-volatile data storage. By combining the gate voltage and optical input, non-volatile multi-level data storage can be achieved as shown in Figure 3.7 b, d and e. This device enables the storage of light signals at low

programming voltages and the multi-level data storage allows for the increased memory density. Kim et al. also adopted single-layer MoS₂ to demonstrate an optoelectronic memory for potential image sensing application.^[67] Traditional image sensing systems includes a photodetector and a memory device. The MoS₂ optoelectronic memory device provide a simple method to integrate the two components into one single device, which enables a lower power consumption and complexity in the circuit design. The switching mechanisms are based on the charge trapping and de-trapping at the MoS₂/SiO₂ interface, which modify MoS₂ conductivity. The linear relationship between light exposure dosage and output electrical current is potential for the applications in image sensing, which enables the detection of image contrast. Graphene/MoS₂ hybrid structure was also investigated for the optoelectronic memory based on the gate tuned charge exchange between the MoS₂ and graphene layers. In addition to the sensing and memory functions, Tan *et al.* demonstrated an optoelectronic RRAM with integrated demodulating and arithmetic functions in an ITO/CeO_{2-x}/AlO_y/Al device.^[68] The optoelectronic RRAM can be optically written and electrically erased, in which the programming and erasing processes are based on photo-induced electron de-trapping and electrically induced electron trapping (Figure 3.9 a and b). Multi-level storage can be achieved in the device by tuning the light wavelength and power density (Figure 3.9 c and d). The light information such as light intensity and wavelength can be demodulated into electrical signals. Additionally, the linear relationship between the current and light pulse number enables the conduction of add function. This device integrates sensing, memory and computing functions in one device, which provides

possibilities for designing multifunctional devices with lowering the power consumption and complexity.

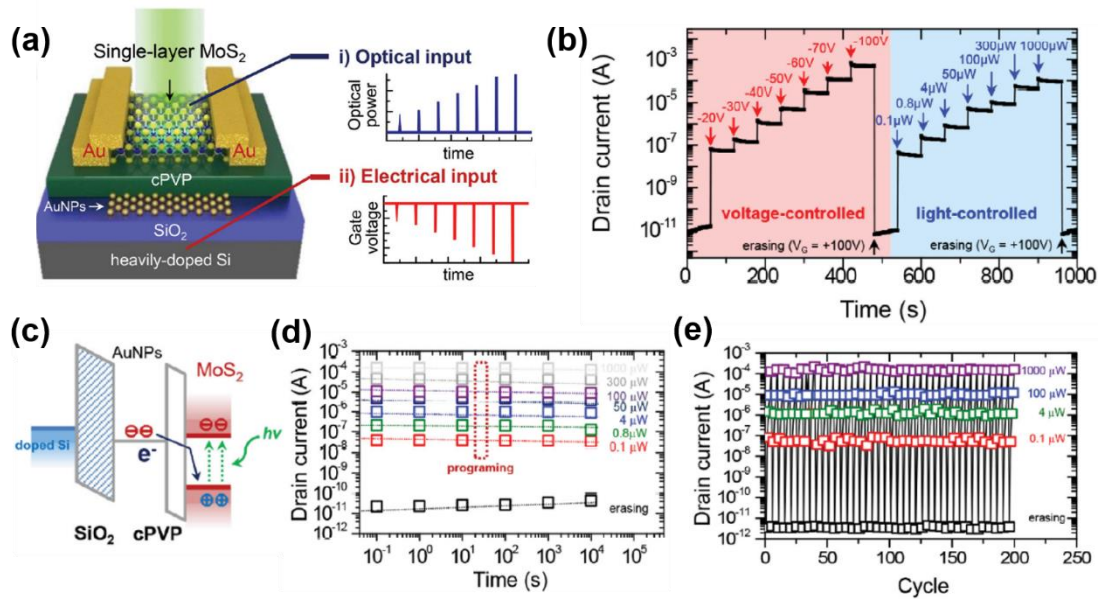


Figure 3.7. Single-layer MoS₂ based optoelectronic memory. (a) Device structure. (b) Optically programmed multi-level storage. (c) Band diagram illustrating the charge transfer between MoS₂ and Au nanoparticles. (d) Retention properties. (e) Endurance tests.^[66]

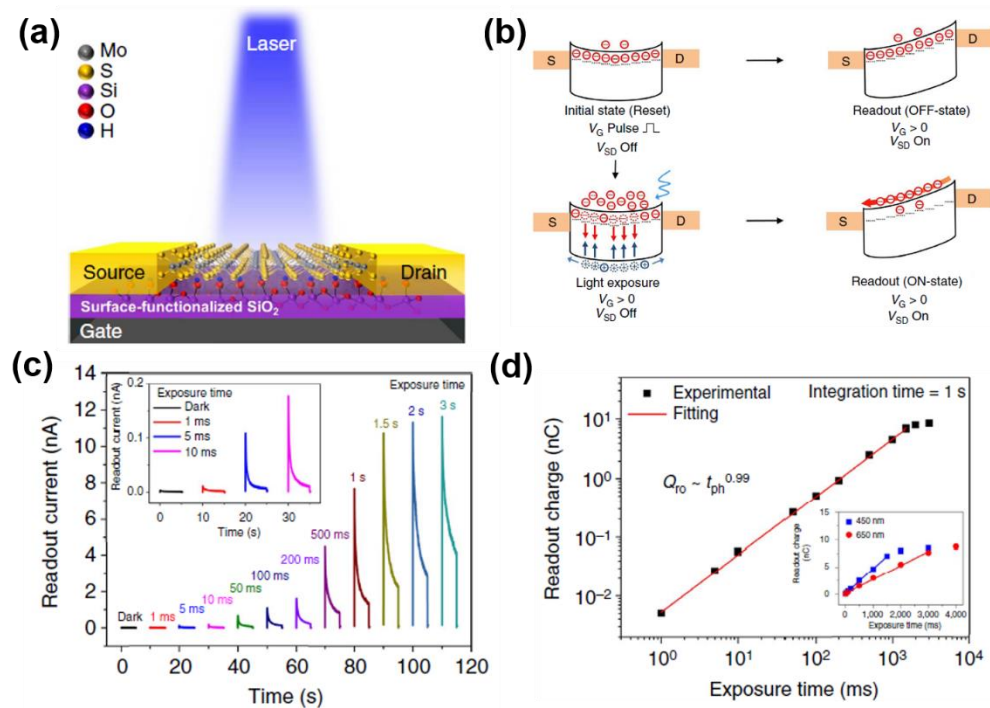


Figure 3.8. MoS₂ optoelectronic memory for image sensing application. (a) Device structure. (b) Switching mechanism. (c) The linear relationship between output current and illumination time. (d) Data retention properties.^[67]

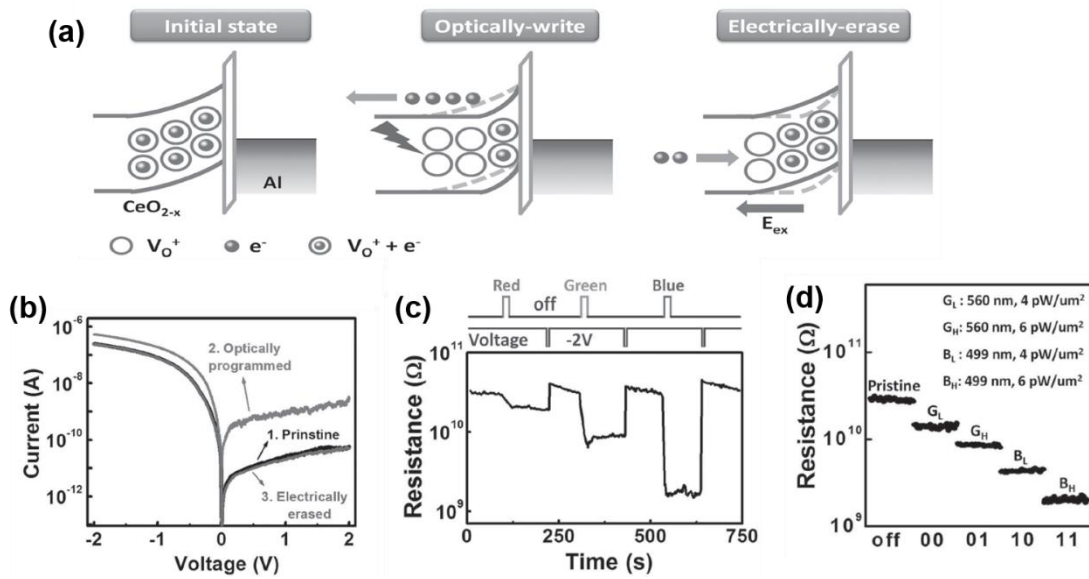


Figure 3.9. An optoelectronic memory with structure of ITO/CeO_{2-x}/AlO_y/Al. (a) Schematics of switching mechanism. (b) IV curves of optical programming and electrical erasing. (c) Wavelength-dependent resistance states. (d) Multi-level data storage by controlling the light intensity and wavelength. [68]

The introduction of optical control in RRAMs allows for the design of multifunctional memory device, such as multi-level storage, sensing and data processing. However, the slow operation speed in the optoelectronic memory is still a main issue and hinder the device from practical applications. The novel optoelectronic memories are still required to be explored with faster operation speed.

3.2 Low voltage, optoelectronic CH₃NH₃PbI_{3-x}Cl_x Memory with Integrated Sensing and Logic Operations

3.2.1. Motivation

Internet of things (IoT) has emerged as a technological revolution in the information explosion era. There are huge amount of interconnected devices coupled with sensors

(data capture), processors (data processing and analyzing), and embedded non-volatile memories (data storage). To better deliver the potential of IoT, multifunctional integrated devices with low power consumption are desired. From this point of view, non-volatile optoelectronic memory can be a possible choice for constructing a “smart sensor” for IoT application, which integrates the sensing, data storage and data processing functions into one device.

Optoelectronic memory can respond to both electrical stimuli and optical excitation, which enables to store and convert optical information as an electronic readout at low programming voltages.^[69-73] The optoelectronic memory also takes advantages of storing and processing transmitted optical signals over long-distance transmission with wide bandwidth, high-data-rate density, and low power consumption.^[74] Recently, researchers have demonstrated optoelectronic memory devices integrated with multi-level data storage, light-sensing, demodulating and arithmetic functions.^[69, 72, 73, 75-77] However, new optoelectronic materials, architectures and systems still remain to be developed and explored to reduce the cost, complexity and energy consumption.

Recently, organometal halide perovskites (OHPs) show excellent light absorption, long electron-hole diffusion length, ambipolar charge transport, unusual defect physics, and tunable band gap.^[78] A number of applications based on OHPs as light absorbing materials or semiconductor materials have been demonstrated, including solar cell^[79-81], photodetector^[82, 83], laser^[84], light emitting diode^[85-88], transistors^[89] and photovoltachormic supercapacitor^[90]. OHP-based electronic devices usually exhibit significant hysteresis, possibly caused by ferroelectricity, the formation and movement

of trap states or ion migration in the perovskites. More recently, researchers reported the perovskites for non-volatile resistive switching random access memory (RRAM).^[91-95] Till now, most of the research works based on the perovskite memory have been focused on the tri-iodide perovskite ($\text{CH}_3\text{NH}_3\text{PbI}_3$) system. It has been verified that I^- and MA^+ with low activation energies can migrate under external electric field.^[93] The formation and accumulation of defects can lead to resistive switching (RS) behavior in the perovskite memory devices.^[91, 95] It is also desirable to develop device architecture or counterpart materials, which enable the integration of both non-volatile information storage and processing in one device for the sake of high-performance integrated circuit design.

In this work, we design a non-volatile optoelectronic $\text{CH}_3\text{NH}_3\text{PbI}_{3-x}\text{Cl}_x$ memory device, in which the SET voltage can be controlled as low as 0.1 V with the assistance of light illumination. The $\text{CH}_3\text{NH}_3\text{PbI}_{3-x}\text{Cl}_x$ memory device can execute data-storage and logic operation in one memory device by using one electrical pulse and one optical pulse as the input signals. It can also detect the coincidence of electric and optical signal. This design provides possibilities in smart sensor design and IoT application.

3.2.2. Experiments

Perovskite Deposition and Perovskite Based ReRAM Fabrication The fluorine-doped tin oxide (FTO) coated glass substrates were cleaned with acetone, isopropanol and deionized water sequentially. The pre-cleaned substrates were then dried with nitrogen gas and further cleaned by UV-Ozone treatment. A one-step spin coating was

applied to the deposition of perovskite layer ($\text{CH}_3\text{NH}_3\text{PbI}_{3-x}\text{Cl}_x$) on the FTO glass in the N_2 glove box. The spin coating solution (34-wt%) for the perovskite layer was prepared by mixing methylammonium iodide (MAI) and lead chloride in N, N-dimethylformamide (DMF). The spin-coated perovskite thin film was annealed at 105 °C for 40 min. The dot-shaped Au electrodes with a thickness of 50 nm and diameter of 200 μm were deposited by e-beam evaporation through a shadow mask. The deposition rate was controlled at 0.3 Å /s and the final deposition temperature of the substrate was 40 °C.

Characterization of Perovskite Thin Film X-Ray diffraction (XRD) patterns of the perovskite film was determined by a Rigaku SmartLab X-ray diffractometer with a 2 theta range from 10 ° to 70 ° in a step of 0.01 °. Scanning electron microscopy (SEM) image was performed by Hitachi S-4800 field emission scanning microscope. The absorption spectra of perovskite film on quartz were examined using a UV-2250 Shimadzu UV-Vis spectrophotometer. Ultraviolet photoelectron spectra (UPS) and X-ray photoelectron spectroscopy (XPS) were carried out in a vacuum chamber ($<10^{-5}$ Torr). The excitation source for UPS is He-I UV source ($h\nu = 21.2$ eV). Before the UPS measurement of the perovskite sample, a conductive Au sample is used to calibrate the Fermi level. As to conduct the UPS of perovskite layer, a small voltage bias 5 V is applied to the sample when recording the secondary electron cutoff. A monochromatic Al K α (1486.6 eV photons) was used as the excitation source for XPS. A pass energy of 80 or 40 eV was employed for the wide and core-level narrow scan, respectively. The core-level signals were recorded at a photoelectron take-off angle of 90°. All

binding energies were calibrated referring to the C1s peak at 284.6 eV.

Characterization of Perovskite Based ReRAM The electrical characterizations of perovskite based ReRAM were measured using a Keithley 4200 in the vacuum probe station. FTO electrode was grounded and voltage was applied to the gold electrode. A white light LED with controllable power densities was used to illuminate the device from the FTO side. All the electrical switching measurements were conducted in the dark.

3.2.3. Results and Discussions

Figure 3.10 shows schematic structure of perovskite based memory in a configuration of Au/CH₃NH₃PbI_{3-x}Cl_x hybrid perovskite/fluorine-doped tin oxide (FTO) substrate, where the bottom FTO electrode is grounded, and the top Au electrode is connected to a voltage source for switching the memory cell. The perovskite thin film (CH₃NH₃PbI_{3-x}Cl_x) was deposited on FTO glass substrate by one-step solution method, and 50 nm Au was deposited on top of perovskite layer by e-beam evaporation. Figure 3.10b is the top-view scanning electron microscopy (SEM) image of the perovskite layer with a thickness of 270 nm, indicating a continuous perovskite film and good coverage on the FTO substrate. The (110), (220) and (330) peaks in the X-Ray diffraction (XRD) patterns confirms a crystallized perovskite thin film with the tetragonal phase, as shown in Figure 3.10c. To determine the elemental composition in the perovskite layer, we also conducted X-ray photoelectron spectroscopy (XPS) test (Figure 3.10d). A full spectrum scan shows negligible amount of Cl atoms in the perovskite film. A narrow

scan of Cl 2p core level is shown in the Figure 3.10e, where negligible signals corresponding to the Cl 2p_{3/2} and Cl 2p_{1/2} peaks are detected. It is consistent with previous works, in which the presence of Cl involves in the form of intermediate phase CH₃NH₃Cl that can easily escape during the annealing process and rare Cl exists in the final product.^[97] Although Cl content is negligible in the final perovskite thin film, Cl plays an important role in the film formation and crystallization and can influence the surface trap states in the film and the electronic properties ^[97-99].

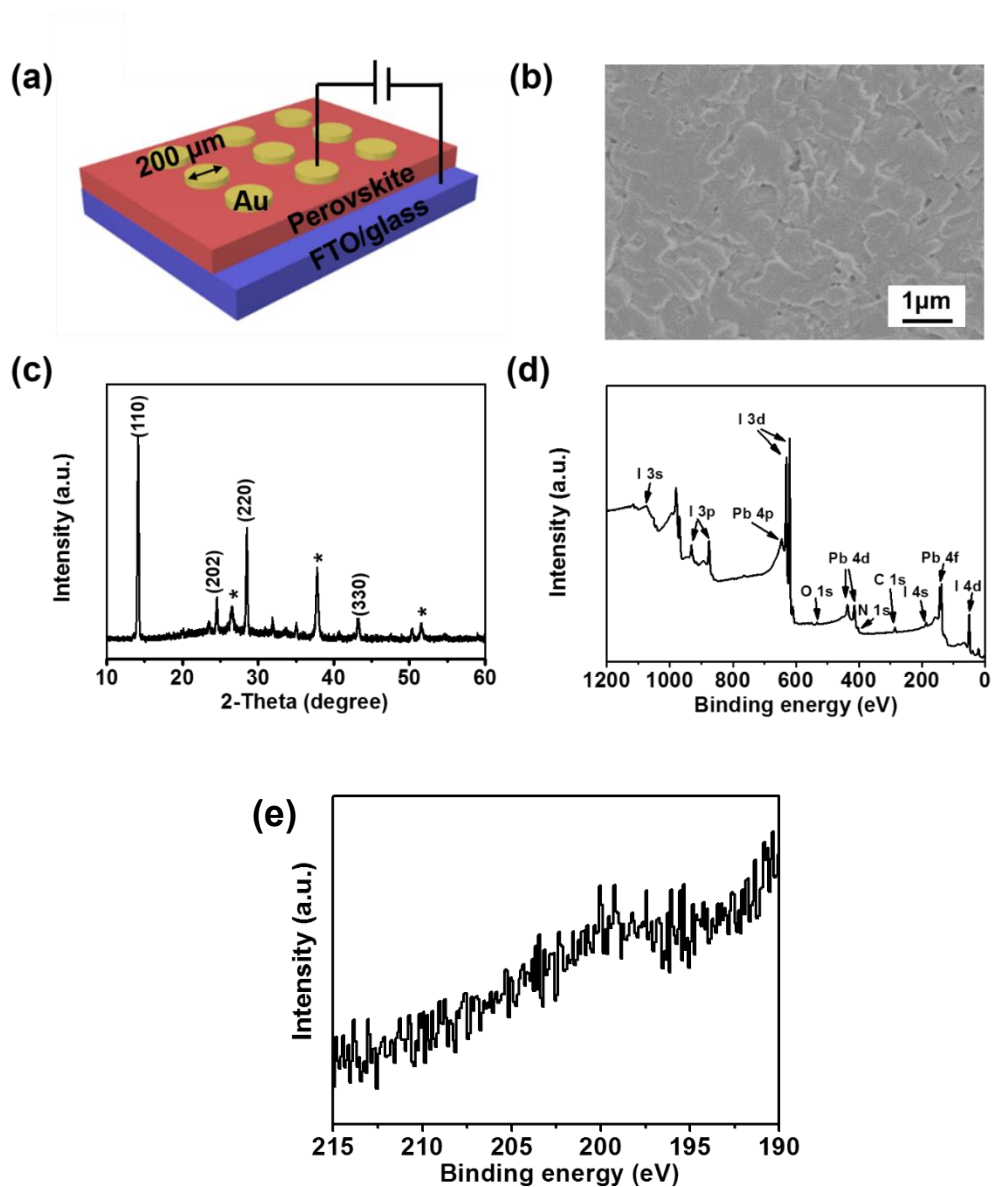


Figure 3.10. (a) Schematic device structure of perovskite based RRAM. (b) The as-prepared

perovskite thin film deposited on FTO glass substrate by one-step solution method, indicating good coverage of perovskite layer on the FTO glass. (c) XRD patterns of the as-prepared perovskite thin film. * represents the peaks of FTO glass. (d) XPS survey spectrum of the as-prepared perovskite thin film. (e) Narrow scan of Cl 2p core level and negligible signal of Cl 2p peak is detected. This suggests that most of the Cl escape with the form of intermediate phase.

It is worthy to be noted that we intentionally introduced the traps in the $\text{CH}_3\text{NH}_3\text{PbI}_{3-x}\text{Cl}_x$ film for the resistive switching memory device by using a low-concentrated precursor solution (34 wt. %). It has been suggested that the role of Cl in the precursor solution (>45 wt. %) can slow down the perovskite formation and crystallization, and drive the growth of well-defined grains in the perovskite film because of the modulated kinetics of the reactions by the formation of intermediate phases (*e.g.* $\text{CH}_3\text{NH}_3\text{Cl}$).^[97, 98] This evolution in perovskite morphology can further results in the reduced trap states and long diffusion length in the perovskite film.^[98-102] However, due to the less content of $\text{CH}_3\text{NH}_3\text{Cl}$ in the low-concentrated precursor solution, the duration of $\text{CH}_3\text{NH}_3\text{Cl}$ controlled crystallization is shortened and results in the under-developed film.^[97] This can introduce increased trap states during the film formation, and is a dominant characteristic in understanding the switching mechanism of our memory device.

We first examine the electrical characteristics of $\text{CH}_3\text{NH}_3\text{PbI}_{3-x}\text{Cl}_x$ based RRAM. Figure 3.11 shows the characteristics of electrical switching of $\text{CH}_3\text{NH}_3\text{PbI}_{3-x}\text{Cl}_x$ based memory. The memory device exhibits a bipolar and non-volatile resistive switching behavior (Figure 3.11a) under a DC voltage bias sweep ($0 \rightarrow 1.5 \rightarrow 0 \rightarrow -1.5 \rightarrow 0$ V). No forming process is required. As a positive voltage sweep is applied from 0 V to 1.5 V, the device is triggered from high resistance state (HRS) to low resistance state (LRS) at a positive voltage of 1.47 V. The RESET process occurs by applying a negative

voltage of -1.41 V. The ON/OFF ratio of the perovskite memory cell reaches 10^4 . Figure 3.11b and c demonstrate the retention characteristic and cyclic endurance test during 50 cycles, respectively. All of the above electrical tests are performed under a dark condition. Distributions of the average SET/RESET voltage of the devices in 17 batches are shown in Figure 3.11d. The devices fabricated in different batches exhibit reasonable variations with similar performance.

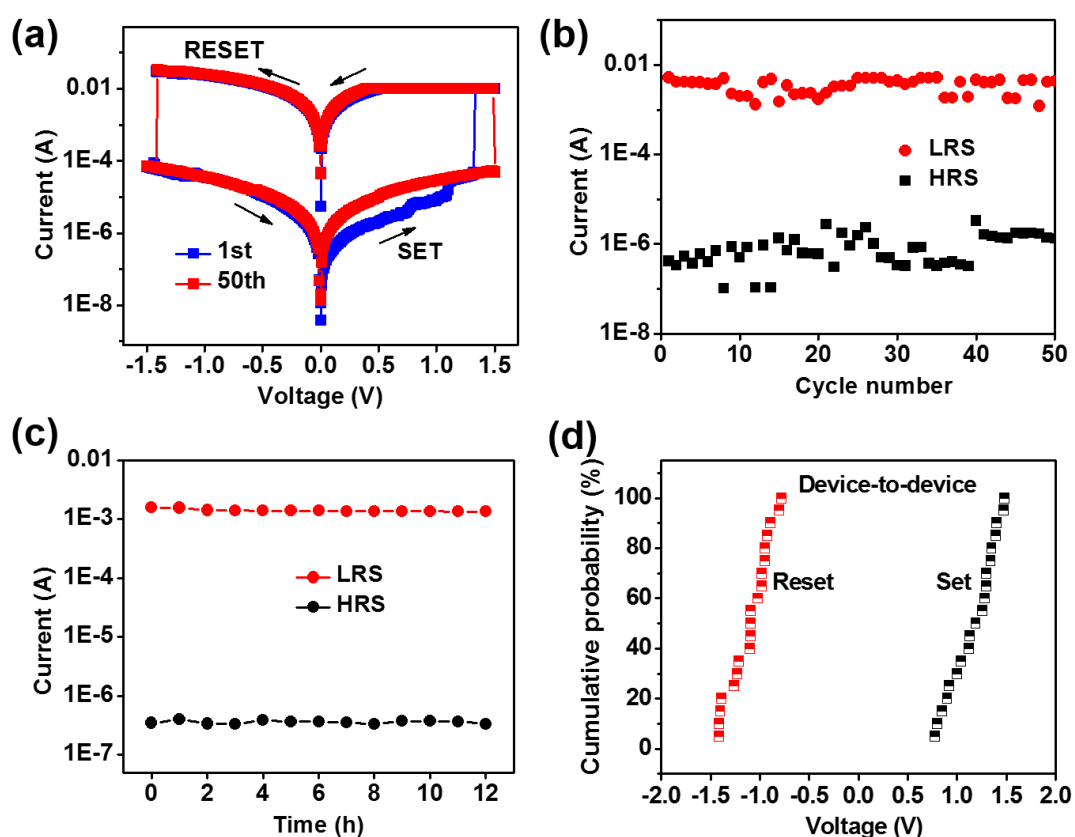


Figure 3.11. (a) The I-V characteristics of electrical switching behavior of perovskite based memory. (b) Cyclic tests for 50 cycles (c) Electrical reliability test for 12 h before and after electrical switching, showing no obvious degradation in HRS and LRS. (d) Cumulative probability plots for the SET and RESET voltages.

The unique light absorption characteristics of perovskite provide the possibilities in controlling the switching behavior and realizing more functions in $\text{CH}_3\text{NH}_3\text{PbI}_{3-x}\text{Cl}_x$ memory. Figure 3.12 depicts the current-voltage (I-V) characteristics of the photo-

assisted switching. During the SET process, the white light LED with a power density of 3.20 mW/cm^2 is adopted to illuminate the device from the FTO side, accompanying with the positive voltage sweep. It is noteworthy that the transition from HRS to LRS occurs at a SET voltage as low as 0.1 V , which is the lowest SET voltage compared with those perovskite based RRAM cells reported in existing literature. In these previous works, the SET voltages of perovskite based non-volatile RRAM under dark condition are 0.64 V [91], 0.8 V [92] and 2 V [96], respectively. After the SET process, the device can be electrically RESET under a dark condition at a voltage of -0.45 V . Distributions of the average SET/RESET voltage and HRS/LRS are plotted in Figure 3.13a and b, respectively, showing reasonably good memory characteristics. We also conducted endurance and retention measurements using pulse measurement mode, as shown in Figure 3.14a and b. The voltage pulse condition and light power density for SET process is 0.13 V for $100 \mu\text{s}$ and 3.2 mW/cm^2 , respectively. The voltage pulse for RESET process is -1.6 V for $250 \mu\text{s}$. The readout voltage is 0.05 V . Figure 3.14a depicts pulse switching endurance for two resistance states over 400 cycles. Both HRS and LRS can be retained up to 13 hours under dark and ambient environment, showing good retention compared with other perovskite-based memories (Figure 3.14b).^[91-96] The switching performance of our device is in stark contrast with the existing optoelectronic memories. In the previous optoelectronic memories reported, the memory devices can perform well through optical switching with light illumination. While there is no optical power supplied and under a dark condition, the electrical switching cannot exhibit comparable performances. For example, the optoelectronic memory with

ITO/CeO_{2-x}/Al_xO_y/Al structure can be switched optically with an ON/OFF ratio of 10³, whereas only an ON/OFF ratio of 10 is exhibited in the electrical switching under dark condition because of a different switching mechanism. [76] Similar phenomena have also been demonstrated in optoelectronic memories based on other materials, such as ZnO/SrTiO₃ [76] and Al₂O₃/SiO₂/Si [71]. In comparison, our device can exhibit similar ON/OFF ratio by electrical switching under the dark condition compared with the switching under light illumination, which can be more adaptive to various environments. We also examined the air-stability of the perovskite memory cells. The air-stability of perovskite material in ambient environment is an issue because of the exposure of hybrid perovskite to water can cause its decomposition. We conducted experiments of the device air-stability (Figure 3.15). The air-stability test of the device is conducted at the ambient environment with a humidity of 50~55 %. The device characteristics were extracted every day. Figure 3.15a and b show the degradation of electrical switching and optical switching, respectively. The devices exhibit slight degradation after 3 days and fail after 4 days at the ambient environment. The failure of the device can be attributed to the hydrolyzed perovskite in the presence of moisture in air.

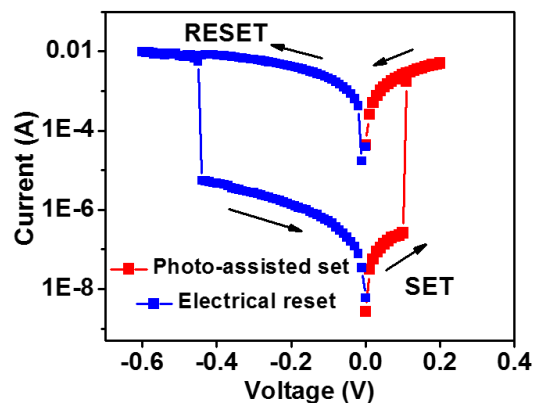


Figure 3.12. The I-V characteristics of low-voltage photo-assisted switching behavior of perovskite based memory. The SET process is conducted under the white light illumination with a power

density of 3.20 mW/cm^2 . The perovskite based memory then is RESET under the dark condition.

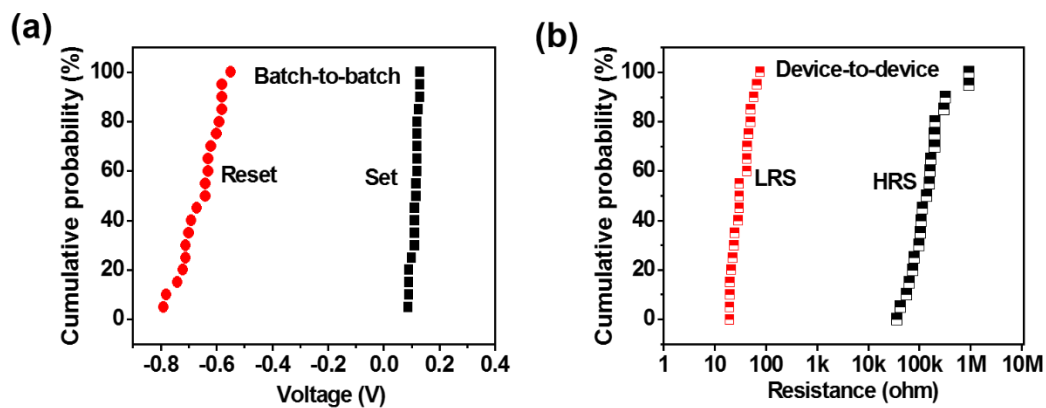


Figure 3.13. Distributions of the average SET/RESET voltage and HRS/LRS.

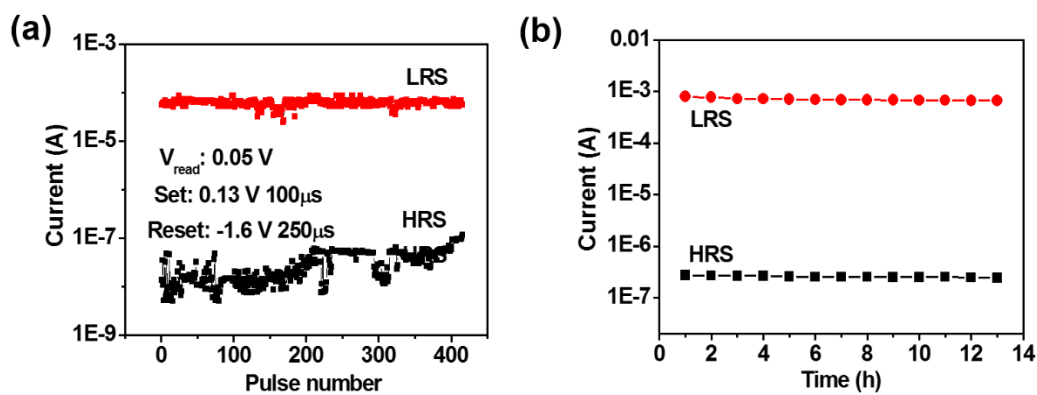


Figure 3.14. Pulse switching endurance and (d) retention test for two resistance states. The pulse condition for HRS is 0.13 V for 100 μs with white light illumination (3.20 mW/cm^2) and for LRS is -1.6 V for 250 μs . The readout voltage is 0.05 V.

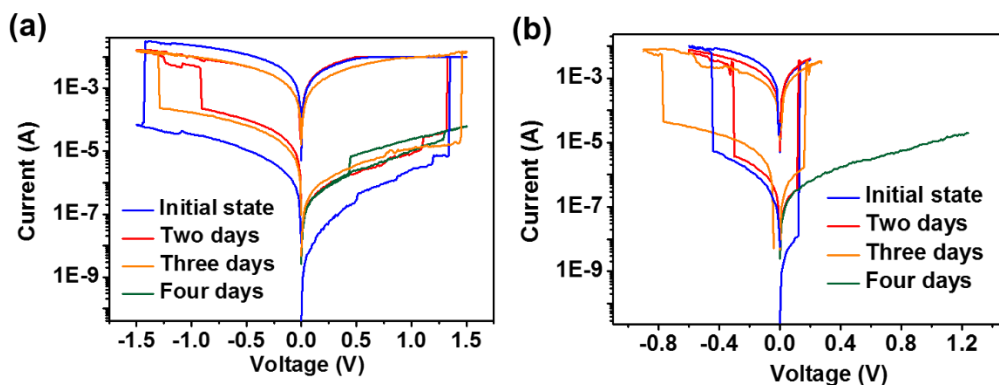


Figure 3.15. Stability tests of perovskite RRAM at the ambient environment with humidity of 50~55 %. (a) Electrical switching and (b) Optical switching.

Figure 3.16a and b present the photo-assisted switching characteristics. The SET voltage exhibits light-dependent characteristics, as shown in the Figure 3e. As the light intensity is increased from 0 to 3.20 mW/cm^2 , the SET voltage decreases from 1.47 V

to 0.1 V accordingly with the same compliance current of 10 mA. By combining voltage pulse and optical pulse, we can also obtain multiple non-volatile resistance states corresponding to different light intensities (Figure 3.16b). The SET processes of each resistance state are operated by one electrical pulse and one optical pulse. The voltage pulse used is 0.13 V 100 μ s for all set processes. The duration of optical pulse applied is 1 s and the readout voltage is 0.05 V. With the same voltage pulse, the resistance of memory cell is decreased as light intensity is increased. These light intensity-dependent characteristics can also be considered as behaviors of a sensor, in which the resistance switching behaves differently according to different levels of light intensities. Compared with the conventional photodetector, the light information can be recorded and retained in our device even after the removal of optical trigger.

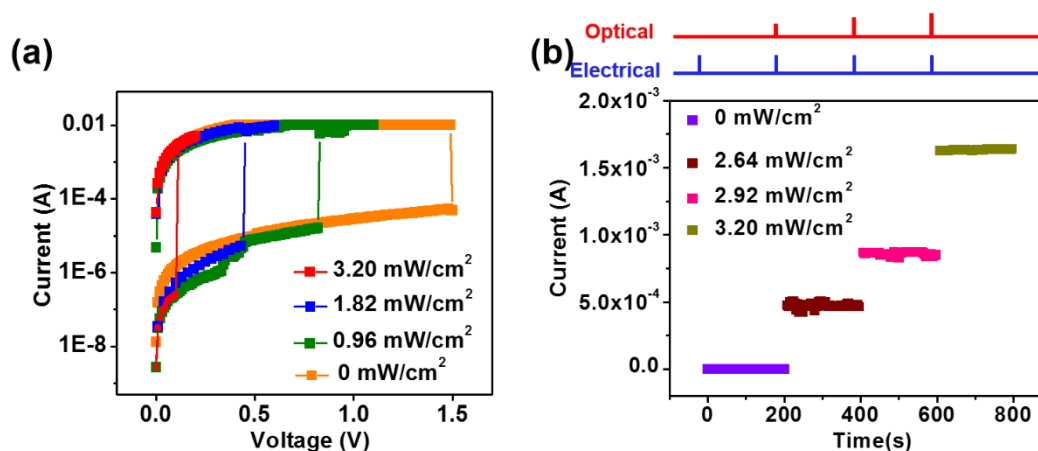


Figure 3.16. The SET processes under different light intensities. (f) Light-intensity controlled multiple resistance states. The voltage pulse for the set processes is 0.13 V for 100 μ s. The duration of optical pulses used is 1 s.

In order to better understanding the switching behavior and switching mechanism, firstly we conducted the ultraviolet electron microscopy (UPS) to examine the surface trap states and semiconductor type of the as-prepared perovskite thin film on the FTO glass, which plays an important role in determining the electronic properties of the

perovskite film. ^[103, 104] A He-I UV light source ($h\nu=21.2$ eV) is utilized to obtain the UPS spectra (Figure 3.17a and b). The binding energy is referred to the Fermi level. We extract the work function from the onset energy in the cut-off region in Figure 4a, which is approximately 4.37 eV. Figure 3.17b shows the spectrum near the valence band region, where the valence band maxima (VBM) is obtained at a binding energy of 1.32 eV. The band gap of perovskite thin film is determined to be 1.63 eV, according to the absorption spectrum in Figure 3.17c. Thus, the schematic band diagram of perovskite thin film can be sketched in the inset of Figure 3.17b, in which the Fermi level locates near to the conduction band. In addition, UPS has a high sensitivity to the intrinsic surface defects. A broad distribution of hole trap states is presented in the band gap above the valence energy. In previous studies, researchers also employed UPS technique to examine the surface trap states in the perovskite thin film, which are in consistent with our results ^[105, 106] These trap states can provide hole trapping centers at the perovskite/Au interface, which is essential to understand the switching behavior in the $\text{CH}_3\text{NH}_3\text{PbI}_{3-x}\text{Cl}_x$ memory device.

Secondly, we investigated the effect of device area on the resistance state. Figure 3.18a (electrical switching) and Figure 3.18b (photo-assisted switching) show the ON and OFF current of our perovskite memory devices with different device areas (the diameter of top electrode: 80 μm , 150 μm , and 300 μm). The readout voltage is 0.05 V and compliance current is controlled at 10 mA. The resistance increases with the decrease of device area. This is in stark contrast with the filament-based switching mechanism, where the resistance is typically independent on device area. According to

the above area-dependent results and UPS tests, we proposed an interface-based switching mechanism based on the injection/ejection of holes at the perovskite/Au interfacial hole trapping centers.

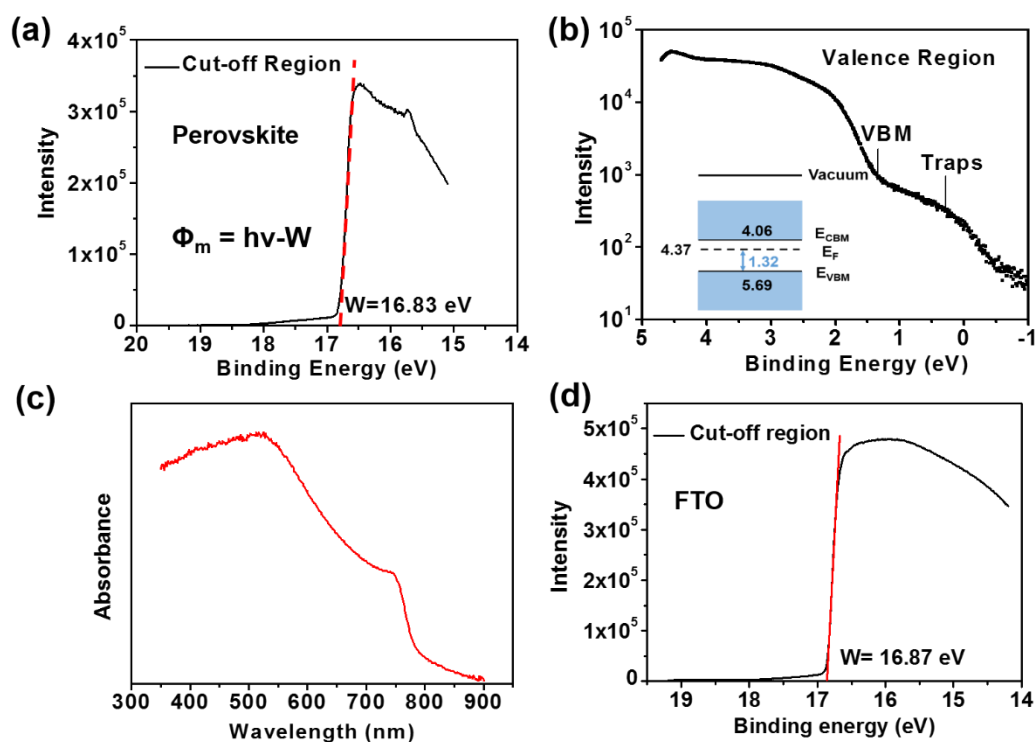


Figure 3.17. UPS spectra of perovskite thin film on FTO glass at (a) cut-off region and (b) valence band region obtained with $h\nu = 21.2$ eV. The binding energy is referred to the Fermi level. The work function is determined as 4.37 eV from the intercepts. A broad distribution of hole traps is observed above the valence band edge. The difference between valence band and Fermi level can be determined as 1.32 eV. (c) Absorbance spectrum of perovskite thin film on FTO glass and the bandgap obtained from the absorption edge is 1.63 eV. The band diagram of perovskite film is schematically illustrated in the inset of Figure 3.17. (d) The cut-off region in the UPS spectrum of FTO glass. The work function of FTO is calculated as 4.33 eV, which is considered to form an ohmic contact with perovskite layer.

Figure 3.18c and d depict the proposed mechanisms of electrical switching of the perovskite memory cell. According to the UPS characterization results, the work function of perovskite is 4.37 eV and the interfacial hole traps are located close to valence bands. At the initial state (HRS), there is a Schottky barrier formed at the perovskite/Au interface because of the difference in Fermi level between perovskite

(4.37 eV) and Au (5.0 eV). The work function of the FTO glass is extracted as 4.33 eV from the UPS, as shown in Figure 3.17d. Thus, we can regard the contact between FTO and perovskite as Ohmic contact because of their similar work functions of 4.33 eV (FTO) and 4.37 eV ($\text{CH}_3\text{NH}_3\text{PbI}_{3-x}\text{Cl}_x$), respectively.

As a positive voltage connected to Au electrode is increased to 1.5 V, the Schottky barrier is decreased. The holes can inject from the Au electrode across the perovskite/Au interface, and fill into the interfacial hole trapping centers. With the increase of hole concentration at the interface, the Fermi level of perovskite shift towards to the valence band, leading to a lowered Schottky barrier. The contact between perovskite and Au electrode then becomes a quasi Ohmic contact, corresponding to LRS. Hybrid perovskite has been reported previously that can be heavily doped in low concentration dopants, which results in the obvious change in Fermi level and Schottky barrier.^[107-109] Since the hole trap states have broad energy distribution between the Fermi level and valence band maximum (Figure 3.17b), the injected holes can be stably filled in the deep level defects, and the LRS can be retained even after the removal of electrical bias.^[110-113] The RESET process happens as a negative voltage bias is applied to the Au electrode. Holes are retracted from the trapped states in perovskite to the Au electrode. The Schottky barrier becomes higher and recovers to the original state (HRS).

For the photo-assisted low voltage switching (Figure 3.18d), under the light illumination, a large amount of electron-hole pairs are generated in the perovskite that can be separated with a small bias of 0.1 V. The hole trap states can trap photo-generated holes, shifting the Fermi level of perovskite towards valence band and leaving a

lowered Schottky barrier. In the meantime, more holes from Au electrode can also inject into the hole trap states in the perovskite, further lowering the Schottky barrier. A quasi Ohmic contact can be formed, corresponding to LRS. Thus, with the light illumination, the SET voltage of the device can be controlled as low as 0.1 V, and the energy consumption of the memory device can also be reduced in this photo-assisted switching. The SET voltage also exhibits the light-intensity dependent characteristics. As the light intensity decreases, less amount of photo-induced charge carriers are generated, which requires a larger voltage to drive the injection of holes. By combining voltage pulse and optical pulse, multiple resistance states can be obtained. With the same voltage pulse (0.13 V, 100 μ s) and higher light intensity, the number of filled hole traps is increased, resulting in decreased Schottky barrier and resistance. The RESET process is similar to that of the electrical switching as stated above.

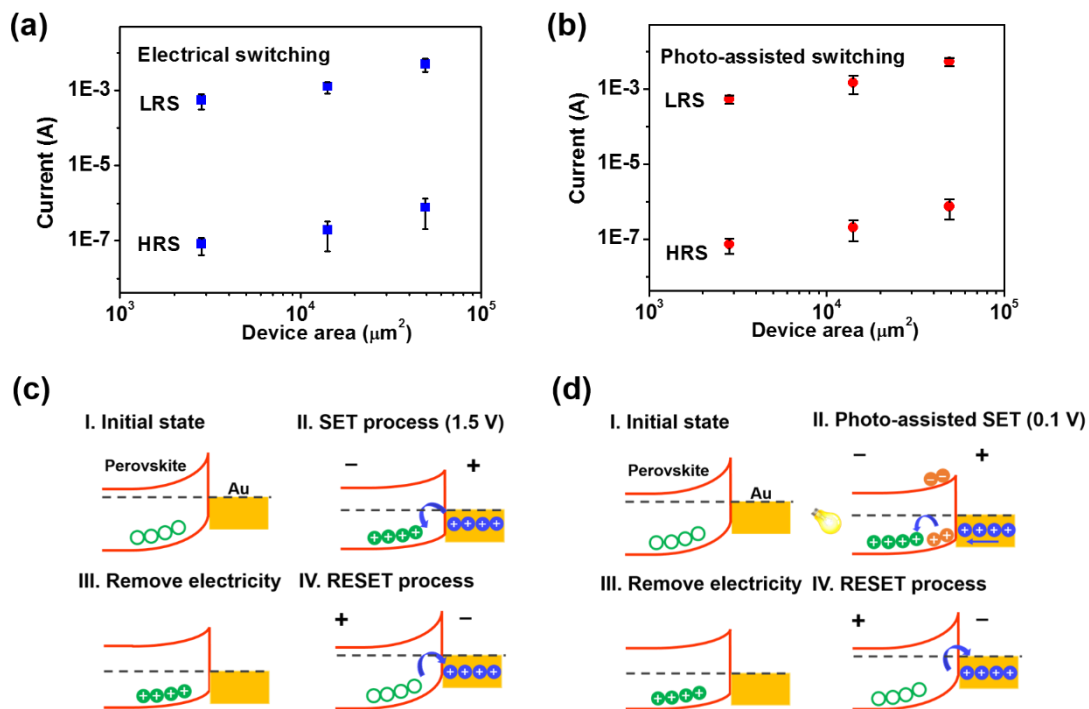


Figure 3.18. Variation of resistances at ON and OFF states of perovskite memory devices with different effective areas for (a) electrical switching and (b) photo-assisted switching. (c) electrical

switching and (d) photo-assisted switching mechanism including four states: I. initial state corresponding to HRS: hole trapping centers locate at the perovskite surface; II. SET process: hole trap states are filled, shifting the Fermi level to the valence band; III. remove light electricity: a lowered barrier and quasi ohmic contact are resulted corresponding to LRS. IV. electrical reset: holes are extracted from the trap states and a transition from LRS to HRS occurs.

In addition to the sensing and memory functions, the use of both optical and electrical pulses also enables the device to operate with the functions of both data storage and non-volatile logic operation. Here we adopt the light pulses and electrical pulses as the input signals to realize typically logic operation, including AND ($Y=AB$) and OR ($Y=A+B$). Figure 3.19a demonstrates a nonvolatile AND logic operation. To correctly perform a logic operation, it is critical to select the light intensity and pulse voltage. For the input signals, we defined the light pulse ($>3.2 \text{ mW/cm}^2$, 1 s) as logic '1', light pulse ($<0.3 \text{ mW/cm}^2$, 1 s) as logic '0', electrical pulse (0.13 V, 100 μs) as logic '1' and electrical pulse (0.01 V, 100 μs) as logic '0'. For the output, the HRS and LRS are defined as logic '1' and logic '0', respectively. The output currents are read before and after the input pulses with a read voltage of 0.05 V. Using an electrical pulse with a small voltage of 0.01 V, even combining a light pulse with intensity of $>3.2 \text{ mW/cm}^2$, the memory device cannot be switched to LRS. This can be understood that the voltage of 0.01 V is insufficient to separate the photo-generated carriers or drive the charge carriers into hole traps. Similarly, the use of a light pulse with low power intensity of $<0.3 \text{ mW/cm}^2$ and an electrical pulse of 0.1 V is not enough to set the device to LRS, because of the very small amount of photo-generated charge carriers produced. Only in the case that the input electrical pulse (0.1 V, 1 s) and optical pulse (3.2 mW/cm^2 , 1 s) can switch the device to LRS corresponding to logic '1'. The output state of LRS can be retained over 13 hours.

To fulfill an OR logic operation, we also appropriately select the parameters of the input pulses. Figure 3.19b show an OR logic operation. Before each operation, the device is reset to HRS. In the OR logic operation, we define the light pulse (3.2 mW/cm^2 , 1 s) as logic ‘1’, light pulse (0.5 mW/cm^2 , 1 s) as logic ‘0’, electrical pulse (2 V, 250 μs) as logic ‘1’ and electrical pulse (0.13 V, 100 μs) as logic ‘0’. The output currents are read before and after the input pulses with a read voltage of 0.05 V. As an electrical pulse of 0.13 V and an optical pulse of 0.5 mW/cm^2 are input, the input energy cannot drive the SET process, and the output is considered as logic ‘0’. The inputs of an electrical pulse of 0.1 V (logic “0”) and a light pulse of 3.2 mW/cm^2 (logic “1”), and inputs of an electrical pulse of 2 V (logic “1”) and a light pulse of 0.5 mW/cm^2 (logic “0”) can both switch the device to LRS (logic “1”). The output states can be stably retained and stored, which suggests a non-volatile logic operation.

We also demonstrate another function of coincidence event detection in our device, which can detect the simultaneity the several input signals and plays important roles in the neuroscience and neuromorphic computing. ^[113-115] Figure 3.19c shows the operation of the perovskite memory as a 3-pulse coincidence detector. In this system, three input signals are defined as optical pulse (A) with a power intensity of 3.2 mW/cm^2 , electrical pulse (B) applied to the top electrode (0.05 V) and electrical pulse (C) applied to the bottom electrode (-0.05 V). The duration of three pulses are 1 s. The output current Y can represent if one of the input signal is out of phase with the rest signals. It can be noticed that only in the case the three pulses appear simultaneously, there shows the output current of 1.4 mA, corresponding to the LRS of the memory

device.

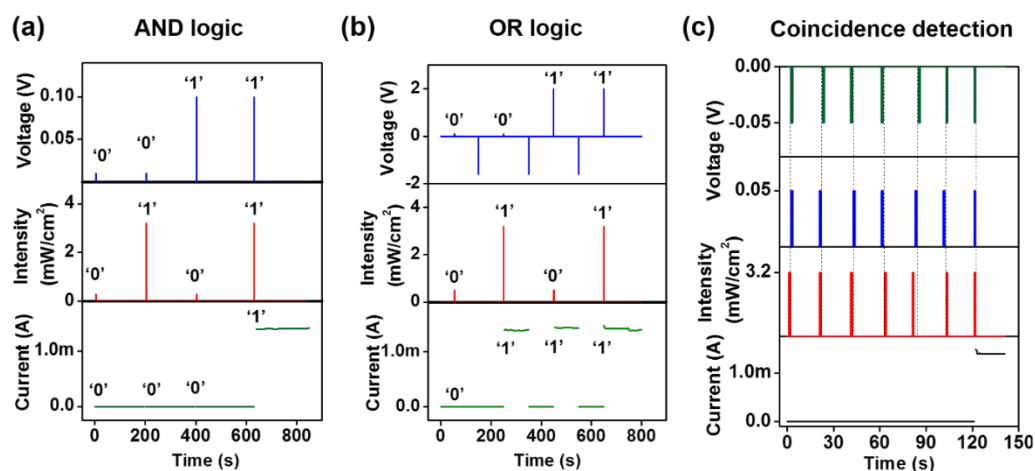


Figure 3.19. Demonstrations of logic operations and coincidence detection of the perovskite based memory. (a) A demonstration of AND logical operation. We defined the light pulse ($>3.2 \text{ mW/cm}^2$, 1 s) as logic '1', light pulse ($<0.3 \text{ mW/cm}^2$, 1 s) as logic '0', electrical pulse (0.13 V, 100 μs) as logic '1' and electrical pulse (0.01 V, 100 μs) as logic '0'. (b) A demonstration of OR logical operation. we define the light pulse (3.2 mW/cm^2 , 1 s) as logic '1', light pulse (0.5 mW/cm^2 , 1 s) as logic '0', electrical pulse (2 V, 250 μs) as logic '1' and electrical pulse (0.1 V, 100 μs) as logic '0'. HRS and LRS are defined as logic '1' and logic '0' in both AND and OR logic operations. (c) A demonstration of 3-pulse coincidence detection. Three input pulses are optical pulse (3.2 mW/cm^2 , 1s), electrical pulse applied to the top electrode (0.05 V, 1s) and electrical pulse applied to the bottom electrode (-0.05 V, 1s). The output current Y can represent the coincidence of the three input pulses. Only in the case that the three pulses appear coincidentally, there shows an output current corresponding to the LRS of the memory device.

3.2.4. Summary

In summary, we design and fabricate $\text{CH}_3\text{NH}_3\text{PbI}_{3-x}\text{Cl}_x$ perovskite based optoelectronic memory device. By utilizing the excellent light absorption ability of the perovskite layer, the SET voltage of the memory device can be decreased from 1.5 V to 0.1 V with the assistance of light illumination. It can reduce the power consumption in the device. According to the switching behavior, we proposed a possible trap-mediated switching mechanism based on the existence of hole trapping centers at the $\text{CH}_3\text{NH}_3\text{PbI}_{3-x}\text{Cl}_x$ perovskite surface. The possible switching mechanism may provide

more possibilities in the perovskite based memory device design. By combining the electrical input and optical input and correctly select the input pulses, the perovskite RRAM can execute not only data storage but also optical sensing and logic operation.

References

1. Li, Y., S. Long, Q. Liu, H. Lü, S. Liu, and M. Liu, *Chin. Sci. Bull.* **2011**, 56, 3072.
2. Wong, H.-S.P., H.-Y. Lee, S. Yu, Y.-S. Chen, Y. Wu, P.-S. Chen, B. Lee, F.T. Chen, and M.-J. Tsai, *Proceedings of the IEEE* **2012**, 100, 1951.
3. Seo, S., M. Lee, D. Seo, E. Jeoung, D.-S. Suh, Y. Joung, I. Yoo, I. Hwang, S. Kim, and I. Byun, *Appl. Phys. Lett.* **2004**, 85, 5655.
4. Kim, K.M., B.J. Choi, and C.S. Hwang, *Appl. Phys. Lett.* **2007**, 90, 242906.
5. Kim, Y.-M. and J.-S. Lee, *J. Appl. Phys.* **2008**, 104, 114115.
6. Jeong, D.S., H. Schroeder, and R. Waser, *Electrochem. Solid-State Lett.* **2007**, 10, G51.
7. Ye, C., C. Zhan, T.-M. Tsai, K.-C. Chang, M.-C. Chen, T.-C. Chang, T. Deng, and H. Wang, *Applied Physics Express* **2014**, 7, 034101.
8. Hwang, I., M.-J. Lee, G.-H. Buh, J. Bae, J. Choi, J.-S. Kim, S. Hong, Y.S. Kim, I.-S. Byun, and S.-W. Lee, *Appl. Phys. Lett.* **2010**, 97, 052106.
9. Russo, U., D. Ielmini, C. Cagli, A. Lacaíta, S. Spiga, C. Wiemer, M. Perego, and M. Fanciulli. *Conductive-filament switching analysis and self-accelerated thermal dissolution model for reset in NiO-based RRAM*. in *Electron Devices Meeting, 2007. IEDM 2007. IEEE International*. 2007. IEEE.
10. Yu, S. and H.-S.P. Wong, *IEEE Electron Device Letters* **2010**, 31, 1455.
11. Tsai, Y.-T., T.-C. Chang, C.-C. Lin, L.-S. Chiang, S.-C. Chen, S.M. Sze, and T.-Y. Tseng, *ECS Transactions* **2011**, 41, 475.
12. Zhou, Q. and J. Zhai, *Appl. Surf. Sci.* **2013**, 284, 644.
13. Wang, S.-Y., D.-Y. Lee, T.-Y. Tseng, and C.-Y. Lin, *Appl. Phys. Lett.* **2009**, 95, 112904.
14. Lv, H., M. Wang, H. Wan, Y. Song, W. Luo, P. Zhou, T. Tang, Y. Lin, R. Huang, and S. Song, *Appl. Phys. Lett.* **2009**, 94, 213502.
15. Goux, L., P. Czarnecki, Y.Y. Chen, L. Pantisano, X. Wang, R. Degraeve, B. Govoreanu, M. Jurczak, D. Wouters, and L. Altimime, *Appl. Phys. Lett.* **2010**, 97, 243509.
16. Lee, H., P. Chen, T. Wu, Y. Chen, C. Wang, P. Tzeng, C. Lin, F. Chen, C. Lien, and M.-J. Tsai. *Low power and high speed bipolar switching with a thin reactive Ti buffer layer in robust HfO₂ based RRAM*. in *Electron Devices Meeting, 2008. IEDM 2008. IEEE International*. 2008. IEEE.
17. Wu, Y., B. Lee, and H.-S.P. Wong. *Ultra-low power Al₂O₃-based RRAM with 1 μ A reset current*. in *VLSI Technology Systems and Applications (VLSI-TSA), 2010 International Symposium on*. 2010. IEEE.
18. Liang, J. and H.-S.P. Wong, *IEEE Transactions on Electron Devices* **2010**, 57, 2531.
19. Baek, I., M. Lee, S. Seo, M. Lee, D. Seo, D.-S. Suh, J. Park, S. Park, H. Kim, and I. Yoo. *Highly scalable nonvolatile resistive memory using simple binary oxide driven by asymmetric unipolar voltage pulses*. in *Electron Devices Meeting, 2004. IEDM Technical Digest. IEEE International*. 2004. IEEE.
20. Tsunoda, K., K. Kinoshita, H. Noshiro, Y. Yamazaki, T. Iizuka, Y. Ito, A. Takahashi, A. Okano, Y. Sato, and T. Fukano. *Low power and high speed switching of Ti-doped NiO ReRAM under the unipolar voltage source of less than 3 V*. in *Electron Devices Meeting, 2007. IEDM 2007. IEEE International*. 2007. IEEE.
21. Lee, M.-J., Y. Park, B.-S. Kang, S.-E. Ahn, C. Lee, K. Kim, W. Xianyu, G. Stefanovich, J.-H. Lee, and S.-J. Chung. *2-stack 1D-1R cross-point structure with oxide diodes as switch elements*

- for high density resistance RAM applications*. in *Electron Devices Meeting, 2007. IEDM 2007. IEEE International*. 2007. IEEE.
22. Lee, M.-J., C.B. Lee, D. Lee, S.R. Lee, M. Chang, J.H. Hur, Y.-B. Kim, C.-J. Kim, D.H. Seo, and S. Seo, *Nat. Mater.* **2011**, 10, 625.
 23. Tsai, T.-M., K.-C. Chang, T.-C. Chang, Y.-E. Syu, S.-L. Chuang, G.-W. Chang, G.-R. Liu, M.-C. Chen, H.-C. Huang, and S.-K. Liu, *IEEE Electron Device Letters* **2012**, 33, 1696.
 24. Waser, R., R. Dittmann, G. Staikov, and K. Szot, *Adv. Mater.* **2009**, 21, 2632.
 25. Sawa, A., *Mater. Today* **2008**, 11, 28.
 26. Kim, C.J. and I.-W. Chen, *Thin Solid Films* **2006**, 515, 2726.
 27. Yang, R., X. Li, W. Yu, X. Gao, D. Shang, X. Liu, X. Cao, Q. Wang, and L. Chen, *Appl. Phys. Lett.* **2009**, 95, 072105.
 28. Chang, K.-C., T.-M. Tsai, T.-C. Chang, K.-H. Chen, R. Zhang, Z.-Y. Wang, J.-H. Chen, T.-F. Young, M.-C. Chen, and T.-J. Chu, *IEEE Electron Device Letters* **2014**, 35, 530.
 29. Gao, S., C. Song, C. Chen, F. Zeng, and F. Pan, *The Journal of Physical Chemistry C* **2012**, 116, 17955.
 30. Sun, J., Q. Liu, H. Xie, X. Wu, F. Xu, T. Xu, S. Long, H. Lv, Y. Li, and L. Sun, *Appl. Phys. Lett.* **2013**, 102, 053502.
 31. Ling, Y., Y. Lei, Q. Zhang, L. Chen, Q. Song, and Z. Xiong, *Appl. Phys. Lett.* **2015**, 107, 108_1.
 32. Gao, S., F. Zeng, C. Chen, G. Tang, Y. Lin, Z. Zheng, C. Song, and F. Pan, *Nanotechnology* **2013**, 24, 335201.
 33. Zhu, X., W. Su, Y. Liu, B. Hu, L. Pan, W. Lu, J. Zhang, and R.W. Li, *Adv. Mater.* **2012**, 24, 3941.
 34. Peng, P., D. Xie, Y. Yang, Y. Zang, X. Gao, C. Zhou, T. Feng, H. Tian, T. Ren, and X. Zhang, *J. Appl. Phys.* **2012**, 111, 084501.
 35. Bratsch, S.G., *J. Phys. Chem. Ref. Data* **1989**, 18, 1.
 36. Speight, J.G., *Lange's handbook of chemistry*. Vol. 1. 2005: McGraw-Hill New York.
 37. Liaw, C., M. Kund, D. Schmitt-Landsiedel, and I. Ruge. *The conductive bridging random access memory (CBRAM): a non-volatile multi-level memory technology*. in *Solid State Device Research Conference, 2007. ESSDERC 2007. 37th European*. 2007. IEEE.
 38. Kozicki, M.N., M. Balakrishnan, C. Gopalan, C. Ratnakumar, and M. Mitkova. *Programmable metallization cell memory based on Ag-Ge-S and Cu-Ge-S solid electrolytes*. in *Non-Volatile Memory Technology Symposium, 2005*. 2005. IEEE.
 39. Hasegawa, T., K. Terabe, T. Tsuruoka, and M. Aono, *Adv. Mater.* **2012**, 24, 252.
 40. Rahaman, S., S. Maikap, H. Chiu, C.-H. Lin, T.-Y. Wu, Y.-S. Chen, P.-J. Tzeng, F. Chen, M.-J. Kao, and M.-J. Tsai. *Low power operation of resistive switching memory device using novel W/Ge0.4Se0.6/Cu/Al structure*. in *Memory Workshop, 2009. IMW'09. IEEE International*. 2009. IEEE.
 41. Jameson, J., P. Blanchard, C. Cheng, J. Dinh, A. Gallo, V. Gopalakrishnan, C. Gopalan, B. Guichet, S. Hsu, and D. Kamalanathan. *Conductive-bridge memory (CBRAM) with excellent high-temperature retention*. in *Electron Devices Meeting (IEDM), 2013 IEEE International*. 2013. IEEE.
 42. Vianello, E., G. Molas, F. Longnos, P. Blaise, E. Souchier, C. Cagli, G. Palma, J. Guy, M. Bernard, and M. Reyboz. *Sb-doped GeS₂ as performance and reliability booster in conductive bridge RAM*. in *Electron Devices Meeting (IEDM), 2012 IEEE International*. 2012. IEEE.
 43. Kund, M., G. Beitel, C.-U. Pinnow, T. Rohr, J. Schumann, R. Symanczyk, K. Ufert, and G.

- Muller. *Conductive bridging RAM (CBRAM): An emerging non-volatile memory technology scalable to sub 20nm*. in *Electron Devices Meeting, 2005. IEDM Technical Digest. IEEE International*. 2005. IEEE.
44. Schindler, C., S.C.P. Thermadam, R. Waser, and M.N. Kozicki, *IEEE Transactions on Electron Devices* **2007**, 54, 2762.
 45. Rahaman, S., S. Maikap, W. Chen, H. Lee, F. Chen, M. Kao, and M. Tsai, *Appl. Phys. Lett.* **2012**, 101, 073106.
 46. Banno, N., T. Sakamoto, N. Iguchi, H. Sunamura, K. Terabe, T. Hasegawa, and M. Aono, *IEEE Transactions on Electron Devices* **2008**, 55, 3283.
 47. Li, Y., S. Long, M. Zhang, Q. Liu, L. Shao, S. Zhang, Y. Wang, Q. Zuo, S. Liu, and M. Liu, *IEEE Electron Device Letters* **2010**, 31, 117.
 48. Maikap, S., S. Rahaman, T. Wu, F. Chen, M. Kao, and M. Tsai. *Low current (5 pA) resistive switching memory using high- κ Ta₂O₅ solid electrolyte*. in *The 39th European Solid-State Device Research Conference and the 35th European Solid-state Circuits Conference (ESSDERC/ESSCIRC)*. 2009.
 49. Liu, Q., S. Long, H. Lv, W. Wang, J. Niu, Z. Huo, J. Chen, and M. Liu, *ACS nano* **2010**, 4, 6162.
 50. Yoon, J., H. Choi, D. Lee, J.-B. Park, J. Lee, D.-J. Seong, Y. Ju, M. Chang, S. Jung, and H. Hwang, *IEEE Electron Device Letters* **2009**, 30, 457.
 51. Aratani, K., K. Ohba, T. Mizuguchi, S. Yasuda, T. Shiimoto, T. Tsushima, T. Sone, K. Endo, A. Kouchiyama, and S. Sasaki. *A novel resistance memory with high scalability and nanosecond switching*. in *Electron Devices Meeting, 2007. IEDM 2007. IEEE International*. 2007. IEEE.
 52. Rahaman, S., S. Maikap, W. Chen, H. Lee, F. Chen, T. Tien, and M. Tsai, *J. Appl. Phys.* **2012**, 111, 063710.
 53. Rahaman, S.Z., S. Maikap, T.-C. Tien, H.-Y. Lee, W.-S. Chen, F.T. Chen, M.-J. Kao, and M.-J. Tsai, *Nanoscale research letters* **2012**, 7, 345.
 54. Belmonte, A., W. Kim, B. Chan, N. Heylen, A. Fantini, M. Houssa, M. Jureczak, and L. Goux. *90nm WAl₂O₃/TiW/Cu 1T1R CBRAM cell showing low-power, fast and disturb-free operation*. in *Memory Workshop (IMW), 2013 5th IEEE International*. 2013. IEEE.
 55. Wang, Y., X. Shi, X. Lai, Z. Gao, L. Liu, Y. Wang, W. Zhu, C. Meng, and L. Zhang, *Appl. Phys. Lett.* **2016**, 108, 192102.
 56. Yan, Z. and J.-M. Liu, *Scientific reports* **2013**, 3.
 57. Zou, X., H.G. Ong, L. You, W. Chen, H. Ding, H. Funakubo, L. Chen, and J. Wang, *AIP Advances* **2012**, 2, 032166.
 58. Yang, Y., F. Pan, F. Zeng, and M. Liu, *J. Appl. Phys.* **2009**, 106, 123705.
 59. Bozano, L., B. Kean, V. Deline, J. Salem, and J. Scott, *Appl. Phys. Lett.* **2004**, 84, 607.
 60. Dimitrakopoulos, C.D. and P.R. Malenfant, *Adv. Mater.* **2002**, 14, 99.
 61. Kim, T.W., Y. Yang, F. Li, and W.L. Kwan, *NPG Asia Materials* **2012**, 4, e18.
 62. Hwang, S.K., J.M. Lee, S. Kim, J.S. Park, H.I. Park, C.W. Ahn, K.J. Lee, T. Lee, and S.O. Kim, *Nano Lett.* **2012**, 12, 2217.
 63. Beck, A., J. Bednorz, C. Gerber, C. Rossel, and D. Widmer, *Appl. Phys. Lett.* **2000**, 77, 139.
 64. Park, J., S. Lee, J. Lee, and K. Yong, *Adv. Mater.* **2013**, 25, 6423.
 65. Bera, A., H. Peng, J. Lourembam, Y. Shen, X.W. Sun, and T. Wu, *Adv. Funct. Mater.* **2013**, 23, 4977.
 66. Lee, D., E. Hwang, Y. Lee, Y. Choi, J.S. Kim, S. Lee, and J.H. Cho, *Adv. Mater.* **2016**, 28, 9196.

67. Lee, J., S. Pak, Y.-W. Lee, Y. Cho, J. Hong, P. Giraud, H.S. Shin, S.M. Morris, J.I. Sohn, and S. Cha, *Nat. Commun.* **2017**, *8*, 14734.
68. Tan, H., G. Liu, X. Zhu, H. Yang, B. Chen, X. Chen, J. Shang, W.D. Lu, Y. Wu, and R.W. Li, *Adv. Mater.* **2015**, *27*, 2797.
69. A. Lipatov, P. Sharma, A. Gruverman, A. Sinitskii, *ACS nano* **2015**, *9*, 8089.
70. A. Bera, H. Peng, J. Lourembam, Y. Shen, X. W. Sun, T. Wu, *Adv. Funct. Mater.* 2013, *23*, 4977.
71. M. Ungureanu, R. Zazpe, F. Golmar, P. Stoliar, R. Llopis, F. Casanova, L. E. Hueso, *Adv. Mater.* 2012, *24*, 2496.
71. J. Lee, S. Pak, Y.-W. Lee, Y. Cho, J. Hong, P. Giraud, H. S. Shin, S. M. Morris, J. I. Sohn, S. Cha, *Nat. Commun.* 2017, *8*, 14734.
73. K. Roy, M. Padmanabhan, S. Goswami, T. P. Sai, G. Ramalingam, S. Raghavan, A. Ghosh, *Nat. Nanotech.* 2013, *8*, 826.
74. M. J. Kobrinsky, B. A. Block, J.-F. Zheng, B. C. Barnett, E. Mohammed, M. Reshotko, F. Robertson, S. List, I. Young, K. Cadien, *Intel Technology Journal* 2004, *8*.
75. M. S. Choi, G.-H. Lee, Y.-J. Yu, D.-Y. Lee, S. H. Lee, P. Kim, J. Hone, W. J. Yoo, *Nat. Commun.* 2013, *4*, 1624.
76. H. Tan, G. Liu, X. Zhu, H. Yang, B. Chen, X. Chen, J. Shang, W. D. Lu, Y. Wu, R. W. Li, *Adv. Mater.* 2015, *27*, 2797.
77. C.-J. Kim, S.-J. Choi, J.-H. Ahn, J.-W. Han, H. Kim, S. Yoo, Y.-K. Choi, *ACS nano* 2012, *6*, 1449.
78. S. D. Stranks, G. E. Eperon, G. Grancini, C. Menelaou, M. J. Alcocer, T. Leijtens, L. M. Herz, A. Petrozza, H. J. Snaith, *Science* 2013, *342*, 341.
79. J. Burschka, N. Pellet, S.-J. Moon, R. Humphry-Baker, P. Gao, M. K. Nazeeruddin, M. Grätzel, *Nature* **2013**, *499*, 316.
80. J. M. Ball, M. M. Lee, A. Hey, H. J. Snaith, *Energy Environ. Sci.* 2013, *6*, 1739.
81. M. Long, T. Zhang, H. Zhu, G. Li, F. Wang, W. Guo, Y. Chai, W. Chen, Q. Li, K. S. Wong, *Nano Energy* 2017, *33*, 485.
82. W. Deng, L. Huang, X. Xu, X. Zhang, X. Jin, S.-T. Lee, J. Jie, *Nano Lett* 2017, *17*, 2482.
83. L. Dou, Y. M. Yang, J. You, Z. Hong, W.-H. Chang, G. Li, Y. Yang, *Nat. Commun.* 2014, *5*, 5404.
84. H. Zhu, Y. Fu, F. Meng, X. Wu, Z. Gong, Q. Ding, M. V. Gustafsson, M. T. Trinh, S. Jin, X. Zhu, *Nat. Mater.* 2015, *14*, 636.
85. Y. H. Kim, H. Cho, J. H. Heo, T. S. Kim, N. Myoung, C. L. Lee, S. H. Im, T. W. Lee, *Adv. Mater.* 2015, *27*, 1248.
86. S. A. Veldhuis, P. P. Boix, N. Yantara, M. Li, T. C. Sum, N. Mathews, S. G. Mhaisalkar, *Adv. Mater.* 2016, *28*, 6804.
87. H. Cho, C. Wolf, J. S. Kim, H. J. Yun, J. S. Bae, H. Kim, J. M. Heo, S. Ahn, T. W. Lee, *Adv. Mater.* 2017, *29*, 31.
88. H. K. Seo, H. Kim, J. Lee, M. H. Park, S. H. Jeong, Y. H. Kim, S. J. Kwon, T. H. Han, S. Yoo, T. W. Lee, *Adv. Mater.* 2017, *29*, 12.
89. M. Long, T. Zhang, Y. Chai, C.-F. Ng, T. C. Mak, J. Xu, K. Yan, *Nat. Commun.* 2016, *7*, 13503.
90. F. Zhou, Z. Ren, Y. Zhao, X. Shen, A. Wang, Y. Y. Li, C. Surya, Y. Chai, *ACS nano* 2016, *10*, 5900.
91. C. Gu, J.-S. Lee, *ACS nano* 2016, *10*, 5413.

92. E. J. Yoo, M. Lyu, J. H. Yun, C. J. Kang, Y. J. Choi, L. Wang, *Adv. Mater.* 2015, 27, 6170.
93. Z. Xiao, J. Huang, *Adv. Electron. Mater.* 2016, 2, 7.
94. W. Xu, H. Cho, Y. H. Kim, Y. T. Kim, C. Wolf, C. G. Park, T. W. Lee, *Adv. Mater.* 2016, 28, 5916.
95. D. J. Kim, Y. J. Tak, W. G. Kim, J. K. Kim, J. H. Kim, H. J. Kim, *Adv. Mater. Interfaces* 2017, 4, 6.
96. X. Zhu, J. Lee, W. D. Lu, *Adv. Mater.* 2017, 29, 29.
97. H. Yu, F. Wang, F. Xie, W. Li, J. Chen, N. Zhao, *Adv. Funct. Mater.* 2014, 24, 7102.
98. Q. Chen, H. Zhou, Y. Fang, A. Z. Stieg, T.-B. Song, H.-H. Wang, X. Xu, Y. Liu, S. Lu, J. You, *Nat. Commun.* 2015, 6, 7269.
99. S. Colella, E. Mosconi, P. Fedeli, A. Listorti, F. Gazza, F. Orlandi, P. Ferro, T. Besagni, A. Rizzo, G. Calestani, *Chem. Mater.* 2013, 25, 4613.
100. F. X. Xie, H. Su, J. Mao, K. S. Wong, W. C. Choy, *J. Phys. Chem. C* 2016, 120, 21248.
101. R. J. Stewart, C. Grieco, A. V. Larsen, G. S. Doucette, J. B. Asbury, *J. Phys. Chem. C* 2016, 120, 12392.
102. E. M. Hutter, G. E. Eperon, S. D. Stranks, T. J. Savenije, *J. Phys. Chem. Lett* 2015, 6, 3082.
103. K. Jiao, C. Duan, X. Wu, J. Chen, Y. Wang, Y. Chen, *Phys. Chem. Chem. Phys.* 2015, 17, 8182.
104. A. Pfau, K. Schierbaum, *Surf. Sci.* 1994, 321, 71.
105. X. Wu, M. T. Trinh, D. Niesner, H. Zhu, Z. Norman, J. S. Owen, O. Yaffe, B. J. Kudisch, X.-Y. Zhu, *J. Am. Chem. Soc.* 2015, 137, 2089.
106. Y.-F. Chen, Y.-T. Tsai, D. Bassani, R. Clerc, D. Forgács, H. Bolink, M. Wussler, W. Jaegermann, G. Wantz, L. Hirsch, *J. Mater. Chem. A* 2016, 4, 17529.
107. J. M. Frost, K. T. Butler, F. Brivio, C. H. Hendon, M. Van Schilfgaarde, A. Walsh, *Nano Lett.* 2014, 14, 2584.
108. K. Yan, M. Long, T. Zhang, Z. Wei, H. Chen, S. Yang, J. Xu, *J. Am. Chem. Soc.* 2015, 137, 4460.
109. K. Yan, Z. Wei, T. Zhang, X. Zheng, M. Long, Z. Chen, W. Xie, T. Zhang, Y. Zhao, J. Xu, *Adv. Funct. Mater.* 2016, 26, 8545.
110. G. Agnus, W. Zhao, V. Derycke, A. Filoramo, Y. Lhuillier, S. Lenfant, D. Vuillaume, C. Gamrat, J. P. Bourgoïn, *Adv. Mater.* 2010, 22, 702.
111. K. Das, M. NandaGoswami, R. Mahapatra, G. Kar, A. Dhar, H. Acharya, S. Maikap, J.-H. Lee, S. Ray, *Appl. Phys. Lett.* 2004, 84, 1386.
112. C.-H. Lin, Y. Kuo, *J. Appl. Phys.* 2011, 110, 024101.
113. M. V. Srinivasan, G. D. Bernard, *Biol. Cybern.* 1976, 21, 227.
114. K. D. Cantley, A. Subramaniam, H. J. Stiegler, R. A. Chapman, E. M. Vogel, *IEEE Trans. Neural Netw. Learn. Syst.* 2012, 23, 565.
115. P. König, A. K. Engel, W. Singer, *Trends Neurosci.* 1996, 19, 130.
116. H. Agmon-Snir, C. E. Carr, J. Rinzel, *Nature* 1998, 393, 268.

CHAPTER 4 UV-switchable Transition Metal Oxide Optoelectronic Memory

4.1 Introduction

In human visual memory system, human eyes perceive an image through retina, and the image information is carried through optic nerve to the visual center of brain, where the image is further memorized, processed and interpreted. Visual prostheses, such as, artificial retinas, artificial eyes and artificial visual memory systems have been developed and demonstrated by using electronic devices for robot eyes or blind patients.^[1-4]

Conventional imaging technologies for artificial retina application, such as, the use of image sensor arrays based on photodetectors has their limitations.^[1, 2, 5] The image sensor arrays can only detect the light information in real time and the output electrical signals are further required to be transferred to the brain for memorization and processing. Further developments in artificial vision systems have been achieved along with the recent design of artificial visual memory systems by integrating sensor and memory array, which enables the mimicry of the eye-like image sensing and brain-like image memorization, opening up the path for artificial visual system design.^[4] However, the functions of these vision prostheses are restricted to image memory and the processing of sensory data cannot be achieved. Additionally, the design of sensor and memory arrays could not cater for the demands of simplicity, miniaturization and

energy efficiency.

Optically-stimulated synaptic RRAM devices are become promising candidates for a cognitive artificial eye design, which enables to sense the detected image and emulate the functions of a brain including storing and processing data as well. The employment of optoelectronic RRAM synaptic devices can potentially reduce the power consumption during the data transfer and improve the processing speed compared with conventional vision chips, in which the sensing, memory and data processing systems are separated.^[6, 7] The electrically operated synaptic RRAM devices for neuromorphic computing have been extensively investigated. However, the optically-controlled synaptic RRAM devices are rarely been developed. Additionally, as the lens on a human eye filters out UV light, human eyes cannot sense UV image like animals and UV light can also cause damage to human eyes. Therefore, an artificial eye which enables the UV sensing is desirable for the artificial eye design and could improve the imaging possibilities of human eyes.

Transition metal oxide-based photochromic materials, such as tungsten oxide (WO_3),^[8] molybdenum oxide (MoO_3),^[9] titanium dioxide (TiO_2),^[10] zinc oxide (ZnO),^[11] niobium pentoxide (Nb_2O_5)^[12] and vanadium pentoxide (V_2O_5),^[13] have been extensively studied for sunglasses, smart windows, large area displays and image storage devices. Generally, the photochromic mechanism is recognized as that the intervalent electron transfer between metal ions with different states. More specifically, for example in MoO_3 , as the oxides are irradiated with UV light, electrons and holes are generated. The photo-generated holes react with the water molecule trapped in the

MoO₃ film, resulting in the formation of proton. The resulted proton and photo-generated electron can further change the valence state of tungsten ions, accompanying with the color change. The photo-induced change of valence state of Mo ions can also result in the change in film resistances, which is potential for optoelectronic memory application.^[14]

In this work, we adopted photochromic material MoO₃ as both light absorption layer and storage medium and designed UV switchable optoelectronic memory. The MoO₃ memory exhibits both non-volatile and volatile resistive switching behaviors according to different light intensity and light wavelength applied, which allows for the implementation of light-stimulated short-term (STP) and long-term plasticity (LTP) in a simple and two-terminal optoelectronic memory device. The tunable and light-stimulated synaptic behavior not only bridges the gap between sensing and neuromorphic computing for photonic-enabled neuromorphic networks, but also provides possibilities in emulating human visual memory process including sensing in retina and processing in human brain. The memory arrays are also fabricated for mimicking the short-term and long-term image memorization process in the human visual systems, which is potential for the application of cognitive artificial eyes.

4.2 Experiments

The MoO₃ optoelectronic memories were fabricated in a configuration of Pd/MoO₃/ITO, where a 100-nm-thick Pd (bottom electrode) was firstly deposited on the SiO₂/Si substrate by e-beam evaporation with a base pressure of 8×10^{-7} Torr and

deposition rate of 0.5 Å/s. Then a MoO₃ layer with a thickness of 100 nm was deposited by thermal evaporation at an evaporation rate of 1.5 Å/s. The base pressure was 5×10⁻⁶ Torr and evaporation pressure of 9×10⁻⁵ Torr. Before the deposition of the top ITO electrode, a dot-shaped shadow mask was attached on top of the MoO₃ to define the effective area of the top electrode. The transparent ITO with a thickness of 50 nm were deposited as the top electrode by DC sputtering. The sputter base pressure was controlled as 8×10⁻⁷ Torr and deposition pressure was controlled as 3 mTorr. The deposition power was 50 W, corresponding to a deposition rate of 0.3 Å/s.

X-Ray diffraction (XRD) patterns of the perovskite film was determined by a Rigaku SmartLab X-ray diffractometer with a 2 theta range from 10 ° to 70 ° in a step of 0.01 °. X-ray photoelectron spectroscopy (XPS) were carried out in a vacuum chamber (<10⁻⁵ Torr). A monochromatic Al Ka (1486.6 eV photons) was used as the excitation source for XPS. A pass energy of 80 or 40 eV was employed for the wide and core-level narrow scan, respectively. The core-level signals were recorded at a photoelectron take-off angle of 90°. All binding energies were calibrated referring to the C1s peak at 284.6 eV. All of the electrical characterizations were conducted using probe station and Keithley 4200.

4.3 Results and Discussions

4.3.1. Device structure and switching characteristics

Figure 4.1 shows the schematic structure of MoO₃ optoelectronic memory. The bottom Pd (100 nm thickness) electrode also serves as H⁺ acceptor/reservoir. A MoO₃

layer (100 nm thickness) was deposited by thermal evaporation as the light absorption layer and data storage medium. The as-deposited MoO₃ layer is amorphous according to the XRD pattern (Figure 4.2a). The amorphous MoO₃ thin film is reported with better photochromic properties regarding to the faster response times and longer retention time, which is more appropriate for memory applications.^[15] The optical band gap of as-prepared MoO₃ layer is extracted as 3.37 eV from the absorption curve (Figure 4.2b). Thus, we utilized the UV light (365 nm) to illuminate the transparent ITO (top electrode) and stimulate the memory cell in this work.

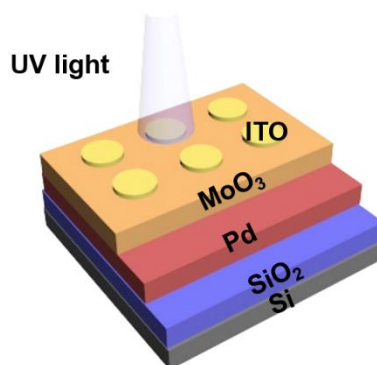


Figure 4.1. Device structure of MoO₃ optoelectronic memory.

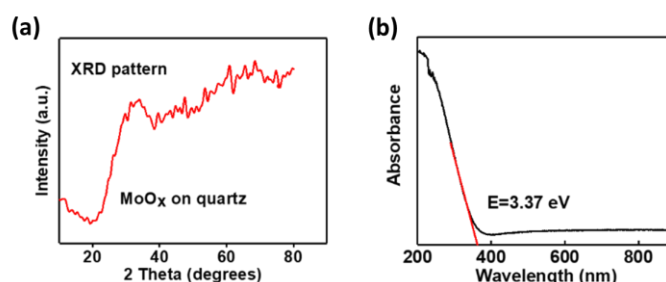


Figure 4.2. (a) XRD pattern and (b) Absorption spectrum of as-deposited MoO₃ thin film.

We first examine the DC switching characteristics of the MoO₃ optoelectronic memory, as shown in Figure 4.3a. The ITO electrode is grounded and the voltage is swept on the Pd electrode. The pristine memory cell is at HRS. As UV light with wavelength of 365 nm and power density of 150 mW/cm² is illuminated to the device,

the memory cell can be SET from HRS to LRS. A RESET process occurs at a voltage of -2.13 V during the negative voltage sweeping. No electrical switching is observed even the voltages of ± 7 V are applied with no UV light illumination (Figure 4.3b). Figure 4.3c and Figure 4.3d show the cycling and retention properties with AC switching. The SET process is operated by a UV light (365 nm) pulse with intensity of 150 mW/cm^2 and 600 ms. Electrical pulse with amplitude of -4.5 V and 100 ms is employed for the RESET process. The device delivers an ON/OFF ratio of ~ 40 with a read voltage of 0.1V. The resistances ($V_{\text{read}}=0.1 \text{ V}$) at HRS and LRS are nearly unchanged after 50 cycles (Figure 4.3c) and can be retained up to 12h (Figure 4.3d), exhibiting good reliabilities. The cumulative probability plot (Figure 4.3e) shows small device-to-device variation. We also investigated area-dependent switching characteristics of MoO_3 device. Figure 4.3f shows the relationship between HRS/LRS current and effective device areas. The device areas are controlled by the dot-shape shadow masks with the diameters of 100 μm , 250 μm and 500 μm , respectively. Both HRS and LRS currents are dependent on the device area, which is also consistent with the proposed valence state change mechanism (discussed in the next part).

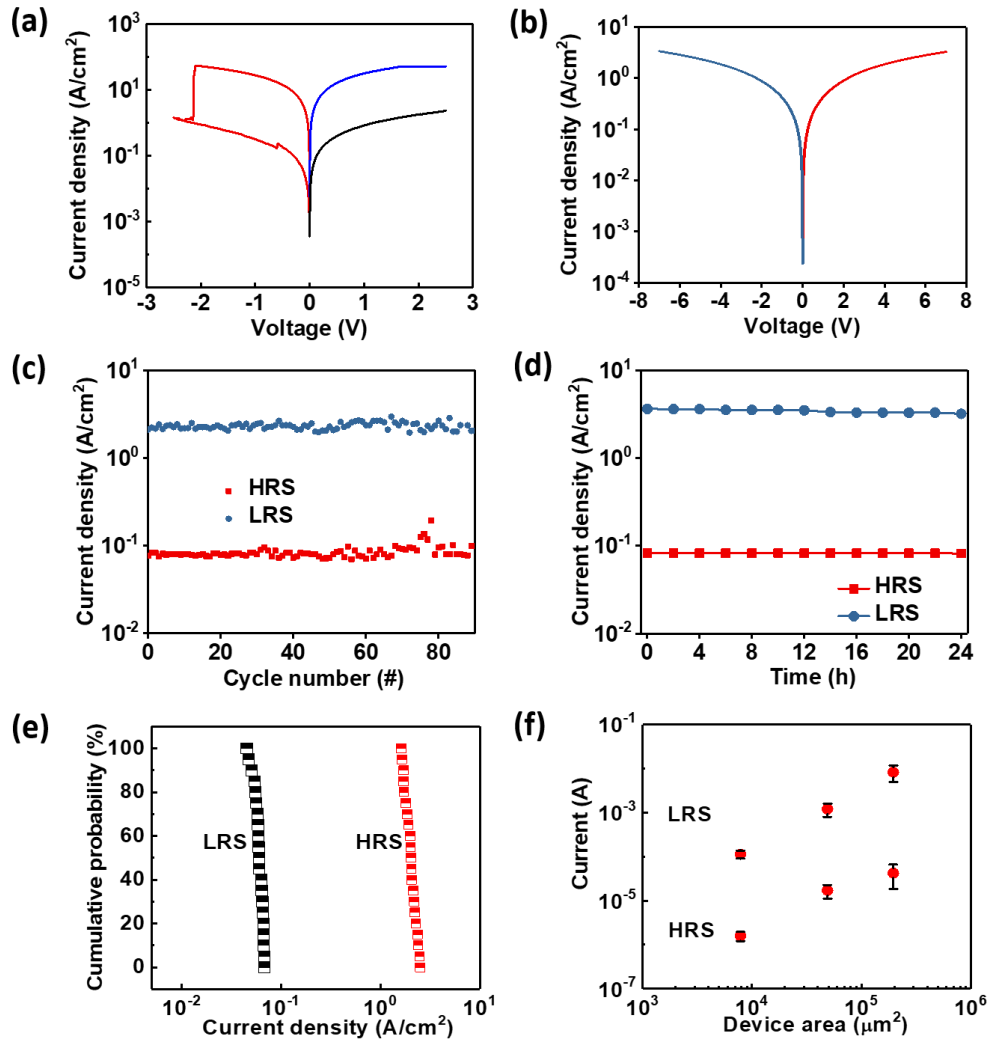
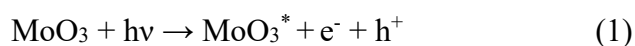


Figure 4.3 (a) The DC switching characteristics of MoO₃ optoelectronic memory. The device can be switched on by UV light with wavelength of 365 nm and power density of 150 mW/cm². (b) I-V sweeping with no UV illumination (c) Cyclic test for 50 cycles. (d) Retention test for HRS and LRS. The readout voltage used is 0.05 V. The optical pulse (150 mW/cm², 600 ms) for cyclic and retention test is employed for SET process and electrical pulse (-4.5 V 100 ms) is applied for RESET process. (e) Cumulative plot of resistances at LRS and HRS of 20 devices at different batches (f) Variations of resistances at HRS and LRS with different device areas.

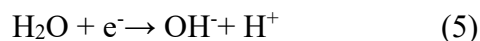
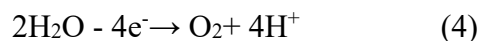
4.3.2. Switching mechanisms

The valence states of Mo⁶⁺ can be changed by external triggers, exhibiting color change as well as resistance switching. Based on the electrical characteristics of our device, we propose a switching mechanism as illustrated in Figure 4.4. The pristine

Pd/MoO₃/ITO device exhibits high resistance. The water absorbed on the surface of as-prepared MoO₃ film from ambient air plays a significant role in the photochromic process and the corresponding resistance change.^[16-18] The water molecules absorbed on the MoO₃ surface, forming the net of hydrogen bonds, which serves as tunnels for the hydrogen diffusion from water molecule to oxide surface.^[19] As the UV light is irradiated through the top ITO electrode, electrons and holes are generated in the MoO₃ film. The photo-generated electrons are excited to conduction band of MoO₃. The photo-generated holes react with the absorbed water on the surface of the film to form protons and then diffuse into MoO₃. In the meantime, the oxygen radicals occupy vacancy sites inside the sample. The photo-generated electrons and the formed protons react with MoO₃, resulting in the change in valence state of molybdenum ions from 6 to 5.^[19, 20] The process can be expressed as below:

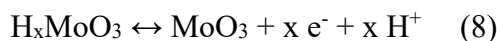
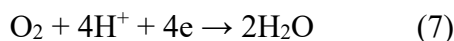
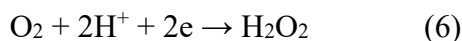


Accompanying with the change of valence state of Mo, a resistance transition of from HRS to LRS also occurs in the MoO₃ layer. The transition of electrical conductivity in MoO₃ has been reported to be associated with the hydrogen insertion in the oxide.^[20, 21] However, although applied voltage can also induce the water dissociation with no UV light, no electrical switching is observed in Figure 4.3b. This can be attributed to the different reactions occurred. The electrically induced water dissociation reactions at cathode and anode can be expressed as:



Under external electric field, H^+ and OH^- are drifted towards each other and then combined. The valence state change of Mo only occurs near the metal/ MoO_3 interface. The small amount of valence state change of Mo at the interface is insufficient for forming percolation network through MoO_3 thin film, resulting in negligible resistance change. In contrast, the products from UV-induced water dissociation induce H^+ in the MoO_3 film, which can produce uniform distribution of H^+ and cause the change of Mo valence state.

To examine the change of Mo valence state during the optical SET process, XPS narrow scans of Mo 3d core level spectra are conducted before and after UV illumination, as shown in Figure 4.5 b and c, respectively. The Mo 3d spectrum can be resolved into four peaks. At the initial state before the UV illumination, the MoO_3 film showed Mo $3d_{3/2}$ (236.0 eV) and Mo $3d_{5/2}$ (232.9 eV) peaks, which fit Mo^{6+} states well. After the UV illumination, Mo 3d peaks were fitted and dissolved into four peaks, $\text{Mo}^{6+} 3d_{3/2}$ (236.0 eV), $\text{Mo}^{6+} 3d_{5/2}$ (232.9 eV), $\text{Mo}^{5+} 3d_{3/2}$ (234.9 eV) and $\text{Mo}^{5+} 3d_{5/2}$ (231.8 eV), which suggests the formation of Mo^{5+} ions induced by UV illumination. A negative voltage is employed for the RESET process. During the electrical RESET process, protons is extracted from MoO_3 , and drifts towards the Pd bottom electrode. Pd is a well-accepted metal catalyst for oxygen reduction reaction (ORR). As protons are extracted from MoO_3 layer, the reverse reaction from H_xMoO_3 to MoO_3 is promoted, corresponding to HRS:



The produced H_2O_2 or H_2O in the ORR can be cyclically used for the UV SET process. Under the UV illumination, H_2O_2 is dissociated into H_2O and O_2 . The produced H_2O can be also used for the water dissociation process under the UV illumination.

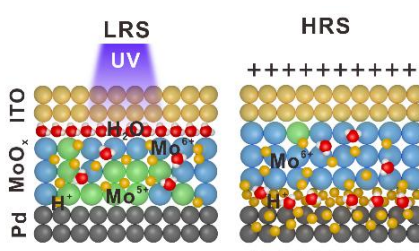


Figure 4.4. Switching mechanisms in the MoO_3 optoelectronic memory.

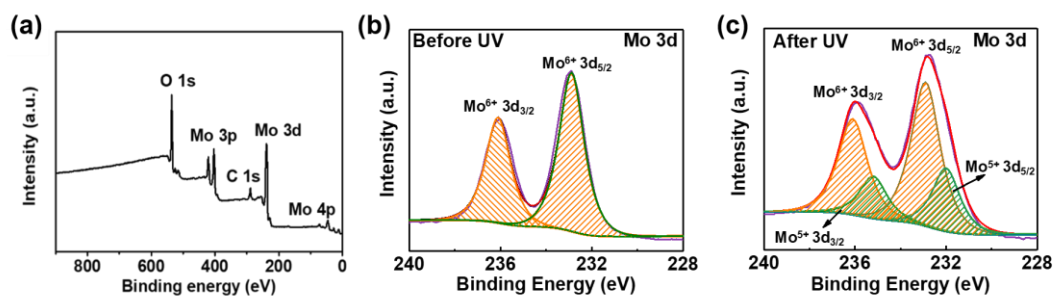


Figure 4.5. XPS spectra of MoO_3 layer on Pd electrode. (a) Wide scan. (b) Narrow scan of Mo 3d core level before UV illumination. (d) Narrow scan of Mo 3d core level after UV illumination.

To confirm the role of Pd in the RESET process, we compare the switching characteristics of ITO/ MoO_3 /Pd, ITO/ MoO_3 /Au, ITO/ MoO_3 /ITO and ITO/ MoO_3 /Mo (Figure 4.6). All of the devices can be switched by UV illumination, which can be attributed to the insertion of H^+ and change in valence state of Mo in the MoO_3 film. However, the devices with bottom electrodes of Mo and ITO cannot be RESET to HRS, in sharp contrast to the Pd/ MoO_3 /ITO cell. These results further suggest the catalytic

activity of Pd in ORR, which consumes H^+ and promote the reverse reaction from H_yMoO_x to MoO_x .

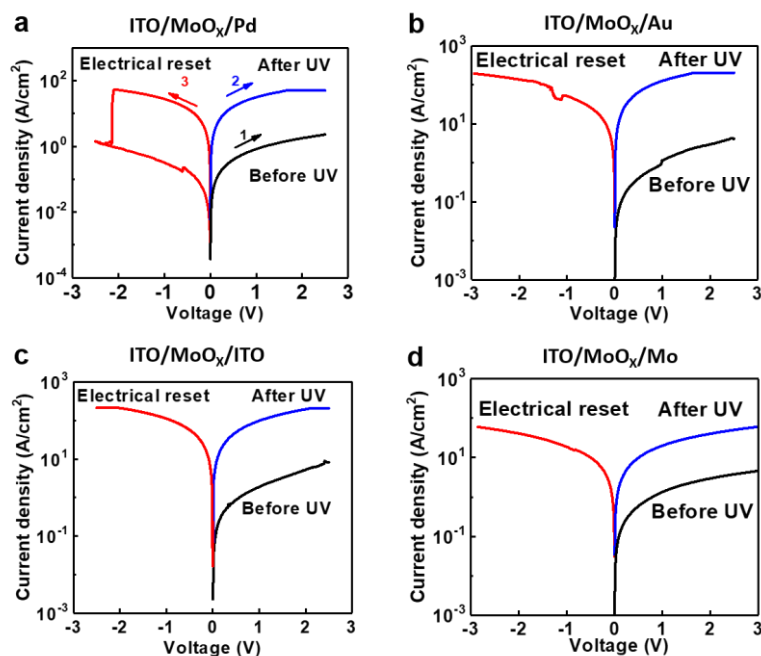


Figure 4.6 Switching characteristics of (a) Pd/MoO₃/ITO device, (b) ITO/MoO₃/Au device (c) ITO/MoO₃/ITO device and (d) ITO/MoO₃/Mo device.

As the valence state change also corresponds to the color change in the MoO₃ film, we also fabricated lateral devices on the glass substrate to observe the film color change under UV illumination and directly relate the electrical conductivity of MoO₃ to the color change/Mo valence state change. Figure 4.7 (a) shows the schematics of the lateral devices with Pd as two electrodes. We firstly deposit patterned Pd electrodes with a channel length of 30 μm and a channel width of 70 μm on the glass substrate. MoO₃ film was then deposited on top of the patterned electrodes and glass substrate. Figure 4.7(b) reveals the gradual color change of the device with UV illumination time, and Figure 4.7(c) records the corresponding device resistances at different illumination times (0s, 10 s, 20 s, 30 s). It can be clearly observed that the electrical conductivity of

the MoO₃ device increases gradually with the color changing from transparent to light blue under the UV light illumination. Other metal electrodes with different work functions, such as Au, Mo, Ti, Al, are also employed. Figure 4.7d demonstrates the variation of electrical conductivity with UV illumination time. The increasing rates of conductivity are similar for the devices with different metal electrodes, which further suggests the conductivity change originating from the MoO₃ layer instead of the interface between MoO₃ and metal electrodes.

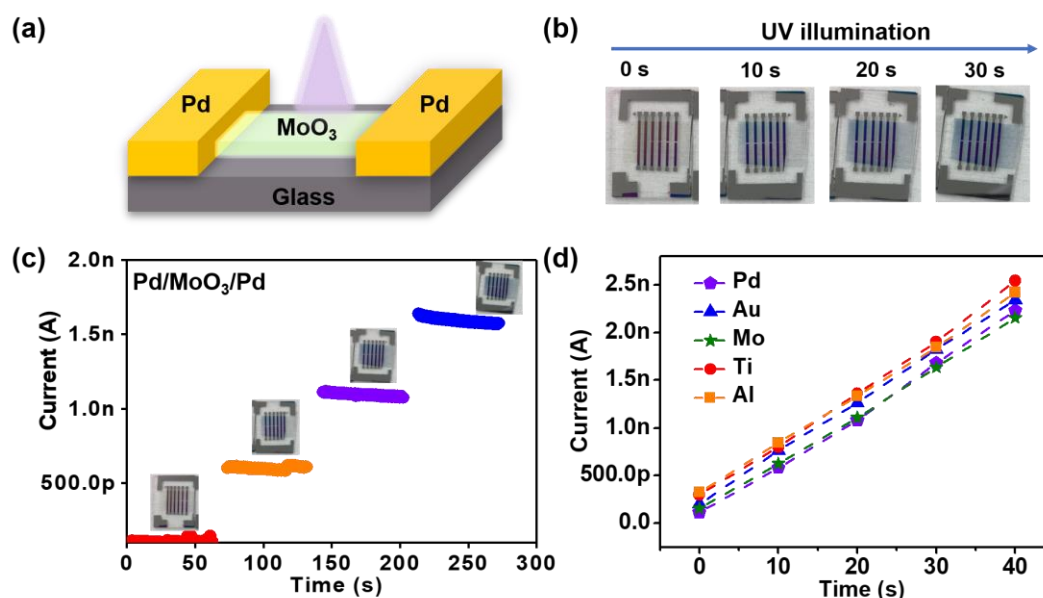


Figure 4.7. (a) Schematic of MoO₃ lateral device with Pd as electrodes. (b) Color change of the MoO₃ lateral devices during continuous UV light illumination. (c) Four resistance states corresponding to illumination times of 0 s, 10 s, 20 s and 30 s, respectively. (d) Variations of device current with illumination time for devices with different metal electrodes.

4.3.3. Synaptic functions

A network based on optoelectronic RRAMs with synaptic functions is able to emulate brain to remember, learn, and process information and is potential for the design of cognitive artificial eye, instead of the conventional artificial eye without learning and processing capabilities. For a single device, synaptic behaviors, including

short-term plasticity (STP), long-term plasticity (LTP) and spike-timing-dependent plasticity (STDP), are common functions for emulating the information memory and processing in the brain.

Therefore, based on the switching mechanism of valence state change, we use MoO_3 devices to demonstrate synaptic functions under different optical illuminations, including STP, LTP and the emulation image memory training process (Figure 4.8 and Figure 4.9), which simulate the sensing of eyes and memory and processing functions of a brain. Figure 4.8(a) shows STP stimulated by a light stimulus with intensities of 0.22, 0.45, 0.65 and 0.88 mW/cm^2 and pulse width of 200 ms. With this stimulus, the current reaches to a peak value and then gradually decreases to the original value. The current degradation can be attributed to the unstable insertion of H^+ and formation H_xMoO_3 with low light intensity.^[20] Both higher light intensity and larger pulse duration cause higher spike current and longer delay time. As the pulse width of optical stimulus is further raised to 2 s, the synaptic strengths are increased significantly (Figure 4.8 b). The increasing rate of spike current and relaxation time increases with the light intensity as a function of pulse width, owing to the improved reaction rate and increased number of protons and Mo^{5+} . In the biological systems, the transition from STP to LTP can be achieved by employing repeated pulse stimulation that persistently increases synaptic strength. To mimic the transition from STP to LTP, we conducted experiments by applying repeated successively 500 identical pulses (Figure 4.8 c). The current increases steadily with the stimulation pulse number and exhibits light-sensing behaviour. We also examine the retention characteristics after 300 pulses for 300 s

(Figure 4.8 d). The transition from STP to LTP can be clearly observed with largely increased retention time after 300 pulses stimulation. The increased pulse number can induce increased number of photogenerated charge carriers, which can further accelerate the water dissociation reaction and transition to Mo^{5+} , and increase the probability of Mo valence state change from 6^+ to 5^+ . These results discussed above suggest that our device is able to sense different light intensity and wavelength, mimic synaptic behaviors and emulate the learning and memory behaviors in human brain.

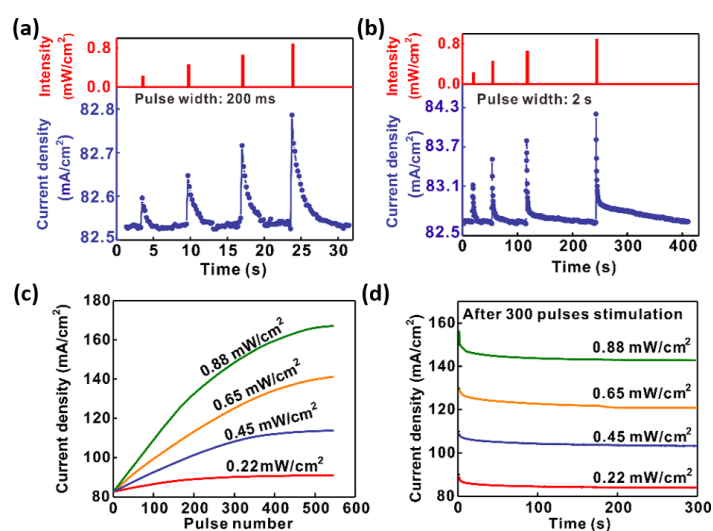


Figure 4.8. Light-tunable synaptic characteristics. (a) Light-intensity dependent STP with pulse width of 200 ms. (b) Light-intensity dependent STP with pulse width of 2 s. (c) Long-term potentiation with pulse number increased to 500 (pulse width: 200 ms, pulse interval: 200 ms). (d) Transition from STP to LTP after 300 pulse stimulation at different light intensities. The retention test is monitored with a small readout voltage of 0.1 V.

4.3.4. Emulation of visual image memory training

Based on the tunable synaptic functions in single devices, we fabricated MoO_3 memory arrays to mimic the image sensing and trainable memory processes (Figure 4.9). One memory device corresponds to one image pixel. Figure 4.9 a demonstrates image memorizations of two letters by MoO_3 memory arrays: (1) the stimuli of letter

“F” are 300 optical pulses with an intensity of 0.88 mW/cm^2 ; and (2) the stimuli of letter “L” are 300 optical pulses with an intensity of 0.45 mW/cm^2 . We recorded the images before light stimuli and after the removal of light stimuli for 3 min. Before applying the stimuli, the devices are at high resistance states. After the light stimuli, the conductance of memory devices increases, and the memory effects of letter “F” and “L” are observed. The Letter “F” exhibits stronger memory effect than the Letter “L” owing to the stronger light stimuli. The above processes suggest the capability of image memory through MoO_3 memory arrays.

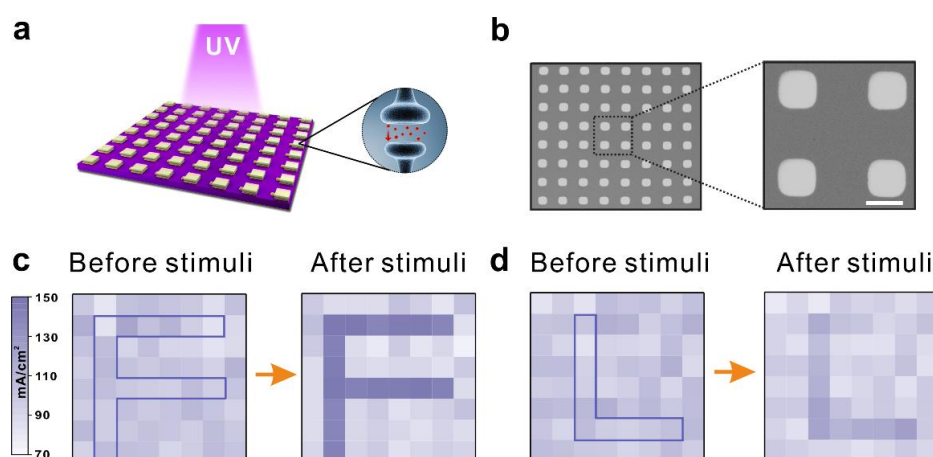


Figure 4.9. Emulation of human visual image memory process. (a) Schematic structure of 8×8 MoO_3 memory array. (b) SEM image of 8×8 MoO_3 memory. The scale bar is $200 \mu\text{m}$. Illustrations of image memory of (c) Letter “F” and (d) Letter “L”. The Letter “F” is stimulated with higher light intensity of 0.88 mW/cm^2 , and the Letter “L” is stimulated with lower light intensity of 0.45 mW/cm^2 (pulse width: 200 ms, pulse interval: 200 ms).

4.4 Summary

In this work, Pd/ MoO_3 /ITO optoelectronic memories are designed by utilizing the valence stage change in Mo ions under UV illumination. This device can be optically switched on and electrically switched off and exhibits both non-volatile and volatile

switching characteristics. Based on the synaptic functions achieved in single device, emulations of human visual memory with different external stimuli are also demonstrated by using MoO₃ memory arrays. This optoelectronic memory integrates sensing, memory and neuromorphic computing into one simple two-terminal device, which bridges the gap between sensing and neuromorphic computing and provides possibilities in visual chip and prosthesis design.

References

1. Choi, C., M.K. Choi, S. Liu, M.S. Kim, O.K. Park, C. Im, J. Kim, X. Qin, G.J. Lee, and K.W. Cho, *Nat. Commun.* 2017, 8, 1664.
2. Pei, K., X. Ren, Z. Zhou, Z. Zhang, X. Ji, and P.K.L. Chan, *Adv. Mater.* 2018, 30, 1706647.
3. Xie, X., J. Kang, Y. Gong, P.M. Ajayan, and K. Banerjee. Room temperature 2D memristive transistor with optical short-term plasticity. in *Electron Devices Meeting (IEDM), 2017 IEEE International.* 2017. IEEE.
4. Chen, S., Z. Lou, D. Chen, and G. Shen, *Adv. Mater.* 2018.
5. Lee, W., J. Lee, H. Yun, J. Kim, J. Park, C. Choi, D.C. Kim, H. Seo, H. Lee, and J.W. Yu, *Adv. Mater.* 2017, 29.
6. Qin, S., F. Wang, Y. Liu, Q. Wan, X. Wang, Y. Xu, Y. Shi, X. Wang, and R. Zhang, *2D Materials* 2017, 4, 035022.
7. Kang, J., B. Gao, P. Huang, L. Liu, X. Liu, H. Yu, S. Yu, and H.-S.P. Wong. Rram based synaptic devices for neuromorphic visual systems. in *Digital Signal Processing (DSP), 2015 IEEE International Conference on.* 2015. IEEE.
8. Xu, N., M. Sun, Y. Cao, J. Yao, and E. Wang, *Appl. Surf. Sci.* 2000, 157, 81.
9. Li, N., Y. Li, Y. Zhou, W. Li, S. Ji, H. Yao, X. Cao, and P. Jin, *Sol. Energy Mater. Sol. Cells* 2017, 160, 116.
10. Diop, D.K., L. Simonot, J. Martínez-García, M. Hébert, Y. Lefkir, G. Abadias, P. Guérin, D. Babonneau, and N. Destouches, *Appl. Spectrosc.* 2017, 71, 1271.
11. Chen, W., H. Shen, X. Zhu, Z. Xing, and S. Zhang, *Ceram. Int.* 2015, 41, 12638.
12. Sol, C. and R.J. Tilley, *Journal of Materials Chemistry* 2001, 11, 815.
13. Pan, L., Y. Wang, X. Wang, H. Qu, J. Zhao, Y. Li, and A. Gavriluk, *Phys. Chem. Chem. Phys.* 2014, 16, 20828.
14. Wang, S., W. Fan, Z. Liu, A. Yu, and X. Jiang, *Journal of Materials Chemistry C* 2018.
15. Ajito, K., L. Nagahara, D. Tryk, K. Hashimoto, and A. Fujishima, *The Journal of Physical Chemistry* 1995, 99, 16383.
16. Gavriluk, A., *Appl. Surf. Sci.* 2016, 364, 498.
17. Colton, R.J., A.M. Guzman, and J.W. Rabalais, *Accounts of Chemical Research* 1978, 11, 170.
18. Wang, S., W. Fan, Z. Liu, A. Yu, and X. Jiang, *Journal of Materials Chemistry C* 2018, 6, 191.
19. Gavriluk, A., 2009.
20. Deb, S. and J. Chopoorian, *J. Appl. Phys.* 1966, 37, 4818.
21. Bechinger, C., G. Oefinger, S. Herminghaus, and P. Leiderer, *J. Appl. Phys.* 1993, 74, 4527.

CHAPTER 5 Summary and Outlook

In this thesis, we designed three optically controlled multifunctional and smart devices: perovskite photovoltachromic supercapacitor (PVCSs), hybrid organic-inorganic perovskite optoelectronic memory and UV-switchable MoO₃ optoelectronic memory. These design of multifunctional devices are promising for the smart devices and IoT applications.

In the PVCS device, we demonstrate a solar light-powered electrochromic supercapacitor, in which the electrochromic supercapacitor can be photo-charged automatically with exhibiting simultaneous color change from transparent to deep blue. More specifically, we demonstrate co-anode and co-cathode PVCSs by vertically integrating a perovskite solar cell (PSC) with MoO₃/Au/MoO₃ transparent electrode and electrochromic supercapacitor. The PVCSs provide a seamless integration of energy harvesting/storage device, automatic and wide color tunability and enhanced photo-stability of PSCs. Compared with conventional PVCC, the counter electrodes of our PVCSs provide sufficient balance charge, eliminate the necessity of reverse bias for bleaching the device, and realize reasonable *in-situ* energy storage. The color states of PVCSs not only indicate the amount of energy stored and energy consumed in real time, but also enhance the photo-stability of photovoltaic component by preventing its long-time photo-exposure under fully charged state of PVCSs. This work designs a new type PVCS for multifunctional smart window applications commonly made of glass.

Except for the self-powered and multifunctional supercapacitor, we also demonstrated two multifunctional and optically controlled memory devices. We first demonstrate an optoelectronic resistive switching memory integrated with sensing and logic operations by adopting organic-inorganic hybrid $\text{CH}_3\text{NH}_3\text{PbI}_{3-x}\text{Cl}_x$ perovskites. The $\text{CH}_3\text{NH}_3\text{PbI}_{3-x}\text{Cl}_x$ cell exhibits low operation voltage of 0.1 V with the assistance of light illumination, long-term retention property, and multiple resistance states. The device shows different SET voltages and resistance states according to different light power densities. According to the resistive switching behavior, we proposed a trap-assisted and interface-based switching mechanism. The unique optoelectronic characteristics in the memory cell enable to perform logic operation for inputting one electrical pulse and one optical signal, and detect the coincidence of electrical and optical signal as well. This design also provides possibilities for smart sensor in IoT application.

Furthermore, we developed another Pd/MoO₃/ITO optoelectronic memory, in which both memory and sensing functions can be obtained through UV-light control. The MoO₃ memory can be optically switched on and electrically switched off, and exhibits both non-volatile and volatile switching characteristics. A switching mechanism was proposed based on the photochromic properties of MoO₃, in which the valence state of molybdenum ions can be changed under the UV light illumination. Based on the synaptic functions achieved in single device, emulations of human visual memory with different external stimuli are also demonstrated by using MoO₃ memory arrays.

The three optically controlled and multifunctional devices are promising for the future smart device design and for IoT application by providing smarter functions, lowering the power consumption and the complexity in future device design. The main challenge currently of the multifunctional devices is the trade-off between different functions as being integrated into one device. The performances of each functions are required to be further improved in the future work including broadening the sensing wavelength, improving the switching speed and developing more data processing capabilities in the optoelectronic memory. Large-scale fabrication of optoelectronic memories are also desired for realizing more data processing functions, such as pattern recognition and image classification.